



Review

A multifunctional platform by controlling of carbon nitride in the core-shell structure: From design to construction, and catalysis applications



Donghui He^{a,b}, Chen Zhang^{a,b,*}, Guangming Zeng^{a,b,*}, Yang Yang^{a,b}, Danlian Huang^{a,b}, Longlu Wang^d, Hou Wang^{a,b,c}

^a College of Environmental Science and Engineering, Hunan University, Changsha, Hunan 410082, China

^b Key Laboratory of Environmental Biology and Pollution Control (Hunan University), Ministry of Education, Changsha, Hunan 410082, China

^c School of Chemical and Biomedical Engineering, Nanyang Technological University, Singapore 637459, Singapore

^d School of Physics and Electronics, Hunan University, Changsha 410082, China

ARTICLE INFO

Keywords:

Core-shell
Carbon nitride
Catalysis
Environment
Energy

ABSTRACT

Core shell structure, which consists of an inner layer “guest” nanomaterial (nonaparticle or nanosheet) encapsulated inside another protective shell, is the most promising system for protecting the core from the surrounding environment, integrating different functional materials and providing a platform to maximize interface connectivity among the multiple components, which might enhance catalytic performance and materialization stability. Graphitic carbon nitride ($\text{g-C}_3\text{N}_4$), as an intriguing earth-abundant metal-free catalyst with a unique two-dimensional structure, excellent chemical stability, abundant “coordination nest” housing active sites, and tunable electronic structure, is a promising material for the controlled construction of core shell heterojunctions with the largest interface. At present, the applications of $\text{g-C}_3\text{N}_4$ based core shell structured nanomaterials ($\text{g-C}_3\text{N}_4$ CSNs) focus on degradation of contaminants, hydrogen production, reduction of carbon dioxide, fuel cells, as well as water disinfection. This review covers state-of-the-art achievements in $\text{g-C}_3\text{N}_4$ CSNs. The depiction comprises four sections based on $\text{g-C}_3\text{N}_4$ CSNs: the advantages of core shell structure and $\text{g-C}_3\text{N}_4$ CSNs; the design for the construction of $\text{g-C}_3\text{N}_4$ CSNs from both architectures and functions; a comprehensive overview of major advances in the synthesis of $\text{g-C}_3\text{N}_4$ CSNs; the discussion of their applications in photocatalysis, photoelectrocatalysis, and electrocatalysis. Moreover, recent strides in developing synthesis and catalytic applications of $\text{g-C}_3\text{N}_4$ CSNs, as well as an outlook section of offering some insights on the future directions and prospects of $\text{g-C}_3\text{N}_4$ CSNs, will be highlighted with the aim of overcoming the present limitations by exploiting more creative prepared methodologies and exploring other practical applications.

1. Introduction

With the expansion of urbanization and industrialization, the demand of energy is rapidly increased for satisfying human life and the emissions of various environmental pollutants threaten the survival of living things [1–6]. Ameliorating energy issues and global environmental pollution could be implemented by exploring leading-edge science and technology on catalysis to improve energy utilization and develop environmentally friendly energy sources [7–9]. Catalytic technique is an effective way to solve the problems of energy conversion and environmental remediation [10–13]. Nowadays, diverse catalysis, such as photocatalysis, electrocatalysis, and photovoltaic catalysis, is critical for many aspects of our life, such as environment, energy, biology, and chemistry [14–16]. Firstly, photocatalysis, as an

environment-good process that converts light energy into chemical energy, is often thought of as a promising approach in hydrogen evolution, degradation of pollutants, and CO_2 reduction [17–20]. Secondly, photoelectrocatalysis, as another way to use solar energy, plays an increasingly important role in degradation of pollutants and water splitting. Thirdly, electrocatalysis, can promote the performance and the deliverable weight energy and power of fuel cells.

The optimization in catalytic performance depends on component and structure of catalysis. Herein, developing a catalyst with suitable components is a crucial step. Despite metal materials as catalysis possess natural advantages, such as high efficiency, excellent selectivity, and easy recycling [21–23], the expense, scarce or bioaccumulation of metals makes them impossible to use on a large scale [24,25]. Therefore, exploring a metal-free catalytic material is essential for achieving

* Corresponding authors at: College of Environmental Science and Engineering, Hunan University, Changsha, Hunan 410082, China.

E-mail addresses: zhangchen@hnu.edu.cn (C. Zhang), zgming@hnu.edu.cn (G. Zeng).

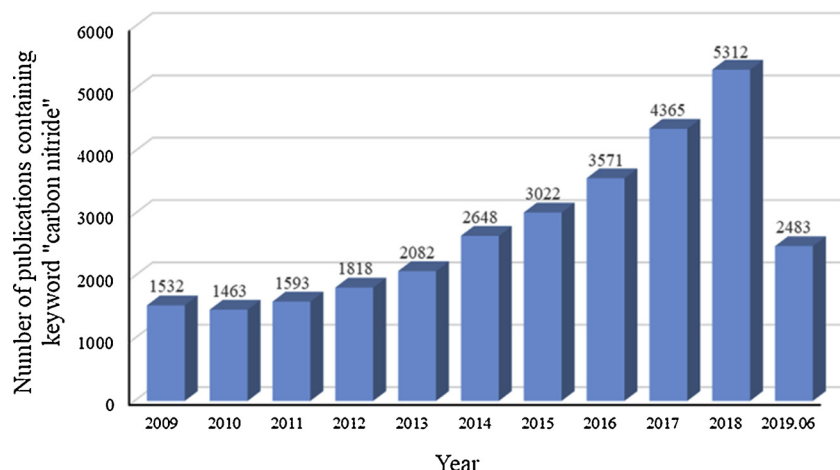


Fig. 1. Representation of the number of publications containing the keyword “carbon nitride” published from 2009 to June 2019. The data are obtained from “Web of Science”.

dramatic breakthroughs and conquering harsh challenges in catalysis. Among various catalytic materials, carbon nitride is undoubtedly a hot research material as evidenced from the increasing number of papers on indexed journals concerning the keywords “carbon nitride” over the last decade (Fig. 1). Metal-free graphitic carbon nitride ($g\text{-C}_3\text{N}_4$) has received in-depth research and the most extensive attention due to its excellent characteristics, such as versatile chemical and physical performance, high temperature resistance, excellent chemical stability, and unique structure [15,26–30]. More importantly, it has a coordination nest surrounded by a $\pi\text{-}\pi$ bond to provide active sites and can be easily peeled off into ultra-thin layers to provide more attachment sites. As early as the 1830s, Berzelius and Liebig synthesized a substance called “melon”, which was later used as the precursor of $g\text{-C}_3\text{N}_4$ [31,32]. Graphitic carbon nitride ($g\text{-C}_3\text{N}_4$) is widely used in various fields, such as purification of polluted water [33,34], evolution of hydrogen [2,20], energy storage [35–37], humidity and gas sensors [38,39], solar cells [40], and fuel cells [12,41]. Obviously, the incorporation of $g\text{-C}_3\text{N}_4$ has greatly advanced the progress in new energy development and environmental protection. However, its practical applications are limited due to inherent drawbacks, such as fast recombination of photo-generated electron-hole pairs, low surface area, difficult to separation from water, low quantum efficiency, and insufficient light absorption. To improve these shortcomings, several strategies have been developed, such as regulating morphology [23], doping other elements or molecular precursor into $g\text{-C}_3\text{N}_4$ to enhance visible-light absorption by changing the band structure [34,42], constructing the heterojunction with other semiconductors to promote photogenerated electron-hole pairs separation [43,44], and adding photosensitizers on $g\text{-C}_3\text{N}_4$ to increase quantum efficiency [45,46]. Among these strategies, constructing the heterojunction and changing structure of $g\text{-C}_3\text{N}_4$ can obtain a large area of effective contact surface and suitable transfer path for charge and substance. Building the core shell heterostructures based on $g\text{-C}_3\text{N}_4$ is determined to be the foremost measure for improving catalytic performance and preventing core from corrosion by the synergistic heterointerfaces and the protection of $g\text{-C}_3\text{N}_4$ shell, respectively.

The core shell structure has attracted a great deal of attention as it shows a comprehensive effect by integrating individual components. It represents novel physical and chemical traits, such as multi-functionality, stability, ease of conditioning and good dispersion, which is not available in a single component [47–55]. Interestingly, tight connection interfaces of the core shell structure connected by adjacent components can trigger outstanding composite performance and unexpected traits. Based on these composite characteristics, the core shell structure can expand the applications of $g\text{-C}_3\text{N}_4$ from photocatalysis to

photoelectrocatalysis and electrocatalysis, even drug delivery and optics, energy storage and conversion, separation, and adsorption. Furthermore, the $g\text{-C}_3\text{N}_4$ based core shell structure can exponentially enhance the catalytic activity in the fields of photocatalysis and photoelectrocatalysis. For example, the tetracycline degradation rate of the uniform and compact $\text{TiO}_2@g\text{-C}_3\text{N}_4$ quantum photocatalyst could reach 2.3 times that of bulk $g\text{-C}_3\text{N}_4$ [56]. Taking photoelectrocatalysis as an example, the excellent photocurrent density of carbon quantum dots (CQDs) sensitized $\text{Ti}:\text{Fe}_2\text{O}_3@g\text{-C}_3\text{N}_4$ nanosheets [57], exhibited a double effect compared to pristine $\text{Ti}:\text{Fe}_2\text{O}_3$. For electrocatalysts, amorphous carbon black@polymeric $g\text{-C}_3\text{N}_4$ also greatly promoted the development of electrodes, which was superior to the state-of-art commercial PtRu-C electrode [58]. The gratifying results are due to the complementary role of $g\text{-C}_3\text{N}_4$ and other materials. On the one hand, the $g\text{-C}_3\text{N}_4$ can act as the shell to protect the core from solution dissolution and photo corrosion. As a result, those unstable materials can show more function. On the other hand, $g\text{-C}_3\text{N}_4$ can obtain other properties (conductivity and magnetic, etc.) via embedding or combining new substances. Especially, the core shell structure can form the tight interface serving to construct a heterojunction. In parallel to the increasing reviews on the preparation of $g\text{-C}_3\text{N}_4$ based core shell nanomaterials ($g\text{-C}_3\text{N}_4$ CSNs), a review for its in-depth summary is a critical step to provide researchers for further investigation.

Previously, lots of articles have reviewed the $g\text{-C}_3\text{N}_4$ based materials with different aspects, such as polymeric [34,59], mesoporous [60,61], nanocomposites [62], doping [63], and nanosheets [64,65]. This review provides a comprehensive understanding of $g\text{-C}_3\text{N}_4$ CSNs. The core shell structure in this review refers to a stable hybrid formed by wrapping between different materials. Apart from a few examples of $g\text{-C}_3\text{N}_4$ as cores, most of them are used as the shell because of its soft polymers. In the first part, the advantages of core shell structure and $g\text{-C}_3\text{N}_4$ CSNs are elaborated. In the second part, design is described in terms of architectures and functions. In the third part, the synthesis methods have been introduced in the following categories, including hydro/solvothermal methods, ultrasonication-assisted chemisorption method, self-assembly strategies, and heat treatment. Among them, heat treatment is further divided into calcination, sol-gel assisted, CVD method, and pyrolysis process. In addition, the morphological and physicochemical features are outlined and the effects of reaction parameters are discussed. In the fourth part, the applications of core shell $g\text{-C}_3\text{N}_4$ based structure are mainly focused on photocatalytic hydrogen evolution, degradation of pollutants, photoanode, and electrocatalyst. Furthermore, we have deeply analyzed the reasons for the increased catalytic performance of core shell structured $g\text{-C}_3\text{N}_4$. Moreover, the research trends and prospects of core shell structured $g\text{-C}_3\text{N}_4$

catalysts are also summarized.

2. Advantages

2.1. Advantages of core-shell structure

Core shell structure composed of an inner 3D nanomaterial wrapped in the other material, has become the focus of complex structure of heterogeneous materials. This structure has been widely used in the frontier of significant fields, such as catalysis [66–69], optics [70,71], pharmaceutical [72], biomedical [73], electronics [74] and materials chemistry [75–77]. Herein, the main advantages of core shell structure are discussed for the photocatalytic system. For 3D photocatalytic nanomaterials, such as octahedron, cone, rod, cube, sphere, their intuitive improvement is the construction of core shell structure for surface modification. For example, the inner layer “guest” nanoparticle enhances visible light absorption by encapsulated inside photosensitizer or retards the recombination of electron hole pairs by coating with a semiconductor of suitable bandgap or increases reactive sites by loading charge receptor. In addition, surface modification can adjust porosity of core by controlling the loading amount or structure of shell. For example, by encapsulated inside porous shell, the core can obtain the optimal state between charge separation and mass transfer. The core shell structure is also conducive to dispersion of some photocatalysts in liquid, thus resulting in larger available active areas for the system. The aggregation-prone colloidal nanoparticles can combine organic shell by chemical bonding to prevent aggregation [78]. This is because of the changes in surface properties by the loading of strong hydrophilic repulsion.

In addition, for unstable substances in the external environment, such as sensitive to oxidation and corrosion, the core shell structure can improve the internal stability by isolating the direct connection between the core and the external environment. Fortunately, the nanoscale thickness of shell is powerless to prevent the light reaction of core. Moreover, the core shell structure can obtain full utilization of the surface of materials, thus leading to the maximization of internal charge transfer. Finally, when the core shell structure possesses hollow core or mesoporous core, they have ability to enhance the utilization rate of light because of multiple reflection of light. In conclusion, core shell structure shows novel physical and chemical properties, such as unique magnetic and optical properties, higher surface area, increased stability, and multifunctional chemical properties. These advantages of core shell structure will facilitate the development in catalysis and material chemistry.

2.2. Advantages of $g\text{-C}_3\text{N}_4$ CSNs

The $g\text{-C}_3\text{N}_4$ based core shell structured nanomaterials ($g\text{-C}_3\text{N}_4$ CSNs) include two types: one is consisting of the inner core of $g\text{-C}_3\text{N}_4$ and the shell (other materials); another is composed of internal core (other materials) and the shell of $g\text{-C}_3\text{N}_4$. However, most experimental papers show the latter structure of $g\text{-C}_3\text{N}_4$ CSNs, which results from the unique physicochemical properties of $g\text{-C}_3\text{N}_4$. Here, the advantages of $g\text{-C}_3\text{N}_4$ CSNs are summarized for a better understanding of the purpose of introducing $g\text{-C}_3\text{N}_4$ into core shell structure. The $g\text{-C}_3\text{N}_4$ CSNs are environmentally friendly and low-cost due to metal-free $g\text{-C}_3\text{N}_4$ that is a material composed of earth-abundant carbon and nitrogen elements. In addition, it possesses the advantages of simple preparation. In generally, $g\text{-C}_3\text{N}_4$ CSNs are synthesized by assembly of prepared $g\text{-C}_3\text{N}_4$ and other material or calcination of the mixture of $g\text{-C}_3\text{N}_4$ precursors and other prepared materials. Because $g\text{-C}_3\text{N}_4$ is the soft polymer and intriguing 2D covalent organic frameworks, $g\text{-C}_3\text{N}_4$ CSNs can combine with various forms of core (introduced in detail in the next section) and be applied to most of the functional materials, such as noble metal and magnetic materials. Considering the suitable bandgap (~ 2.7 eV) of $g\text{-C}_3\text{N}_4$, $g\text{-C}_3\text{N}_4$ CSNs show excellent visible light absorption and are

conducive for the introduction of other semiconductor materials. Moreover, the stable $g\text{-C}_3\text{N}_4$ endows core shell with the chemical and thermal stability. The $g\text{-C}_3\text{N}_4$ CSNs can immobile more metal active sites in “coordination nest” of $g\text{-C}_3\text{N}_4$. Finally, $g\text{-C}_3\text{N}_4$ CSNs possess tunable thickness by stripping $g\text{-C}_3\text{N}_4$ or controlling the amount of its precursors.

In conclusion, $g\text{-C}_3\text{N}_4$ CSNs have the advantages of green economy, simple preparation, abundant active sites, easy thickness adjustment, wide applicability and good performance. Herein, these materials are suitable for applying in the catalytic fields, such as photocatalysis, photoelectrocatalysis, and electrocatalysis.

3. Design of $g\text{-C}_3\text{N}_4$ CSNs

In this section, the design concept of recent $g\text{-C}_3\text{N}_4$ CSNs have been summarized from the two aspects of architectures and functions. The architectures are mainly divided into two categories: spherical and non-spherical; functions are divided into two categories: photocatalysis and electrocatalysis. In addition, we comprehensively introduce the internal mechanism and determining factors of the obtained structure from two aspects, because the framework of $g\text{-C}_3\text{N}_4$ CSNs is dependent on the structure of $g\text{-C}_3\text{N}_4$ or other materials.

3.1. Architectures

The $g\text{-C}_3\text{N}_4$ CSNs with differing compositions, dimensionalities and architectures have been constructed, and will be described below (Fig. 2).

3.1.1. Spherical $g\text{-C}_3\text{N}_4$ CSNs

Spherical $g\text{-C}_3\text{N}_4$ CSNs are constructed via layer-by-layer coverage of $g\text{-C}_3\text{N}_4$ shells or thermal polymerization of $g\text{-C}_3\text{N}_4$ in a hollow shell. Typical examples include $g\text{-C}_3\text{N}_4$ nanosheets coating on other nanoparticles with tens to hundreds of nanometers in diameter, and multi-layer of shells growing on a spherical hard template to prepare a hollow structure. For example, SiO_2 and C nanospheres were used as hard templates for preparation of $\text{TiO}_2@g\text{-C}_3\text{N}_4$ hollow spheres and $\text{C-TiO}_2@g\text{-C}_3\text{N}_4$ hollow spheres, respectively [79,80]. Moreover, microporous materials with large surface areas are interesting for applications in catalysis [81]. Another intriguing example is that carbon nitride encapsulating mesoporous nanospheres, which include the outer package of mesoporous core with hundreds of nanometers [82], and the full package of reunion mesoporous microspheres [83]. This may depend on using $g\text{-C}_3\text{N}_4$ nanosheets or precursors to cover. In addition to being shell, $g\text{-C}_3\text{N}_4$ can also serve as core, such as melamine calcining in Fe^{3+} /polyphenol to form $g\text{-C}_3\text{N}_4$ core [84].

3.1.2. Non-Spherical $g\text{-C}_3\text{N}_4$ CSNs

Non-spherical $g\text{-C}_3\text{N}_4$ CSNs are constructed by the covering of $g\text{-C}_3\text{N}_4$ on other types of nanocores, such as nanorods [85–87], nanowires [88], and nanoctahedra [89], nanocone [90]. The core of the nanorods can be subdivided into a cylindrical shape and a prismatic shape, and the ends of the nanorods may be enclosed or exposed. Moreover, another construction idea is to fill the prepared $g\text{-C}_3\text{N}_4$ shell with core materials. For example, core-shell $\text{LaPO}_4/g\text{-C}_3\text{N}_4$ nanowires [86] was prepared by hydrothermal methods of La^{3+} and PO_4^{3-} ions in the tubular $g\text{-C}_3\text{N}_4$.

Two-dimensional structures make up another representative type of non-spherical $g\text{-C}_3\text{N}_4$ CSNs. For example, the “Pt-free” hierarchical electrocatalyst was prepared by rough, microporous and cratered $g\text{-C}_3\text{N}_4$ covering on graphene sheets [91].

3.1.3. Internal mechanism for the formation of the structure

Increasing numbers of papers are developing $g\text{-C}_3\text{N}_4$ CSNs with unique structures for various applications. By the knowledge that we receive, the different structure of $g\text{-C}_3\text{N}_4$ CSNs can be manipulated by

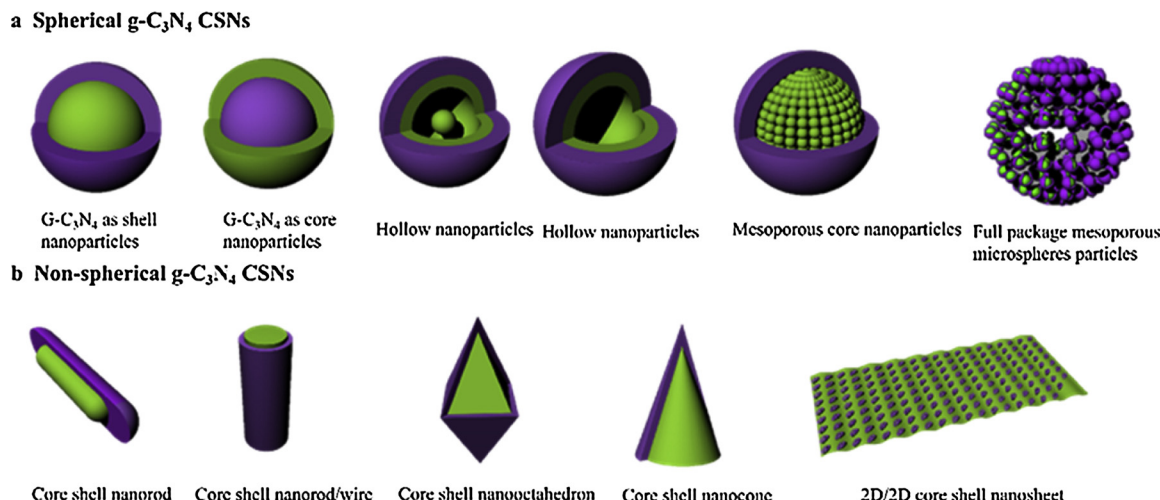


Fig. 2. Schematic illustration of various architectures of $\text{g-C}_3\text{N}_4$ CSNs. a. Spherical $\text{g-C}_3\text{N}_4$ CSNs include $\text{g-C}_3\text{N}_4$ as shell nanoparticles, $\text{g-C}_3\text{N}_4$ as core nanoparticles, hollow nanoparticles, mesoporous core nanoparticles, and full package mesoporous microspheres particles. b. Non-Spherical $\text{g-C}_3\text{N}_4$ CSNs include core shell nanorod, core shell nanorod/wire, core shell nanoctahedra, core shell nanocone, and 2D/2D core shell nanosheet.

attaching to other materials by $\text{g-C}_3\text{N}_4$, copolymerizing carbon nitride precursors inside other materials, and incorporating other materials into the framework of $\text{g-C}_3\text{N}_4$. Owing to $\text{g-C}_3\text{N}_4$ with deformable ultrathin 2D structure, it can facilely load on cores of any structure, such as spherical and rod-shaped. More importantly, this loading does scarcely change the core of structure, thus retaining the excellent properties of the original materials. In the second case, spherical $\text{g-C}_3\text{N}_4$ CSNs can be obtained by calcining the $\text{g-C}_3\text{N}_4$ precursor encapsulated in a polymeric organic material. Owing to the uniform fluid pressure, the polymeric organic material forms stable spherical structure. For example, the as-prepared polyphenol coating on melamine was calcined to spherical $\text{g-C}_3\text{N}_4@\text{C}$ nanocomposites [84]. In the third case, the structure of $\text{g-C}_3\text{N}_4$ CSNs depends on $\text{g-C}_3\text{N}_4$ instead of other materials. By the special treatment of $\text{g-C}_3\text{N}_4$ precursors, $\text{g-C}_3\text{N}_4$ can obtain the hollow 3D structure, which is used for framework of $\text{g-C}_3\text{N}_4$ CSNs. As the tubular $\text{g-C}_3\text{N}_4$ synthesized by chemical treatment was filled with LaPO_4 [86].

3.2. Functions

The $\text{g-C}_3\text{N}_4$ CSNs could be applied for photocatalytic and electrocatalytic fields. Therefore, the function designs of $\text{g-C}_3\text{N}_4$ CSNs for photocatalytic applications, which divide into four parts (enhancement/broadening of light absorption, maximization of interface area, enhancement of charge transfer and separation, improvement of stability and good reuse, and mass transfer enhancement), are highlighted. For electrocatalytic applications, $\text{g-C}_3\text{N}_4$ CSNs have additional contents due to its different requirements, which will be described separately.

3.2.1. Enhancement/broadening of light absorption

It is widely recognized that $\text{g-C}_3\text{N}_4$ with the band gap of 2.7 eV can only use light with a wavelength of less than 460 nm. However, the solar energy mainly concentrated in visible light (420 nm~760 nm) and infrared (IR) light (> 760 nm), which account for 44% and 52% of total energy, respectively. Accordingly, obtaining high light absorption is critical to improve photocatalytic performance. By building the core shell structure, the hybrids can possess outstanding light harvesting. In this part, we will discuss reasons of enhancing light absorption from two perspectives: one is extra light harvesting; another is the expansion of the light absorption range.

During the construction of core shell structure, some strategies can be carried out for extra light harvesting, such as constructing hollow core shell structure, dye coating. Multiple reflections of light are caused

by hollow structure that enhance the utilization efficiency of solar energy. For the second point, the dye, such as triazine-based oligomer (TBO), can effectively obtain visible light by self-sensitization, which will produce new electrons onto the $\text{g-C}_3\text{N}_4$.

It is a huge challenge that expanding light absorption range from ultraviolet light to IR light. On the basis of the factor that narrow band gap is the root cause of increase light absorption range, some approaches for obtaining the narrow band gap can be summed up, such as preparing materials with element doping or defects, matching narrow bandgap semiconductors. These proposals can be achieved by building a core shell structure. Element doping can fill the interstitial positions or substitute atomic sites in the original substance, leading to changes in the band structure. The C, N co-doped core shell structure showed high range of visible light response due to the narrow band gap. In addition, oxides can obtain oxygen vacancies to shorten the band gap, such as obtaining oxygen defects-mediated TiO_2 and ZnO by an electron beam treatment and a solution conversion method, respectively. Among them, the incorporation of ZnO with oxygen defects into the $\text{g-C}_3\text{N}_4$ CSNs achieved the expansion of light absorption in the visible light range. However, the binary core-shell structure is still difficult to achieve full-spectrum light absorption. Fortunately, the full-spectrum light absorption succeeded by adding other moiety in the binary core-shell heterojunction. For example, the introduction of C moiety in $\text{g-C}_3\text{N}_4@\text{Fe}_2\text{O}_3$ core shell nanomaterials can increase the absorption edge to 800 nm, which may be due to the reduction of work function leading to a band bending of CB toward less negative. In the core shell structure, the introduction of new components can be at the interface. For instance, Feng et al. [92] not only coupled $\text{g-C}_3\text{N}_4$ with Ag_2CrO_4 to form Z-scheme heterojunction, but also added nitrogen-doped GQDs (N-GQDs) between the cores and the shells. N-GQDs can use infrared light and converts it into visible light because of the up-conversion effect, resulting in full-spectrum absorption. In general, the combination of multiple components is prerequisite for full-spectrum absorption. The core shell structure is a good choice for tightly bonding multiple substances.

3.2.2. Maximization of interface area

Since the large number of charge separation is carried out at interface between solids, when charge is effectively transferred between interfaces, the total interface area of composites is one of the most important factors affecting photocatalytic performance. However, the nanomaterials are used for synthesizing the composite structure by the common designs, such as 0D/2D, 1D/2D, 2D/2D connection, which

display very low contact area because the surface area of the nanomaterials is not fully utilized. Through the published literatures, other materials (e.g. 0D, 1D, 2D) adhere only to the surface of 2D nanomaterials, which undoubtedly results in the majority of the surface area not forming contact surfaces [93–95]. However, Feng et al [92] maximized the surface area of spherical Ag_2CrO_4 by wrapping it in small pieces of carbon nitride. Compared to the growth of Ag_2CrO_4 on the surface of 2D $\text{g-C}_3\text{N}_4$, the full 3D contact can maximize the contact area. Given the small area of point-to-point (0D/2D, 1D/2D) and face-to-face (2D/2D) by random loading of other materials [96–98], Shen et al. [99] coupled $\text{g-C}_3\text{N}_4$ shell on the surface of SiO_2 core to obtain the large contact area. Among these combined forms, the heterointerface between TiO_2 and $\text{g-C}_3\text{N}_4$, which are respectively regarded as the most promising metal hydrophilic photocatalyst and metal free organic polymer semiconductor photocatalyst, is difficult to achieve the optimal charge kinetics and electron-hole pairs separation efficiency. Fortunately, because their matched band gap, plenty of studies attempted to construct heterostructures between them, $\text{TiO}_2@g\text{-C}_3\text{N}_4$ composites with compact and large interface area were successfully synthesized by facile methods, such as chemically modified solution method, in-situ synthesis. Herein, coupling the $\text{g-C}_3\text{N}_4$ ultrathin nanosheets as shells with cores by the 3D contact can obtain the largest interface area, which serves as a good method to change the structure of composites. The maximization of interface area can increase the active surface area, facilitate separation and transfer of charge carriers. It facilitates the plasmonic energy transfer processes that maximizing the metal–support interaction between the semiconductor shell and the metal core under three-dimensional contact conditions.

3.2.3. Enhancement of charge transfer and separation

It is well known that the most significant disadvantage of bulk $\text{g-C}_3\text{N}_4$ is facile recombination of photogenerated electrons and holes. Fortunately, the core shell structure can form a large area of heterojunction derived from the match of energy and lattice by matching $\text{g-C}_3\text{N}_4$ with other substances. The $\text{g-C}_3\text{N}_4$ as an n-type semiconductor can form p-n junction by coupling with p-type semiconductor. This will form the inner electric field resulting in photogenerated holes moving n-type to p-type and electrons moving p-type to n-type. Numerous studies demonstrated that the core shell structure can construct type II heterojunction by p-n junction, like $\text{CuFe}_2\text{O}_4@g\text{-C}_3\text{N}_4$ [100]. Compared with type II heterojunction, the Z-scheme heterojunction not only promotes charge separation but also obtains high redox potential. As a result, some measures can obtain $\text{g-C}_3\text{N}_4$ CSNs with Z-scheme heterojunction as follows: (I) The semiconductors with hole-retaining reduce the conduction band by introducing oxygen vacancies [85]; (II) The substances with superior electron mobility connect both sides of the interface, such as C and CNT [84,101]. In addition, sensitizers, reservoir of charge as a party to the core shell structure or adding cocatalysts, which helps to enhance the separation efficiency of charge carriers.

It is worth pointing out that two main factors, namely, the tightness and thickness of shells, can affect photocatalytic performance and separation of photogenerated electrons and holes. This is because the former can enhance surface heterojunction and reduce charge transfer resistance. The latter can reduce pathway of charge transfer leading to fewer recombination and improve quantum confinement effect.

3.2.4. Improvement of stability and good reuse

The further applications of excellent semiconductor materials and noble metals are restricted due to photocorrosion and dissolution. Take for an example, CdS possesses a perfect electronic structure and energy band gap (~2.4 eV) for water splitting and capturing visible light. Nevertheless, its catalytic performance is limited due to the problem of photocorrosion that sulfur ions are oxidized to S by photogenerated holes. By constructing the core shell structure coupling $\text{g-C}_3\text{N}_4$ nanosheets with CdS , the corrosive holes from CdS will transfer to $\text{g-C}_3\text{N}_4$ resulting in the inhibition of phototocorrosion [102]. Other than that,

Ag -based semiconductors, like AgI and Ag_3PO_4 , can be reduced into Ag under illumination and dissolve in water. This is not conducive to apply them in treating wastewater and splitting water. In addition to avoiding photocorrosion, the coating of stable $\text{g-C}_3\text{N}_4$ shells can handle two difficulties, namely, avoiding direct contact between the Ag -based semiconductors and water, and forming large interface area to enhance the structural stability. It should point that $\text{g-C}_3\text{N}_4$ CSNs possess high mechanical stability due to the high stability of $\text{g-C}_3\text{N}_4$ and effects of force between cores and shells, such as Van der Waals forces, electrostatic force. Under these circumstances, some readily dispersible substances can well bind and concentrate, such as Ag , C as cores. Plenty of cyclic experiments [103] demonstrated its surface chemical property and crystal structure have not changed after using it multiple times.

As well, the valid separation of catalysts can implement by constructing core shell structure. On the one hand, under the package of shells, the weight and dimension of composites are increased. For instance, the $\text{AgFeO}_2@g\text{-C}_3\text{N}_4$ catalyst can spontaneously precipitate to achieve the purpose of collection. On the other hand, the introduction of magnetic cores, such as CuFe_2O_4 [104] and Fe_2O_3 [84], can be conducive to separate by magnetic force.

3.2.5. Mass transfer enhancement

Mass transfer is a material transfer process that occurs in a system due to uneven material concentrations [105]. On the basis of different location of the reactants, mass transfer can be divided into external mass transfer and internal mass transfer [106]. External mass transfer is related to the number of catalyst surface sites and the flow rate of medium [107,108]. For $\text{g-C}_3\text{N}_4$ CSNs, one method to enhance external mass transfer is through the coating of the core with porous $\text{g-C}_3\text{N}_4$. This is because porous $\text{g-C}_3\text{N}_4$ feathers a large surface area and an open crystalline pore wall. For example, the coating of TiO_2 and ZnO with mesoporous $\text{g-C}_3\text{N}_4$ presents the improved effect of mass transfer [83,109].

For the $\text{g-C}_3\text{N}_4$ CSNs, the internal mass transfer is related to an intrinsic property of components, the thickness of the catalyst film, and coating methods used [110,111]. The internal mass-transfer resistance of a core shell photocatalytic system is affected by the diffusion of reactant molecule within voided film shell. By the adjustment of shell thickness, a synergistic effect of the core and the shell, or the construction of nanointerspace channels, internal mass transfer can consequently be increased. For example, coating of CuFe_2O_4 nanoparticles with $\text{g-C}_3\text{N}_4$ has improved the mass transfer reaction of active substances due to the synergistic effect of the core and the shell [104]. And coating of ZnO nanoparticles with $\text{g-C}_3\text{N}_4$ has improved the mass transfer reaction of active substances due to the nanointerspace channels [112].

3.2.6. Function designs of $\text{g-C}_3\text{N}_4$ CSNs for electrocatalysis

The new generation of CN-based electrocatalysts (ECs), which are characterized by core shell structure, can be designed from the inside out to improve electrocatalytic performance. Using carbonaceous materials (e.g. Fe_3C , graphene, and Vulcan XC-72 carbon black) as core can ensure that minimizing ohmic drops achieves easy electron transfer between active points and external circuits because of their outstanding electrical conductivity [58,113,114]. More interesting, the core can be served as supplemental source of active sites. For example, Jin et al. [115] used the cobalt oxide as the core of ECs to continuously provide cobalt ions as active sites. Hence, the ECs will possess the high stability, even if the surface active sites could be unstable after multiple operations.

Under the protection of the $\text{g-C}_3\text{N}_4$ shell, the unstable carbonaceous materials (e.g. Vulcan XC-72R) can slow down corrosion after long-time operation in varying potential and acidic electrolyte because of mechanical and chemical stability of $\text{g-C}_3\text{N}_4$ in oxidative and acidic environments. In addition, because $\text{g-C}_3\text{N}_4$ has lots of Lewis base and acid sites, it can increase anchoring and precipitation sites for metal

Table 1The comparison of construction methods and the potential applications of $g\text{-C}_3\text{N}_4$ CSNs.

| Construction methods | Advantages | Disadvantages | Applications |
|---|--|---|---|
| Hydro/solvothermal methods | Solution processable; Large scale; Good crystallization | Difficult to control interfacial growth process | Photocatalysis; Photoelectrocatalysis; Electrocatalysis |
| Ultrasonication-assisted self-assembly strategies | Solution processable; Tunable thickness; Controllable interface formation; | Only $g\text{-C}_3\text{N}_4$ shell | Photocatalysis; Photoelectrocatalysis |
| Calcination | Large scale; Suitable for heat-resistant materials | Energy-intensive | Photocatalysis; Photoelectrocatalysis; Electrocatalysis |
| Sol-gel assisted calcination | Solution processable; Tunable thickness; Large scale; stable interface | Energy-intensive | Photocatalysis; Photoelectrocatalysis; Electrocatalysis |
| CVD method | Tunable thickness; Immobilization | Require special instruments | Photocatalysis; Photoelectrocatalysis |
| Pyrolysis process | Large scale | Energy-intensive; Complex processes | Electrocatalysis |

active nanoparticles (NPs). The core shell structure based on the $g\text{-C}_3\text{N}_4$ shell not only improve the interaction between support materials and metal active NPs, but can also increase the triple-phase boundary for acting on electrochemical reactions by avoiding NPs “buried” in the support materials. For example, to overcome the shortcoming of Pt nanoparticles (NPs) buried inside the pores, Li et al. [58] skillfully used carbon nitride to “catch” the Pt NPs. On account of C- and N- based ligands in $g\text{-C}_3\text{N}_4$, the co-catalyst and active metal, which can enhance ECs performance and reduce overpotential respectively, can be fixed in “coordination nests” [91].

4. Construction methods

The key to the preparation of $g\text{-C}_3\text{N}_4$ CSNs is the thickness of the $g\text{-C}_3\text{N}_4$ shell and the tightness of the core-shell connection. The former is closely related to the mass ratio of $g\text{-C}_3\text{N}_4$. The latter mainly depends on the connection force in the synthesis method. The developed synthesis methods are divided into the following categories: (I) hydro/solvothermal methods, (II) ultrasonication-assisted self-assembly strategies, (III) heat treatment (including calcination, sol-gel assisted calcination, CVD method, and pyrolysis process), summarized in Table 1. In addition, to visually show correspondence between above methods and structure, Table 2 summarizes different $g\text{-C}_3\text{N}_4$ core shell structure suitable for each method.

4.1. Hydro/solvothermal methods

Hydro/solvothermal methods are facile and popular solution approaches for synthesis of composite materials and multifunctional materials, such as sulfides, yolk-shell structure, and magnetic iron(III)-based framework composites.

4.1.1. Hydrothermal method

Hydrothermal method is the most common method for preparing nanomaterials by treating the solution of water as a solvent in a sealed pressure vessel for several hours. The powder is dissolved first and then crystallized. The resulting powder by this method has complete grain development, small particle size, and uniform distribution. Li et al. [86] fabricated a series of core shell structured $\text{LaPO}_4@g\text{-C}_3\text{N}_4$ nanocomposites via a simple hydrothermal growth. The $\text{LaPO}_4/g\text{-C}_3\text{N}_4$ (Fig. 3(a)) exhibited the tubular-like $g\text{-C}_3\text{N}_4$ (tCN) is well filled with LaPO_4 to form a sandwiched tubular composite and retained the morphology of LaPO_4 . Besides, the composite sample forms a tight hetero-interface with two (002) lattice planes of tCN and one (100) lattice planes of LaPO_4 on each side (Fig. 3(b)). More importantly, surface energy is reduced during the formation of the tubular $g\text{-C}_3\text{N}_4$ shell. As shown in Fig. 3(c), the melamine is deprotonated by nitric acid to obtain a precipitate. Then, for elevating crystallinity and reduce tubular $g\text{-C}_3\text{N}_4$ surface and structural defects, the washed precipitate is calcined twice (first 450 °C, second 550 °C). Finally, the resultant tCN was dispersed in solution containing La^{3+} and PO_4^{3-} . During hydrothermal

growth, La^{3+} and PO_4^{3-} enter into the $g\text{-C}_3\text{N}_4$ shells by electrostatic interaction to form the LaPO_4 core. Subsequently, Gu and co-workers [116] used a one-pot hydrothermal method for synthesis of $\text{SSCN}@\text{MoS}_2$ by using $(\text{NH}_4)_2\text{MoS}_4$ and 1,3,5-triazine as the precursor. (002) facet of MoS_2 rises with increasing the mass ratio of MoS_2 . The characteristics indicated the successful preparation of the thin layer coating onto the SSCN microspheres. The research found triazine-based oligomer (TBO) dyes as photosensitizer could promote visible-light absorption and MoS_2 as coating provided active sites. Despite main core shell structured nanomaterials focusing on binary composite, there are also super binary composite such as ternary and quaternary. In general, the strategy for synthesis of super binary composite involves the choose of connector. Metal-organic frameworks (MOFs) exhibits the features of both wide variable composition and high internal surface area and possess structural features to easily combine with other components, thus resulting in wide photocatalytic applications. For example, Khasavani [123] synthesized the $\text{Ag}_3\text{PO}_4/\text{BiPO}_4@\text{MIL-88B}(\text{Fe})@g\text{-C}_3\text{N}_4$ (AB@MIL-88B(Fe)@g-CN) core shell structured nanocomposite by hydrothermal method, which introduce MOFs into photocatalysis. In this process, $\text{Ag}_3\text{PO}_4/\text{BiPO}_4$ (denoted as AB) nanoparticles precipitated on the outmost layer of as-prepared core shell MIL-88B(Fe)@g-C₃N₄, owing to their unique ability to absorb light. Besides, MIL-88B(Fe)@g-C₃N₄ plays a major role in providing active sites and accelerating charge transfer due to its large surface area and good conductivity, respectively. Moreover, the quaternary composite exhibited 85% removal of AB92 because of the heterojunction formed by individual components. Meanwhile, they have prepared ternary novel $\text{BiOI}@\text{MIL-88A}(\text{Fe})@g\text{-C}_3\text{N}_4$ nanocomposite by the same method [124]. More interesting, the composite exhibited higher photocatalytic activity for AB92 (88% removal of AB92) than the previous quaternary composite. It can be inferred that BiOI as a sensitizer possesses stronger light absorption than AB.

4.1.2. Solvothermal method

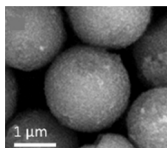
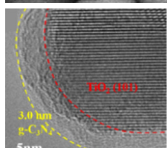
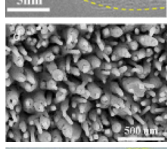
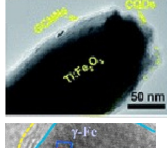
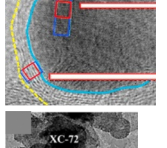
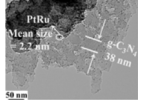
The solvent of solvothermal method is organic solvent, which is different from the hydrothermal method. It can be noted that products of the solvothermal process often possess uniform facets and high-quality crystallinity. For example, Yan et al. [125] successfully reformed $\text{CdS}@g\text{-C}_3\text{N}_4$ core/shell nanorods by loading with nickel hydroxide. It is noteworthy that $\text{Ni}(\text{OH})_2$ is a cocatalyst on the surface of $\text{CdS}@g\text{-C}_3\text{N}_4$. The samples were obtained by heating the slurry, which is prepared by stirring of $\text{CdS}/g\text{-C}_3\text{N}_4$ and $\text{Ni}(\text{NO}_3)_2\cdot 6\text{H}_2\text{O}$ in the mixed solution of oleyamine and ethanol, in 50 mL Teflon-lined autoclave. The ultrathin $g\text{-C}_3\text{N}_4$ shells can contribute to preventing CdS corrosion and accept holes from CdS . The uniform facets of a $\text{Ni}(\text{OH})_2\text{-CdS}/g\text{-C}_3\text{N}_4$ sample was confirmed by HRTEM image, which showed exposed (002) lattice planes of $g\text{-C}_3\text{N}_4$ shell and CdS core, whose lattice spacing are 0.325 nm and 0.336 nm, respectively. In addition, the mass ratio of $\text{Ni}(\text{OH})_2$ in the sample has the best value, and when it is more or less, it is not conducive to light absorption. Another case also used ethylene glycol as the solvent of solvothermal method. You et al. [126]

Table 2The suitable preparation method for g-C₃N₄-based core-shell structures.

| Composites | SEM/TEM images | Methods | C sources/N sources | Conditions | Ref. |
|--|----------------|---|---|--|-------|
| Core-shell g-C ₃ N ₄ /MCNTs/BiOI nanocomposites | | Solvothermal | Cyanamide | 150 °C for 12 h | [101] |
| SSCN ^a @MoS ₂ microspheres | | Hydrothermal | Cyanuric chloride and cyanuric acid with a molar ratio of 1.8 | 160 °C for 10 h | [116] |
| Core-shell LaPO ₄ /g-C ₃ N ₄ nanowires | | Hydrothermal | Melamine | 160 °C for 20 h | [86] |
| core-shell TiO ₂ @g-C ₃ N ₄ hollow microspheres | | Ultrasonication-assisted self-assembly strategies | Melamine | Evaporated by 80 °C water bath | [117] |
| g-C ₃ N ₄ /OD-ZnO ^b | | Ultrasonication-assisted self-assembly strategies | Urea | Evaporation of the water by stirring at room temperature for 48 h | [85] |
| Cu ₂ O@g-C ₃ N ₄ octahedra | | Ultrasonication-assisted self-assembly strategies | Melamine | Evaporation of the water by stirring at room temperature for 48 h | [89] |
| Eu doped g-C ₃ N ₄ @BiVO ₄ | | Calcination | Melamine | 300 °C for 1 h | [118] |
| Mesoporous TiO ₂ @g-C ₃ N ₄ hollow core@shell | | Calcination | Cyanamide | 550 °C under flowing N ₂ for 1 h with a ramp rate of 2.5 °C min ⁻¹ | [80] |
| g-C ₃ N ₄ @α-Fe ₂ O ₃ /C | | Calcination | Melamine | 550 °C for 4 h with the heating rate of 5 °C min ⁻¹ | [84] |
| NaYF ₄ : Yb, Er/g-C ₃ N ₄ | | Calcination | Melamine and cyanuric acid | 550 °C in N ₂ atmosphere for 3 h | [119] |
| TiO ₂ @g-C ₃ N ₄ core-shell nanorod arrays | | Calcination | Cyanamide | 500 °C for 2 h | [120] |

(continued on next page)

Table 2 (continued)

| Composites | SEM/TEM images | Methods | C sources/N sources | Conditions | Ref. |
|--|--|------------------------------|---|---|-------|
| Mesoporous TiO ₂ /g-C ₃ N ₄ microspheres |  | Calcination | Myanamide | 550 °C in nitrogen for 4 h | [83] |
| g-C ₃ N ₄ @TiO ₂ |  | Sol-gel assisted calcination | Dicyandiamide | 550 °C for 4 h | [121] |
| TiO ₂ /C ₃ N ₄ core-shell nanowire arrays |  | CVD | Melamine | 550 °C for 4 h with a temperature rise rate at 5 °C min⁻¹ | [122] |
| CQD sensitized Ti:Fe ₂ O ₃ @GCNN ^c |  | CVD | Dicyandiamide | 550 °C for 3 h with a heating rate of 2 °C min⁻¹ | [87] |
| Fe ₂ Fe-CN ₁ 900/C _A ^d |  | Pyrolysis process | Sucrose/K ₄ Fe(CN) ₆ ·3H ₂ O | Step 1: 150 °C, 7 hours; Step 2: 300 °C, 2 hours; Step III: 900 °C, 2 hours | [113] |
| PtRu/C@g-C ₃ N ₄ NS ^e |  | Pyrolysis process | CO(NH ₂) ₂ | 600 °C in nitrogen for 2 h at a heating rate of 10 °C min⁻¹ | [58] |

^aSSCN: self-sensitized carbon nitride; ^bOD-ZnO: oxygen-defective ZnO; ^cGCNN: graphitic carbon nitride nanosheets; ^dA: the “activation process”; ^eNS: nanosheet. Reproduced with permission from: ref. [101]. Copyright 2018, The Royal Society of Chemistry; Reproduced with permission from: ref. [116]. Copyright 2017, Elsevier; Reproduced with permission from: ref. [86]. Copyright 2017, Elsevier; Copyright 2017, Elsevier; Reproduced with permission from: ref. [117]. Copyright 2018, Elsevier; Reproduced with permission from: ref. [85]. Copyright 2017, Elsevier; Reproduced with permission from: ref. [89]. Copyright 2015, Elsevier; Reproduced with permission from: ref. [118]. Copyright 2018, Elsevier; Reproduced with permission from: ref. [80]. Copyright 2018, Elsevier; Reproduced with permission from: ref. [84]. Copyright 2018, American Chemical Society; Reproduced with permission from: ref. [119]. Copyright 2017, Elsevier; Reproduced with permission from: ref. [120]. Copyright 2017, Elsevier; Reproduced with permission from: ref. [83]. Copyright 2017, American Chemical Society; Reproduced with permission from: ref. [121]. Copyright 2018, Elsevier; Reproduced with permission from: ref. [122]. Copyright 2018, Springer; Reproduced with permission from: ref. [87]. Copyright 2018, The Royal Society of Chemistry; Reproduced with permission from: ref. [113]. Copyright 2016, Elsevier; Reproduced with permission from: ref. [58]. Copyright 2014, The Royal Society of Chemistry.

demonstrated g-C₃N₄ filling in multi-walled carbon nanotubes (MCNTs), then BiOI grew on the outside of MCNTs. In this case, cyanamide is first ultrasonicated and stirred in ethyl alcohol solution including MCNTs, which is critical for filling MCNTs with g-C₃N₄. After drying and heating of the mixture, MCNTs can be occupied g-C₃N₄ to form core shell g-C₃N₄/MCNTs (CM). Subsequently, BiOI can be generated and deposited on CM in the EG solution including bismuth nitrate, potassium iodide, and CM. A series of characterization images confirm that the structure of CM and BiOI kept intact, and the BiOI nanoparticles were uniformly attached on the surface of CM. Similarly, the BiOI also exhibited the uniform facet of (110) and (102) through the solvothermal strategy.

4.2. Ultrasonication-assisted self-assembly strategies

In brief, self-assembly can convert disordered molecular units into ordered composite structure. The self-assembly is a facile and broad method for preparation of catalysts, especially photocatalysts. The method has attracted much attention for applying g-C₃N₄ nanosheets coating to other different cores. Generally, the self-assembly was realized by using water or methanol as solvent. The synthetic process of

ultrasonication-assisted self-assembly can be divided into two steps, defined as a two-step self-assembly: (I) The g-C₃N₄ was exfoliated into nanosheets by ultrasonication as-prepared g-C₃N₄ aqueous solution; (II) The g-C₃N₄ nanosheets can combine with many different types of cores under different conditions, such as chemisorption, electrostatic force, and van der Waals force.

Among them, the chemisorption, as the most effective and stable method, has been used for the synthesis of core shell structured g-C₃N₄ composites. Generally, this method usually involves the mixture of g-C₃N₄ with the active ingredient accompanying stirring, evaporation of the solvent, and drying of residue. Among, the mechanism may be that an irreversible chemical bond between cores and shells is formed when the solution evaporates. Several papers have recently been reported. For example, Chen et al. [109] obtained ZnO@mpg-C₃N₄ via ultrasonication-assisted chemisorption method using the methanol as solvent. Later, Liu et al. [127] developed a highly conductive AgI core, which was obtained by a facile and general chemical reaction precipitation. With evaporation of aqueous solution, the g-C₃N₄ nanosheets regrouped into compact and stable layer because of obtaining lowest surface energy. Later, they used Ag₃PO₄ as the core to prepare the new hybrid core shell nanocomposite by the similar method [128]. The

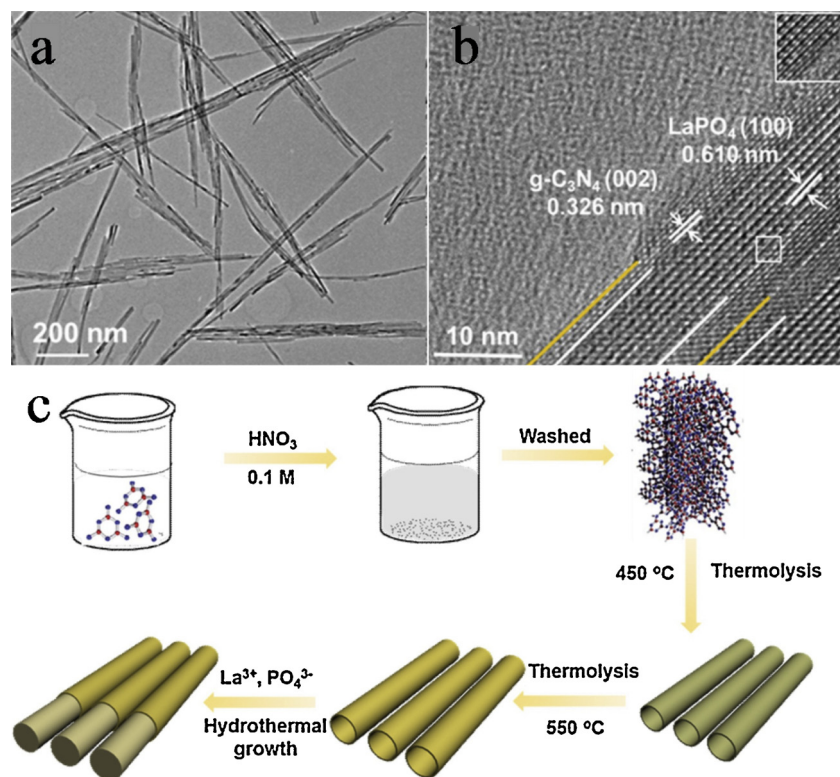


Fig. 3. The TEM image of core shell LaPO₄/tCN-200 (a); high-magnification TEM image (b) of core shell LaPO₄/tCN hybrid. (c) Synthetic process schematic of LaPO₄/tCN. Reproduced with permission from ref [86]. Copyright 2017 Elsevier.

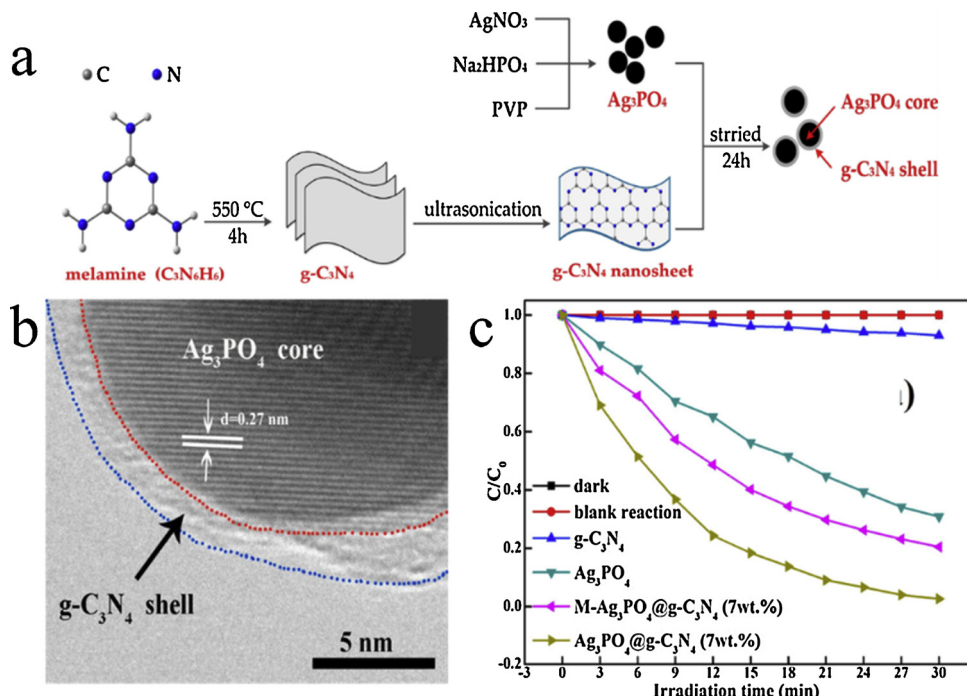


Fig. 4. (a) Schematic diagram of the preparation process for Ag₃PO₄@g-C₃N₄ core shell nanocomposites. (b) The high-magnification TEM image of Ag₃PO₄@g-C₃N₄. (c) Concentration changes of MB in different system. Reproduced with permission from ref [128]. Copyright 2016 Elsevier.

preparation process as shown in Fig. 4(a), the bulk g-C₃N₄ can be obtained by heating melamine to 550 °C for 4 h. After ultrasonication, g-C₃N₄ was exfoliated into nanosheets. The Ag₃PO₄@g-C₃N₄ hybrid structure was formed by stirring mixed solution of Ag₃PO₄ and g-C₃N₄ nanosheets for 24 h. As illustrated in Fig. 4(b), the results are made up of gauze-like g-C₃N₄ nano-sheets completely covered on spherical

Ag₃PO₄ cores. Although Ag₃PO₄ could be corroded by light and slightly dissolve in water, the core shell nanostructure can solve these problems. Moreover, Ag₃PO₄ photocatalysts possess up to 90% quantum yield of oxygen generated from water decomposition. Therefore, the Ag₃PO₄@g-C₃N₄ sample exhibited the higher photocatalytic activity compared with AgI@g-C₃N₄. The former can degrade 97% of MB after

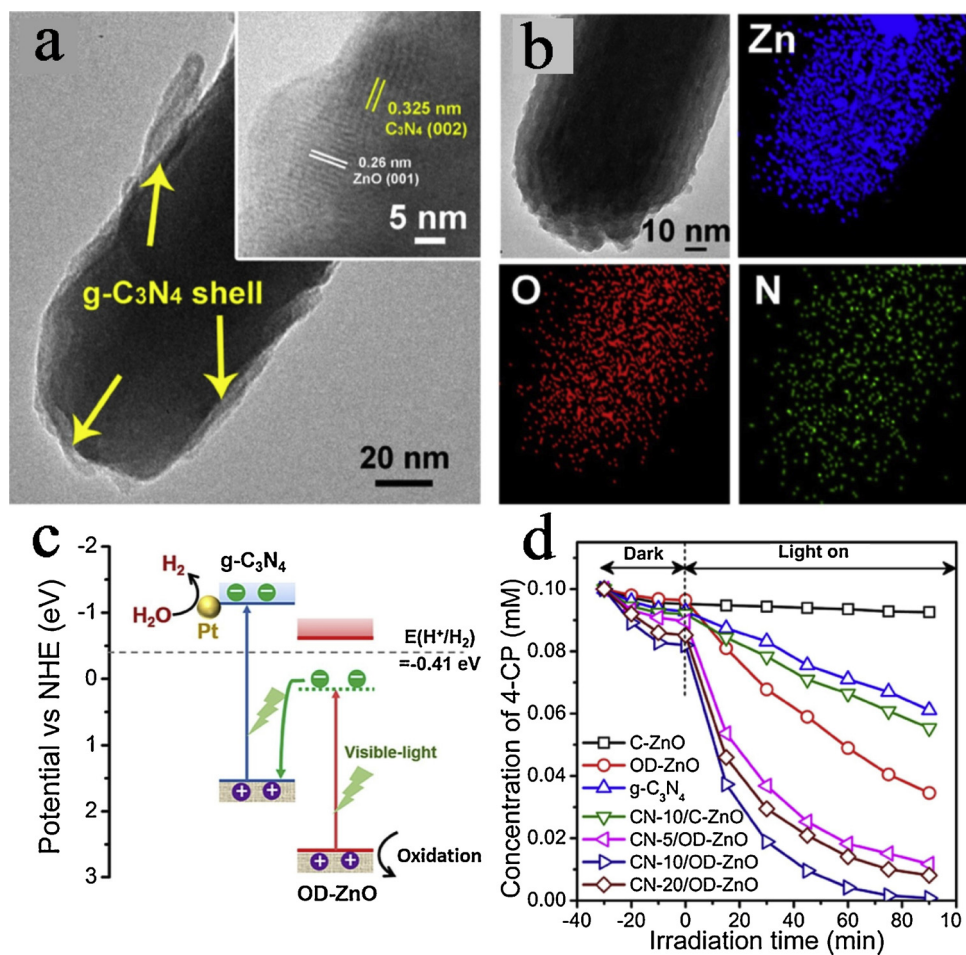


Fig. 5. HRTEM (a), and EDS mapping analysis (b) images of CN-10/OD-ZnO; Photocatalytic mechanism diagram (c) of g-C₃N₄/OD-ZnO by a Z-scheme heterojunction; (d) 4-chlorophenol degradation of different samples under visible light irradiation ($\lambda > 420$ nm). Reproduced with permission from ref [85]. Copyright 2017 Elsevier.

30 min of irradiation (Fig. 4(c)), but the latter can only degrade 96.5% MB after irradiation of visible light for 120 min.

Recently, Wang et al. [85] successfully fabricated Z-scheme heterojunction g-C₃N₄/oxygen-defective ZnO (OD-ZnO) by a chemisorption method. OD-ZnO nanorods were built through a modified solution conversion method. As shown in Fig. 5(a), the original rod-shaped OD-ZnO was wrapped with fiber-shaped g-C₃N₄ nanosheets. To further demonstrate the successful synthesis of the composites, EDS mapping analysis (Fig. 5(b)) was used to test elemental composition (cores contains oxygen and zinc; shells contains nitrogen) and FT-IR analysis confirmed that stable chemical bonds between the core and the shell. It was noted that oxygen defects were very significant to enhance photocatalytic activities. Compared with defect-free ZnO, oxygen-defects can capture the excited electrons from g-C₃N₄ at a more positive energy level. For the Z-scheme heterojunction (Fig. 5(c)), electrons of oxygen defects could combine with holes in valence band (VB) of g-C₃N₄. Therefore, the composite enhanced redox and visible-light absorbed abilities and inhibited recombination in electrons and holes. As a result, compared to g-C₃N₄ and OD-ZnO, the CN-10/OD-ZnO composites showed extremely high photocatalytic efficiency with about 95% degradation ratio in an hour (Fig. 5(d)).

In addition, Zhang et al. [103] fabricated core/shell nanowires structure by using CdS nanowires as substrate. CdS nanowires were obtained by a feasible solvothermal method. In the case, it was noted that the g-C₃N₄ nanosheets will undergo curl and reorganization process during the loading of g-C₃N₄ nanosheets on CdS nanowires. Therefore, in the methanol solution, g-C₃N₄ can physically wrap around

CdS nanowires. During the methanol volatilization, g-C₃N₄ nanosheets will smoothly coat on CdS nanowires by chemisorption process. Moreover, introducing barbituric acid into dicyandiamide precursor, which was used to synthesize g-C₃N₄, can improve its photocatalytic activities. In addition, the samples can improve light absorption performance, but reduce the BET specific surface area with added g-C₃N₄ content increasing. Liu et al. [129] reported CdS nanoparticles as templates to synthesize CdS@g-C₃N₄ core@Shell nanoparticles (NPs). In detail, in mixture of Cd(NO₃)₂ and thiourea, CdS NPs were obtained by gradually adding NaOH(aq). Then, the mixture of CdS NPs and the as-prepared g-C₃N₄ nanosheets forms the product by stirring (Fig. 6(a)). Furthermore, they use water as medium to exfoliate the bulk g-C₃N₄ because of water possessing high polarity and suitable surface energy. By comparing the above two cases, morphology (from nanowires to nanoparticles) and evaporation substance (from methanol to water) were changed, thus leading the change of heterojunction from type II to Z-scheme. This means that different interface formation methods lead to the change in charge transfer direction. Afterwards, Yao et al. [104] fabricated magnetic core-shell CuFe₂O₄@C₃N₄ through increasing reflux to promote the self-assembly process. The CuFe₂O₄ NPs were synthesized by a hydrothermal method. However, compared to pure g-C₃N₄, the g-C₃N₄ in the core shell composite has lower thermal stability, which may be attributed to the CuFe₂O₄ NPs influencing cross-linked rings of g-C₃N₄ nanosheets.

Different from the above methods, Dang et al. [130] developed the electrostatic force to prepared core shell structure. The synthesis procedure is illustrated in Fig. 6(b). First, the g-C₃N₄ was immersed in HCl

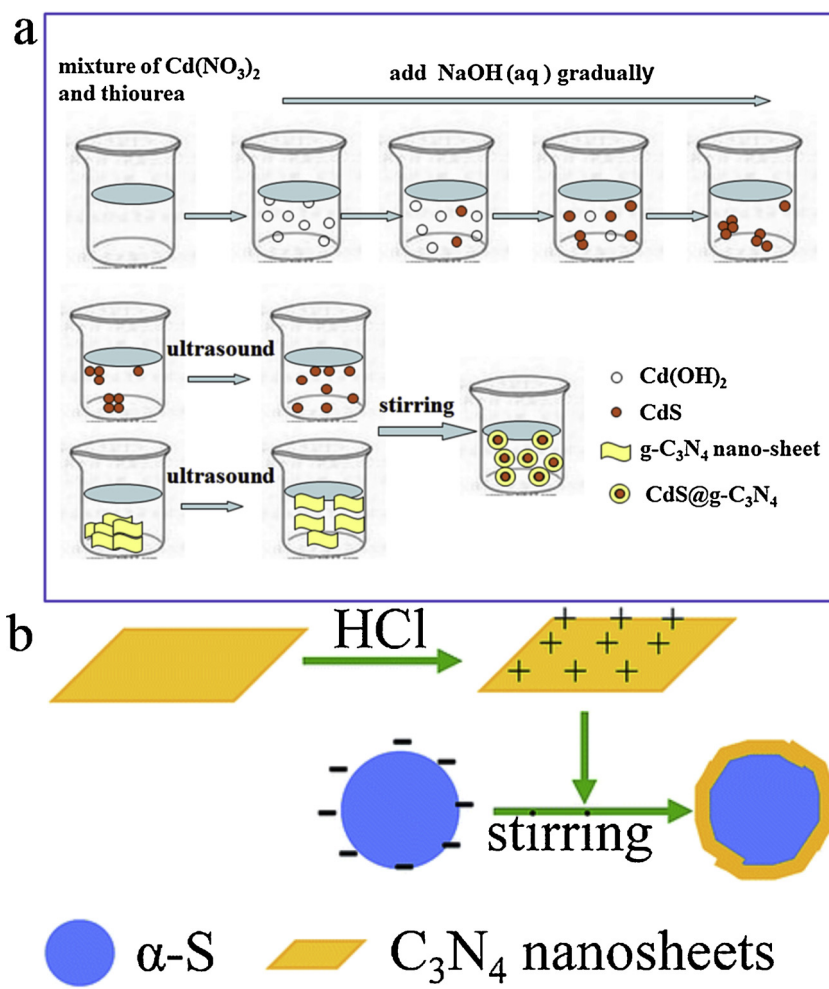


Fig. 6. (a) Synthetic schematic for CdS and CdS@g-C₃N₄; Reproduced with permission from ref [129]. Copyright 2017 Elsevier. (b) Synthetic schematic for α-S@g-C₃N₄. Reproduced with permission from ref [130]. Copyright 2015 The Royal Society of Chemistry.

(0.5 mol L⁻¹) for 1 h to make its surface positive. Next, the mixture was slowly added to the α-S solution with the negative outer surface charge. Accompanied by stirring, the products were obtained by electrostatic interaction between α-S and ultra-thin g-C₃N₄ nanosheets. From the SEM images, the loose combination between g-C₃N₄ shells and the α-S may be attributed to the weak electrostatic force. Afterwards, van der Waals force was also used as a driving force to self-assemble into g-C₃N₄ CSNs. Pan et al. [131] grown C₃N₄/BiPO₄ nanorods via the two-step self-assembly process. In the second step, the BiPO₄ nanorods were added into the methanol solution containing ultrathin g-C₃N₄ nanosheets, and then the g-C₃N₄ nanosheets spontaneously assembles on the outer surface of the BiPO₄ nanorods by van der Waals forces. Because the lattice match between the BiPO₄ and C₃N₄, which are demonstrated by XRD and TEM, the core shell composite with strong interaction was obtained. Interestingly, the smooth carbon nitride coating showed increasing coverage, improved crystallinity and light absorption intensity with increasing g-C₃N₄ content.

4.3. Heat treatment

Heat treatment is the most popular and extensive method for using g-C₃N₄ precursors to construct core shell structure due to the synthesis of g-C₃N₄ and the rupture of g-C₃N₄ nanosheets occurring at high temperatures. The heat treatment can be divided into calcination, sol-gel assisted, chemical vapor deposition (CVD), and pyrolysis process. Whether in photocatalysis or photocatalysis and electrocatalysis, it is widely used.

4.3.1. Calcination

In general, the precursors were heated at around 500 °C for several hours through a condensation pathways for forming g-C₃N₄. Calcination is a necessary process by precursors to prepare g-C₃N₄. Correspondingly, the calcination methods can be widely applied for constructing core shell structured g-C₃N₄ with urea, cyanamide (CA), dicyanamide or melamine as the precursor. It was noting that template selection is vital to construct core shell structure of different shape. In the section, content includes spherical core template and non-spherical core template.

3.3.1.1 Spherical core templates. While the ball as the core, the cover layer is easy to adhere and can be uniformly attached. Bo et al. [132] fabricated SiO₂/g-C₃N₄ nanomaterials by calcining CA molecules on the SiO₂ spherical substrate, which were synthesized by the mixture of tetraethyl orthosilicate (TEOS) solution and aqueous ammonia solution. As illustrated in Fig. 7(a), when TEOS ethanol and water solution was stirred, TEOS was hydrolyzed, followed by forming SiO₂ nanospheres of around 200–300 nm diameter. Meanwhile, it can be observed that the growth of hydroxyl group on the outer surface of SiO₂ nanospheres. After the CA solution was added into the above liquid, –OH group could combine with CA, leading to CA tightly enwrapping SiO₂ nanospheres. In the final step, the calcination of mixture can make CA convert to g-C₃N₄ and let g-C₃N₄ and SiO₂ core more tightly combined. Previously, the g-C₃N₄ based composites were prepared by the first synthesis of pure g-C₃N₄. The strategies may result in loose combination between core and shell. Le et al. [133] explored a novel and facile method to prepare ZnO@g-C₃N₄ by two-step calcination. In this

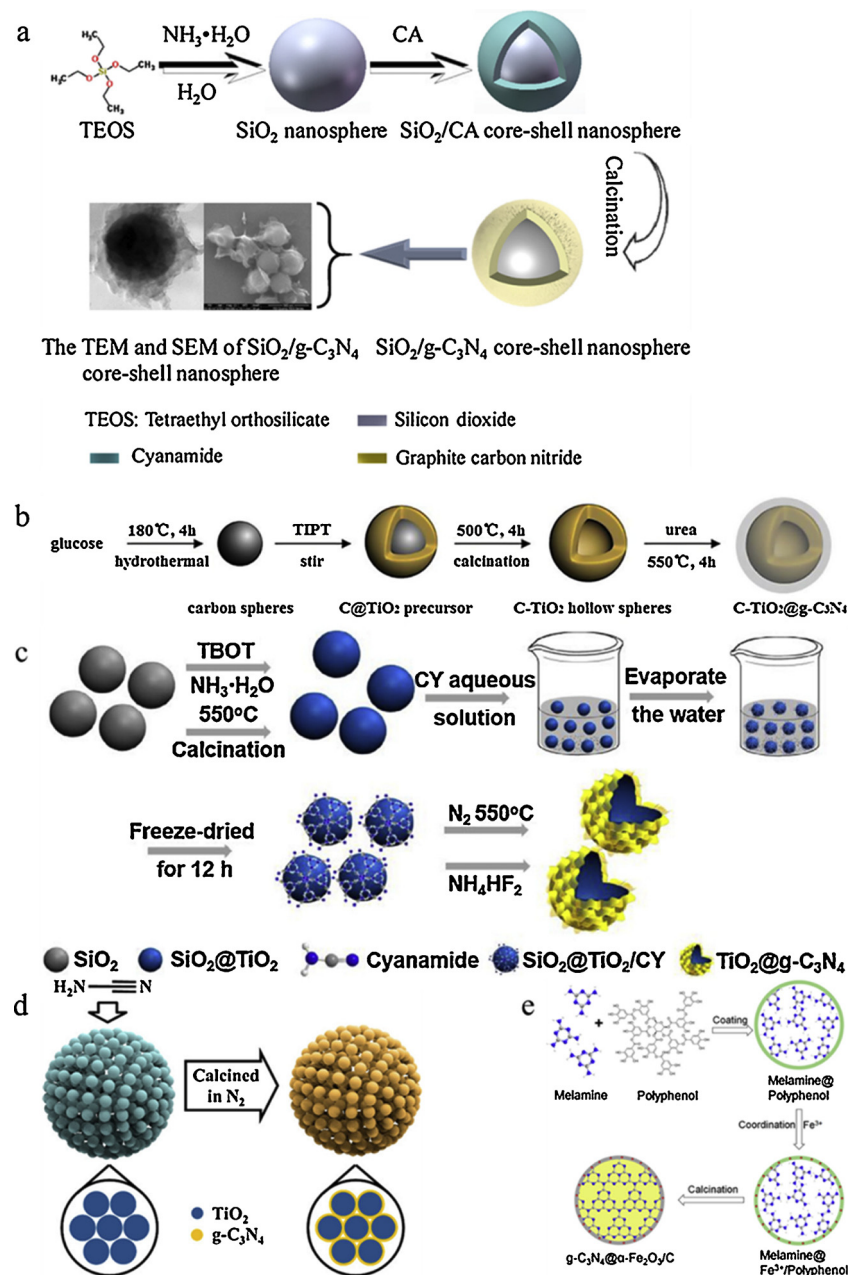


Fig. 7. (a) Synthetic schematic for $\text{SiO}_2/\text{g-C}_3\text{N}_4$. Reproduced with permission from ref [132]. Copyright 2015 Elsevier. (b) Synthetic schematic for C-doped $\text{TiO}_2/\text{g-C}_3\text{N}_4$. Reproduced with permission from ref [79]. Copyright 2017 Elsevier. (c) Synthetic schematic for hollow $\text{TiO}_2/\text{g-C}_3\text{N}_4$. Reproduced with permission from ref [80]. Copyright 2018 Elsevier. (d) Synthetic schematic for Mesoporous $\text{TiO}_2/\text{g-C}_3\text{N}_4$ Microspheres. Reproduced with permission from ref [83]. Copyright 2017 American Chemical Society. (e) Synthetic schematic for $\text{g-C}_3\text{N}_4/\text{g-C}_3\text{N}_4/\text{Fe}_2\text{O}_3/\text{C}$. Reproduced with permission from ref [84]. Copyright 2018 American Chemical Society.

method, the urea precursor can in situ grow on as-fabricated ZnO surface by calcination. Shen and co-workers [99] reported the preparation of high photocatalytic active material via in situ grow procedure with urea as precursor under 550°C for 2 h. The preparation of SnO_2 microspheres is the primary requirement for the construction of subsequent $\text{SnO}_2/\text{g-C}_3\text{N}_4$ core shell composites. In this process, the SnCl_4 and D-glucose anhydrous were mixed in the aqueous solution of ethanol. The above solution firstly generated precipitation by hydrothermal, followed by post-annealing at 550°C . Compared with ZnO particles with 30–50 nm diameter in the previous example, the samples possess a larger core with $1.5\text{ }\mu\text{m}$ particle size. Moreover, it is beneficial to inhibit photogenerated electrons and holes recombination. As a result, photocatalytic activities were significantly enhanced.

More interesting, Zou and co-workers [79] successfully fabricated C-doped $\text{TiO}_2/\text{g-C}_3\text{N}_4$ nanocomposites using urea as precursor. In the

work, the synthetic process (Fig. 7(b)) involves first preparing C-doped TiO_2 hollow spheres by using carbon nanospheres as a template and subsequent making urea in-situ grow on the C-TiO₂ surface through a heat-treatment. Different from sealed core shell structure, the resultant with hollow core shell structure possesses higher visible light absorption due to quantum being used efficiently through multiple reflection. Besides, the special structure has many characteristics, such as easy diffusion, high light utilization, and quite low density. From the XRD curves, it can be found that the calcination can enhance the crystallinity of the finished product. Apart from carbon nanospheres as template, SiO_2 nanoparticles were also applied for constructing hollow core shell structure. Guo et al. [80] firstly engineered $\text{TiO}_2/\text{g-C}_3\text{N}_4$ hollow core@shell composites by in-situ growth and calcination. As illustrated in Fig. 7(c), tetrabutyl titanate molecules and cyanamide are the precursor of TiO_2 and $\text{g-C}_3\text{N}_4$, respectively. On the other hand, SiO_2 templates

were removed by NH_4HF_2 solution.

Different from TiO_2 hollow spheres, Wei et al. [83] used the mesoporous anatase TiO_2 microspheres (TO) as cores to form composites. The TO coated by cyanamide was calcined to obtain the mesoporous $\text{TiO}_2/\text{g-C}_3\text{N}_4$ microspheres (Fig. 7(d)). The mesoporous structure can reduce band gap energy and be beneficial to mass transfer because of a large number of pores. Therefore, this special structure is suitable for photocatalytic degradation of pollutants.

In addition to enabling grow outside the core, $\text{g-C}_3\text{N}_4$ can be integrated into other materials. For example, Wu et al. [84] synthesized $\text{g-C}_3\text{N}_4@\alpha\text{-Fe}_2\text{O}_3/\text{C}$ core@shell photocatalysts by calcination. The general steps are shown in Fig. 7(e). At the beginning, melamine is covered by polyphenol to form preliminary core shell structure. After the introduction of iron ions, the mixtures carry out polymerization and oxidation reaction by calcination, so the final product was obtained. The $\alpha\text{-Fe}_2\text{O}_3$ and C moiety of the unique shell can be regarded as hole oxidation sites and electron transfer site, respectively.

3.3.1.2. Non-spherical core templates. The shapes of such templates include nanorod arrays [88,120,134], hexagonal prism [119], nanosheets [56], and flower-like [118]. Some excellent semiconductors are more difficult to synthesize spheres, so it is a good choice to build non-spherical core-shell composites. In addition, when the core-shell structure is used as an electrode, the nanorod shape is more suitable than the spherical shape because the electron transfer path is shorter and the resistance is smaller. At present, employing nanorod arrays as the template in calcination is an extensive and promising route to obtain $\text{g-C}_3\text{N}_4$ based core shell structure. In this work, FTO-coated glass substrates generally act as a carrier in arranging nanorod arrays. Hao and co-workers [120] successfully synthesized $\text{TiO}_2@\text{g-C}_3\text{N}_4$ nanorod arrays using heptazine as precursor via saturated aqueous solution as heat transfer medium. As showed in Fig. 8(a), the samples were gradually formed from the inside to the outside by a three-step thermal deposition process. From the previous studies, when used as the sole

precursor to prepare carbon nitride, melamine is easily sublimed at higher temperatures. Therefore, the central step, namely, a big and stable heptazine synthesized by the condensation of melamine in the polar solution with HNO_3 , played a crucial role in preventing sublimation during the reaction and making the ultrathin $\text{g-C}_3\text{N}_4$ shells tightly wrapped around the TiO_2 cores of rutile and single crystalline. In the field of photoelectrochemical, Chen et al. [88] designed siliconnanowire (SiNW)/ $\text{g-C}_3\text{N}_4$ core shell nanoarrays by heating a cyanamide solution impregnated with SiNW nanoarrays (Fig. 8(b)). The novel method of metal-catalyzed electroless etching (MCEE) was applied for preparing SiNW nanoarrays. Briefly, the as-prepared clean n-Si wafers was washed by water and acetone, followed by using H_2SO_4 and H_2O_2 to remove organics. Then, the Si was etched by a HF-AgNO_3 solution, leading to part Ag crystal remaining on Si nanoarrays. In order to obtain pure Si nanoarrays, they used the oxidant solution to treat it. The size of SiNW nanoarrays was derived by the etching time. SiNW nanoarrays become rough but its dimension has not been affected. The intimate interfacial contact was confirmed by the TEM and HRTEM images. The as-fabricated resultant exhibited higher PEC performance compared to SiNW nanoarrays and FTO/ $\text{g-C}_3\text{N}_4$ due to the formation of heterojunction between the SiNW and $\text{g-C}_3\text{N}_4$.

Recently, Yang et al. [119] firstly applied Lanthanide-doped upconversion nanoparticles (UPNS) to construct the core shell structured $\text{g-C}_3\text{N}_4$ nanocomposites with hexagonal prism by a facile two-step method. The UPNS can improve solar energy utilization due to more visible light absorption and its upconversion capabilities. In this case, NaYF_4/CM was synthesized by using melamine, EDTA, $\text{NaYF}_4\text{-Yb,Er}$, and cyanuric acid as precursor through a molecular self-assembly process (Fig. 8(c)). The NaYF_4/CM was calcined at 550 °C under N_2 atmosphere. Moreover, the solvents will also influence the morphology of CM supramolecular, such as the rod-like and needle-like CM adducts which are fabricated by using water and chloroform as solvents, respectively.

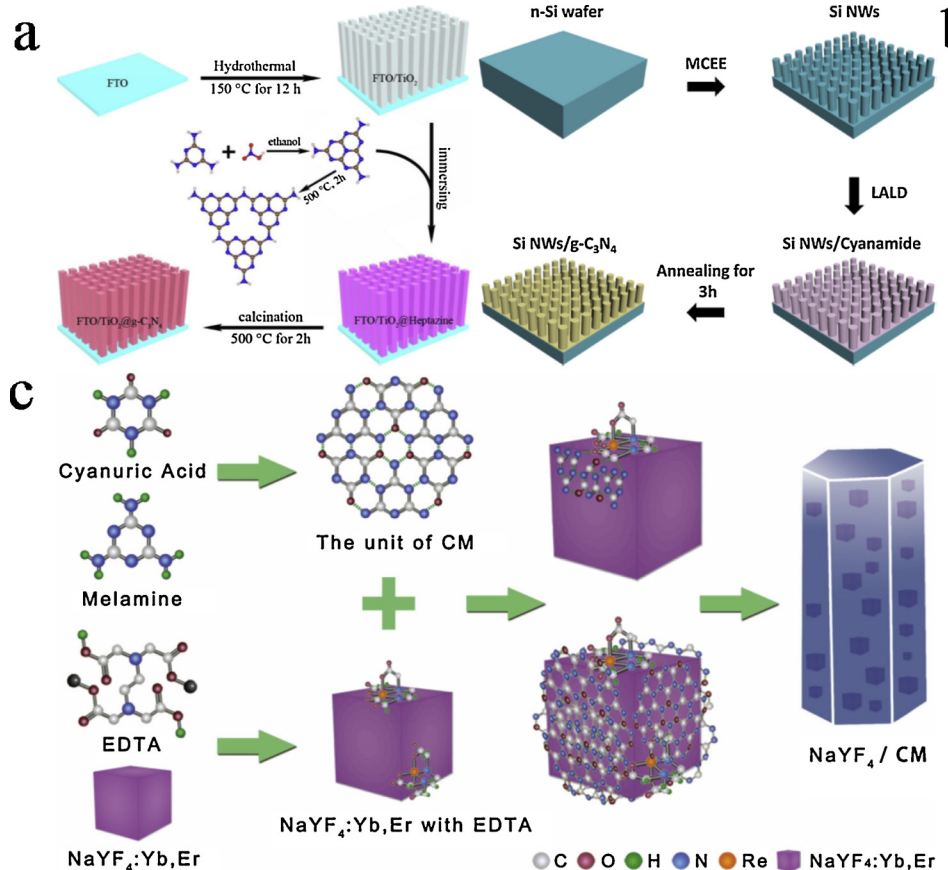


Fig. 8. (a) Synthetic schematic for $\text{TiO}_2@\text{g-C}_3\text{N}_4$ nanorod arrays. Reproduced with permission from ref [120]. Copyright 2017 Elsevier. (b) Synthetic schematic for SiNW/ $\text{g-C}_3\text{N}_4$ core shell nanoarrays. Reproduced with permission from ref [88]. Copyright 2017 Elsevier. (c) Possible synthetic schematic for NaYF_4/CM . Reproduced with permission from ref [119]. Copyright 2017 Elsevier.

BiVO_4 is a popular semiconductor and known for its unique flower shape. By using the pre-prepared Eu doped $\text{g-C}_3\text{N}_4$ nanosheets as shell and flower-like BiVO_4 as core, Wang et al. [118] demonstrated the synthesis of Eu-CN@BiVO_4 core-shell structured composites, in which $\text{g-C}_3\text{N}_4$ can reduce the valence band from 1.58 to 1.43 eV and improve the conduction band from -1.26 to -1.11 eV by doping. These modifications can increase the light absorption edge of $\text{g-C}_3\text{N}_4$ from 430 to 509 nm. Moreover, the Eu doped $\text{g-C}_3\text{N}_4$ nanosheets can significantly increase the specific surface area of BiVO_4 core. The results indicate that the photocatalytic activity of samples is obviously enhanced due to conversion between Eu(III) and Eu(II) achieving more O^{2-} generating.

4.3.2. Sol-gel assisted calcination

Recently, the sol-gel method combined with calcination method can obtain a strongly connected core shell structure. Ma and co-workers [135] reported the sol-gel process for the synthesis of carbon@ $\text{g-C}_3\text{N}_4$ core shell structure. They realized that the bulk $\text{g-C}_3\text{N}_4$ cannot be covered on C cores. Hence, by using nitric acid (HNO_3) treatment, the $\text{g-C}_3\text{N}_4$ surface chargeability would change, and protons can be prone to embed in the $\text{g-C}_3\text{N}_4$ solid with the layered structure, followed by selectively located on the skeleton N atoms by the similar basic interaction. The preparation process of carbon@ $\text{g-C}_3\text{N}_4$ core shell structure was illustrated in Fig. 9(a). In detail, the $\text{g-C}_3\text{N}_4$ sol was prepared by protonation of bulk $\text{g-C}_3\text{N}_4$ with HNO_3 because the strong oxidant can lead to the depolymerization of $\text{g-C}_3\text{N}_4$. After removing HNO_3 , the $\text{g-C}_3\text{N}_4$ colloids can carry out repolymerization by constructing hydrogen carbon. Afterwards, carbon spheres and $\text{g-C}_3\text{N}_4$ gel was mixed, followed by drying and calcining to get Carbon@ $\text{g-C}_3\text{N}_4$. It is noted that the gel was fabricated by spontaneous self-assembly process due to electrostatic force from negatively charged carbon and positively charged $\text{g-C}_3\text{N}_4$. The as-prepared structure improves the surface area of monomer component. It indicates that the sol-gel method can contribute to synthesizing core shell structure. Similarly, Wang et al. [121] explored a novel combination method to obtain $\text{g-C}_3\text{N}_4@\text{TiO}_2$ core shell nanostucture with adjustable ultrathin $\text{g-C}_3\text{N}_4$ shell. Fig. 9(b) roughly illustrated the different stages during fabrication of $\text{g-C}_3\text{N}_4@\text{TiO}_2$ photocatalysts. During the heating process, the precursors undergo the surface area and phase alternation, and adjustable polymerization connected by a new bond. Moreover, the thickness of the $\text{g-C}_3\text{N}_4$ layer can be facilely tuned from 1.0 nm to 3.0 nm by adjusting the annealing temperature from 550 °C to 400 °C. As a result, the as-fabricated sample under 550 °C was provided with the thinnest thickness, the strongest light absorption and the better photocatalytic performance. The report successfully revealed the structure-activity relationship between the core shell structure with different shell thickness and the corresponding catalytic activity.

Mohamed and co-workers [136] also developed the sol-gel assisted heat treatment to synthesize $\text{g-C}_3\text{N}_4@\text{C}$, N co-doped TiO_2 with anatase/rutile mixed phase. It should be pointed out that the condition for the formation of core shell structure is that the annealing temperature reaches or exceeds 550 °C, which is good for the breakage of 2D $\text{g-C}_3\text{N}_4$ nanosheets into short-range order (Fig. 9(c)). According to the XPS, it can be found that urea as $\text{g-C}_3\text{N}_4$ precursor can make the TiO_2 core doped by C and N element. Although high temperature can get well-formed core shell structure, it can also destroy the porous structure of the $\text{g-C}_3\text{N}_4$, thus reducing the overall porosity. This is a common trouble associated with the sol-gel assisted heat treatment.

4.3.3. CVD method

Chemical vapor deposition (CVD) is an efficient and highly positioned method to enable the vapor precursors depositing on the template of relative high temperature. This method is widely used to construct core shell structure in the fields of photocatalysis and photoelectrocatalysis. Correspondingly, Park et al. [137] first demonstrated that the coating of $\text{g-C}_3\text{N}_4$ nanosheets on ZnO nanorod arrays by CVD. In the first step, neat ZnO nanorod arrays were synthesized on

FTO-coated glass by seed-mediated growth. In the two step, melamine occur polymerization under the air atmosphere at 520 °C, thus forming the $\text{g-C}_3\text{N}_4$ layer coating on ZnO nanorods. However, with the $\text{g-C}_3\text{N}_4$ content increasing, it tends to gather on the top of ZnO nanorods. In case of excessive aggregation, photo-generated electrons and holes are easy to combine. CVD not only allows the synthesis of photocatalysts, but also bears great potential for core shell structured photo-electrodes. Yi et al. [57] fabricated Ti-doped $\text{Fe}_2\text{O}_3@\text{g-C}_3\text{N}_4$ nanosheets (Ti: $\text{Fe}_2\text{O}_3@\text{GCNN}$) supported carbon quantum dots (CQDs) as photoanodes for water splitting. The synthesis procedure is illustrated in Fig. 10(a). In the first step, $\text{Ti:Fe}_2\text{O}_3$ was obtained on FTO via a calcination and a hydrothermal method. Next, vapor containing dicyandiamide aggregated on the Ti-doped Fe_2O_3 surface by CVD. Finally, CQDs coated on the as-prepared $\text{Ti:Fe}_2\text{O}_3@\text{GCNN}$. The FESEM (Fig. 10(b)) show the size of the core in a few hundred nanometers and the growth direction of Fe_2O_3 . Fig. 10(c) exhibited the loading of ultra-small CQDs and thin layers of the GCNNs does not affect the framework of the photoelectrode. It is worth mentioning that Ti-dopant can impede the recombination of charge due to the anodic-shifted flat band potential. The $\text{g-C}_3\text{N}_4$ nanosheets and CQDs can facilitate charge separation, perfect the kinetics, increase the donor density, and improve photocurrent density due to their high conductivity and low resistance between electrode and electrolyte. Similarly, Wang and co-workers [122] designed $\text{TiO}_2/\text{g-C}_3\text{N}_4$ core-shell nanowire arrays without CQDs with TiO_2 seed as a precursor by the hydrothermal and CVD method.

4.3.4. Pyrolysis process

Pyrolysis process of hybrid inorganic-organic mixed precursors is a typical and popular method to obtain the electrocatalysts (ECs) for improving oxygen reduction reaction (ORR) in the fuel cells. Because of core shell structure ECs with the best performance, their preparation is also becoming popular. Given the carbon nitride materials with rich N-ligands and C-ligands constituting coordination nest, it is a suitable material as the shell in ECs, which can embed active metals and co-catalysts. The ECs fabricated by the following three steps. First, various related reagents are dissolved and homogenized by sonication in a uniform solvent. Afterwards, the hybrid inorganic-organic mixed precursors form "pristine" ECs by pyrolysis process. In the final step, "activated" ECs was obtained by activation process. In general, the pyrolysis process composed of three steps, in which the temperature increases step by step. The detail as follows: (I) 120–200 °C for 12–24 h or less to remove completely all the residues of solvents; (II) 300–400 °C for 2 h to remove hetero atom (e.g. H and O) from materials and form a hybrid carbon-rich precursor; (3) 500–900 °C for 2 h, temperature regulation in this section is constant, but sometimes is gradient, which depend on the material [138,139].

At the beginning, Vezzù and co-workers [113] successfully prepared the ECs with Fe-carbon nitride (CN) as shell and carbon nanoparticles as core by typical pyrolysis process. They used different ratios of $\text{K}_4\text{Fe}(\text{CN})_6\cdot 3\text{H}_2\text{O}$ and FeCl_3 as Fe source to mix with sucrose and XC-72R nanoparticles and then homogenized by sonication, followed by drying and pyrolysis process for obtaining the "pristine" CN-based ECs. Then, the "activated" CN-based EC was obtained by an activation process. Compared with the "pristine" ECs, the "activated" ECs possesses thin shell and high porosity. It should be noted that using different ratios of $\text{K}_4\text{Fe}(\text{CN})_6\cdot 3\text{H}_2\text{O}$ and FeCl_3 to introduce Fe species will influence the Fe and N mass ratio of the "pristine" and "activated" ECs. In general, the product with high N-ligands can have good hydrophilicity. Especially, high $\text{N}_x\text{-Fe}$ coordination species in the product can facilitate oxygen absorption. CN has an excellent structure to expose Fe species on the outer surface, which provide generous active sites for ORR.

To further enhance the ORR performance, the ECs with alloy appear. Negro et al. [114] reported the preparation of Fe-Sn carbon nitride (CN) as a shell coating on graphene nanoplatelets (GNPs) for the oxygen reduction reaction (ORR) in the cathode of Pt-free anion-exchange membrane fuel cells. Among, the activation process involves

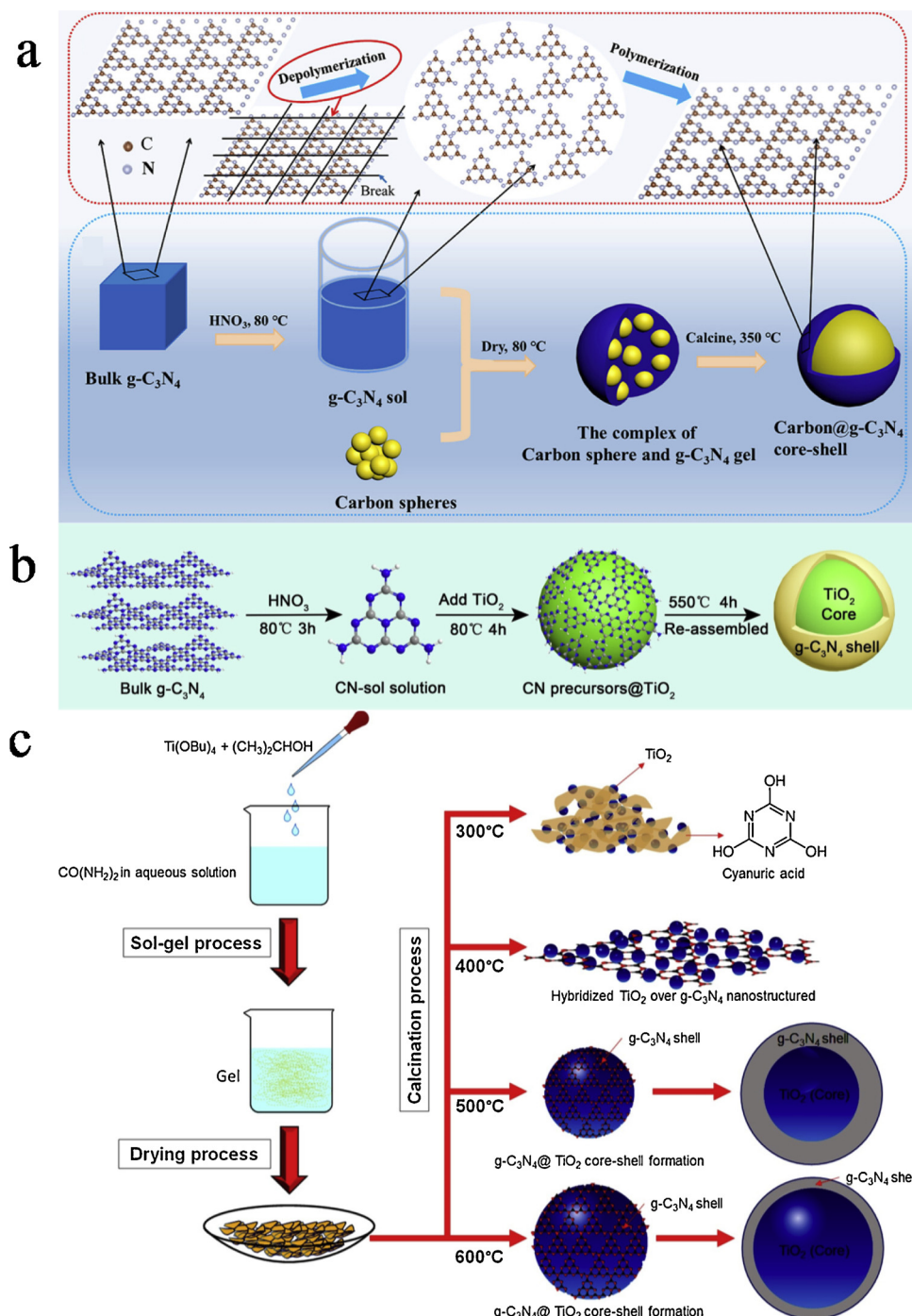


Fig. 9. (a) Synthetic schematic for carbon@g-C₃N₄ photocatalyst. Reproduced with permission from ref [135]. Copyright 2017 American Chemical Society. (b) Synthetic schematic for g-C₃N₄@TiO₂ photocatalyst. Reproduced with permission from ref [121]. Copyright 2018 Elsevier. (c) Synthetic schematic for the g-C₃N₄/TiO₂ photocatalyst. Reproduced with permission from ref [136]. Copyright 2018 Elsevier.

treating with HF for 2 h and subsequently carrying out 900 °C for 2 h (Fig. 11(A)). From the ICPAES results and elemental analysis, we can initially determine that the graphitization degree of CN increased after activation, because hetero atom mass ratio reduced and unstable metal-based nanoparticles without entering coordination nest was removed by high temperature. This can also be observed through HRTEM images (Fig. 11(B)). In few cases, the CN shell still exist the onion-like features, which can block the destruction of underneath NPs (< 100 nm). With respect to conventional Pt/C reference, the thermal stability of Pt-free ECs was improved, but their performance still was insufficient. In general, the platinum-group metal (PGM) based alloys ECs with CN as

the shell was synthesized by two different precursors. The first precursor with hybrid inorganic-organic polymer networks composes of metal coordination macromolecular polymeric organics, such as polyacrylonitrile (PAN). The other precursor with zeolitic inorganic-organic polymer electrolyte (Z-IOPE) is consisted of multiple metal centers connected by small molecular organics, such as sucrose. Negro and co-workers [140] reported a novel PdCoNi-CN_xTf/G ECs by a traditional pyrolysis. The core shell structured ECs are consisted of the carbon nanoparticles (NPs) core and the shell of carbon nitride (CN) embedding Pd as active sites and Co and Ni as co-catalysts. They synthesized four samples under two different pyrolysis temperatures (600 °C, 900

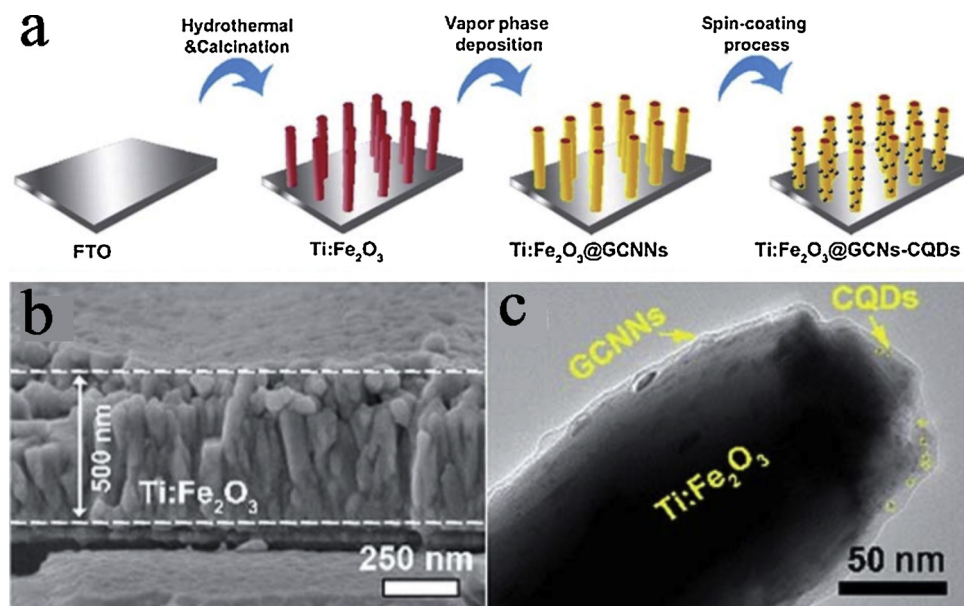


Fig. 10. (a) Synthetic schematic for Ti:Fe₂O₃@GCNN-CQDs nanoarrays. (b) cutaway view of Ti:Fe₂O₃. (c) TEM images of Ti:Fe₂O₃@GCNN-CQDs. Reproduced with permission from ref [57]. Copyright 2018 The Royal Society of Chemistry.

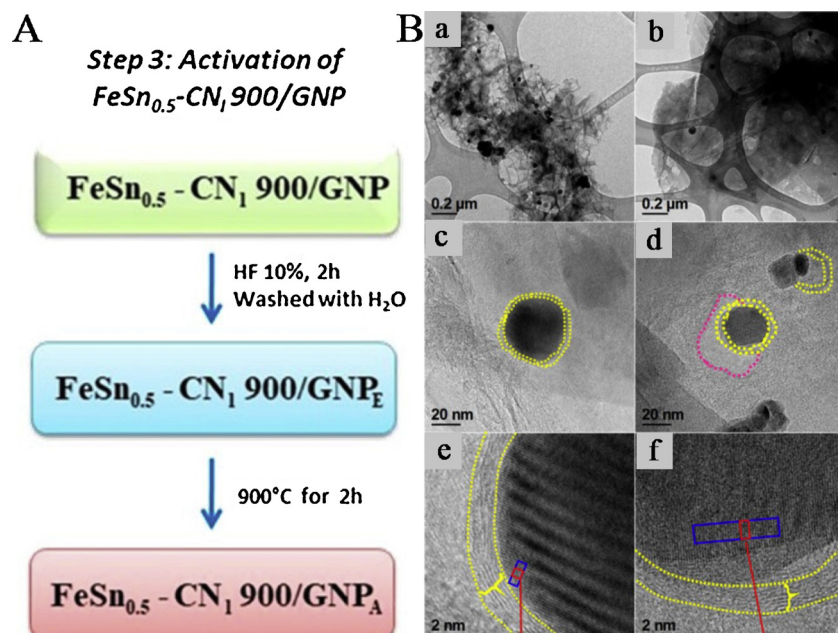


Fig. 11. (A) Activation process for FeSn_{0.5} - CN₁ 900/GNP_A ECs. (B) HRTEM images of (a, c, e) FeSn_{0.5} - CN₁ 900/GNP and (b, d, f) FeSn_{0.5} - CN₁ 900/GNP_A in a gradually expanding multiple. Reproduced with permission from ref [114]. Copyright 2018 American Chemical Society.

°C) and two different precursor binder (PAN, sucrose). Compared with PAN as binder, the sample from the sucrose will possess higher N content, which are the key points for constructing metal-N ligands. Correspondingly, as the temperature rises from 600 to 900 °C, the Pd-based active sites of the CN shell will increase. Therefore, it is crucial for the performance of ECs that the increase of N content in CN shell due to Pd mainly binding to N species.

5. Applications

5.1. Photocatalytic applications

5.1.1. Photocatalytic hydrogen evolution

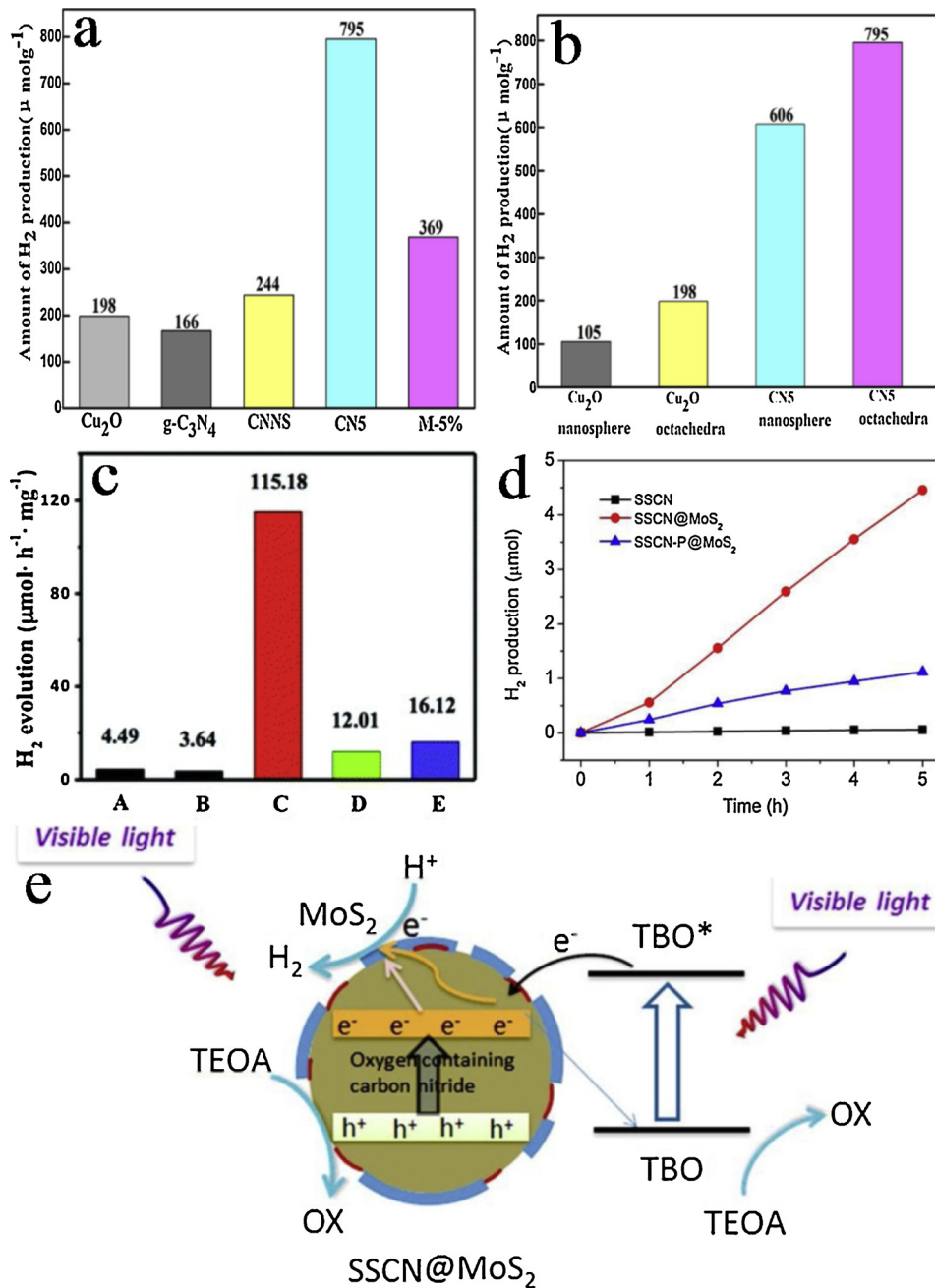
With the rapid development of society and excessive exploitation of

non-renewable energy, there is an urgent need to develop sustainable energy, such as solar energy. By simulating the natural photosynthetic system, hydrogen, as a clean energy source, can be successfully obtained by artificial photocatalytic decomposition of water. The g-C₃N₄, as the promising photocatalysis, of practical applications is hindered due to poor photocatalytic hydrogen evolution. In order to solve low visible light absorption and easy recombination of photogenerated electron hole pairs, the construction of core shell structured g-C₃N₄ based photocatalysts has caused great attention. The g-C₃N₄-based core shell structure photocatalysts for hydrogen evolution were generally summarized in Table 3.

Bai et al. [141] evaluated the effect of noble metal Ag as core. The optimum Ag@C₃N₄ photocatalysts demonstrated excellent photocatalytic performance for hydrogen production, which was

Table 3A summary of $\text{g-C}_3\text{N}_4$ -based core shell structure photocatalysts for hydrogen evolution.

| Materials/($\text{g-C}_3\text{N}_4$ wt%) | Sacrificial agents | Light sources | Photoactivity ($\mu\text{mol g}^{-1} \text{h}^{-1}$) | Ref. |
|---|--|---|--|-------|
| Hollow- $\text{CdS}@\text{g-C}_3\text{N}_4$ / (5%) | Na_2S and Na_2SO_3 | 300 W Xe lamp $\lambda > 400 \text{ nm}$ | 4390 | [102] |
| Mesoporous $\text{TiO}_2@\text{g-C}_3\text{N}_4$ hollow core@shell | CH_3OH | 300 W Xe lamp equipped with AM 1.5 filter | 197.5 | [80] |
| C-doped $\text{TiO}_2@\text{g-C}_3\text{N}_4$ core-shell Hollow nanospheres | CH_3OH | 300 W Xe lamp $\lambda > 420 \text{ nm}$ | 35.6 | [79] |
| $\text{CdS}@\text{g-C}_3\text{N}_4$ / (3%) | Na_2S and Na_2SO_3 | 350 W Xe lamp $\lambda \geq 420 \text{ nm}$ | 10.89 mmol g^{-1} | [129] |
| $\text{g-C}_3\text{N}_4/\text{OD-ZnO}^a$ | TEOA ^b | 300 W Xe lamp $\lambda > 420 \text{ nm}$ | – | [85] |
| SSCN ^c @ MoS_2 / (4%) | TEOA ^b | MAX-302 xenon lamp $\lambda > 420 \text{ nm}$ | 91 | [116] |
| $\text{CdS}/\text{g-C}_3\text{N}_4$ | Na_2S and Na_2SO_3 | 300 W Xe lamp $\lambda > 420 \text{ nm}$ | 115180 | [125] |
| $\text{Cu}_2\text{O}/\text{g-C}_3\text{N}_4$ octahedra / (5%) | TEOA ^b | 300 W Xe lamp $\lambda > 420 \text{ nm}$ | 265 | [89] |
| $\text{Ag}@\text{C}_3\text{N}_4$ | TEOA ^b | 300 W Xe lamp $\lambda > 420 \text{ nm}$ | 25 | [141] |
| $\text{CdS}/\text{g-C}_3\text{N}_4$ Nanowires / (2%) | Na_2S and Na_2SO_3 | 350 W Xe lamp $\lambda \geq 420 \text{ nm}$ | 4152 | [103] |
| $\text{Zn}_{0.8}\text{Cd}_{0.2}\text{S}@\text{g-C}_3\text{N}_4$ / (10%) | Na_2S and Na_2SO_3 | 300 W Xe lamp $\lambda > 420 \text{ nm}$ | 2351.18 | [142] |

^aOD-ZnO: oxygen-defective ZnO; ^bTEOA: Triethanolamine; ^cSSCN: self-sensitized carbon nitride.

approximately 30-fold increase compared to pure g-C₃N₄ (0.84 μmol for 10 h). This result is attributed to two factors: Ag core as electron capture agent can reduce recombination of charge carriers due to its low Fermi level and the formation of hydrogen resolution sites. The photocatalysts with different exposed crystal face will have different photocatalytic activity. Li and co-workers [89] explored the effect on photocatalytic hydrogen evolution of two Cu₂O shapes (nanosphere and octahedral). The authors claimed the H₂ evolution rate of Cu₂O@g-C₃N₄ composites reached up to 795 $\mu\text{mol/g}$ at 3 h, which is much higher than Cu₂O and g-C₃N₄ moiety (Fig. 12(a)). In addition, the H₂ production of Cu₂O octahedral is 198 μmol after 3 h, which is about 2 times higher than Cu₂O nanosphere (105 μmol) (Fig. 12(b)). Mechanism is attributed to the factor that octahedral Cu₂O with the exposed (111) face has higher surface energy and more active sites than Cu₂O nanosphere due to it containing surface Cu atoms with dangling bonds. Thus, combining completely exposed highly active faces with g-C₃N₄ is a novel way to achieve high photocatalytic hydrogen production efficiency.

Despite the great efforts have been made to improve hydrogen production activity by the core shell heterostructure, the goal of being low-cost and enabling large-scale production has not been achieved. After further exploration, Yan et al. [125] demonstrated the performance improvement by introducing co-catalyst. Interestingly, the normal CdS/g-C₃N₄ core shell nanowires become active toward H₂ evolution by Ni(OH)₂ modification. The optimal CdS@g-C₃N₄ with Ni(OH)₂ as co-catalyst produce hydrogen up to 115.18 $\mu\text{mol h}^{-1} \text{ mg}^{-1}$, which is about 26 times as much high as CdS/g-C₃N₄ without Ni(OH)₂ (Fig. 12(c)). In this case, the Ni(OH)₂ can in situ precipitate on the CdS core, which can form intimate interface between CdS/g-C₃N₄ nanowires and Ni(OH)₂. As a result, it can enhance charge transfer capability. The significantly improved performance is probably ascribed to the two main factors: enhancing photogenerated electrons and holes transfer between the core and the shell, and inhibiting the recombination of charge carriers. Interestingly, they found the Ni(OH)₂ as electron donors is not a main reason to the improved photoactivity but it can provide abundant reaction sites.

Recently, Gu and co-workers [116] proposed a new thought for enhancing photocatalytic hydrogen evolution. They modified the g-C₃N₄ core@MoS₂ shell structure to obtain the new self-sensitized carbon nitride (SSCN) core by using triazine-based oligomer (TBO) dyes as sensitizer. After the SSCN-P@MoS₂ sample was treated by base Piranha solution to remove TBO, its H₂ production rate decreased from 0.91 $\mu\text{mol h}^{-1}$ to 0.24 $\mu\text{mol h}^{-1}$ (Fig. 12(d)). Of course, it is worth emphasizing that the comprehensive effect between MoS₂ coating and self-sensitization by TBO plays a major role in improving activity. Different from the effect of co-catalysts, the TBO dyes can enhance visible light absorption so that g-C₃N₄ obtains more electrons. When SSCN@MoS₂ is excited by visible light, the excited electrons of the carbon nitride core and surface TBO dyes jump to the nearby coated MoS₂ for H⁺ reduction. At the same time, TEOA in the solution could recover TBO dyes and consume the photogenerated holes. (Fig. 12(e)).

In addition, the H₂ production rate can be increased by constructing the typical type-II heterojunction, which enable the improvement of separation of photogenerated charge carriers, such as C-doped TiO₂@g-C₃N₄ core-shell hollow nanospheres [79] and hollow CdS@C₃N₄ spheres [102]. Among them, it should be point out that the hollow structure can improve photo quantum utilization because of multiple reflections of light and the reduction of redox potential. Besides typical type-II heterojunction, Z-scheme heterojunction by combining g-C₃N₄ shells with various core can also be used to improve photocatalytic activity, such as metal sulfide (CdS) [129], metal oxide (ZnO), or even oxygen defects-mediated metal oxide (OD-ZnO) [85]. In this system, the oxidation and reduction reactions are carried out in the semiconductor with more positive valence band and the semiconductor with more negative conduction band, respectively. Therefore, the core shell heterojunction with high redox potential can facilitate transfer and

separation of charge carriers, enabling the improvement of photocatalytic hydrogen evolution.

5.1.2. Photocatalytic degradation of pollutants

The atmospheric environment and water resources are polluted via rapid advancement of industrialization and urbanization, which are damaged for the natural environment and biological survival [143–147]. Thus, more effort needs to be paid to address pollutants in the air and water by developing different redox mechanisms [148–152]. Starting from the perspective of green and high efficiency, the utilization of photocatalysts is undoubtedly the promising way to mineralize pollutants [153,154]. Notably, photocatalysts with uniform component such as g-C₃N₄ have been certified to be unsatisfactory for degradation of dyes [155,156]. This is attributed to their low photo utilization and easy recombination of charge carriers, which hindered practical applications. For the problem, the exploration of high activity photocatalysts by constructing composites of different morphology such as nanowires [157], nanorods [158] and nanospheres [141] has been applied to improve the removal rate of pollutants. Given that the g-C₃N₄ nanosheets are soft polymer, it can form core shell structure by associating with other semiconductors or multifunctional substances. Obviously, the structure was applied for photocatalytic degradation of pollutants, which can get unexpected result due to adjustable core shape, their synthetic effect of the core and the shell and electronic structure adjustment. Herein, g-C₃N₄-based core shell structure photocatalysts for pollutant degradation were generally summarized in Table 4.

The methylene blue (MB) dye, which is widely accepted as the extensive material to verify the photodegradation effect, was used for evaluating the photoactivity of C₃N₄/BiPO₄ (CNBP), as reported by Pan and co-workers [131]. Under the UV light, the optimal CNBP in different thickness g-C₃N₄ shells can remove 90% of MB dye in 5 min, which is apparently superior to single component references (C₃N₄ and the uncoated BiPO₄). Especially for C₃N₄, it exhibited a negligible effect of degradation. The samples can be well reused due to stable protection of shells, which was proved by the experiments of cycles. Under visible light, the CNBP showed the different activity order, compared with that under UV light. The reason is that the main substance for excitation photocatalytic reaction is C₃N₄ instead of the uncoated BiPO₄. To the further verification of the degradation activity by pseudo-first-order kinetics, the highest rate constant k of CNBP reached up to 0.31 h^{-1} , which is 5 times higher than C₃N₄ (Fig. 13(a)). This is mainly attributed to the superiorities of core shell structures, including the reduction of electrons and holes recombination due to heterojunction interfaces and inhibition of polymerization of C₃N₄ nanosheets. The former can get more reactive oxygen species and holes and the latter can increase the surface area. Another reason for reducing recombination is energy level and lattice match in the core shell structure. Furthermore, the core shell structure can achieve transfer of charge carriers on individual BiPO₄ particle, resulting from charged surface domains generating strong dipolar fields, as certificated in additional examples (e.g. TiO₂/Ag and BiFeO₃/SrTiO₃).

The MB dye can also be degraded by the novel photocatalysts of ZnO@mesoporous g-C₃N₄ (mpg-C₃N₄), as shown by Chen et al. [109], who demonstrated the mpg-C₃N₄ possesses unique features, such as large surface area, open crystalline wall and porous surface. These features can be beneficial to the absorption of reactants, light harvesting and the electrons transfer. Whether under visible light or ultraviolet light, the composites have an optimal photodegradation activity. With the increase of the loading amount of mpg-C₃N₄, the activity of products presented an upward trend and then falling (Fig. 13(b)). The phenomenon may be attribute to the factor: despite the mpg-C₃N₄ can facilitate charge separation and transfer, it also can prevent the light absorption of ZnO core. Moreover, further analysis by HPLC chromatograms found the degradation process of both unloaded ZnO and ZnO@mpg-C₃N₄ is the same. Both of them degraded MB to

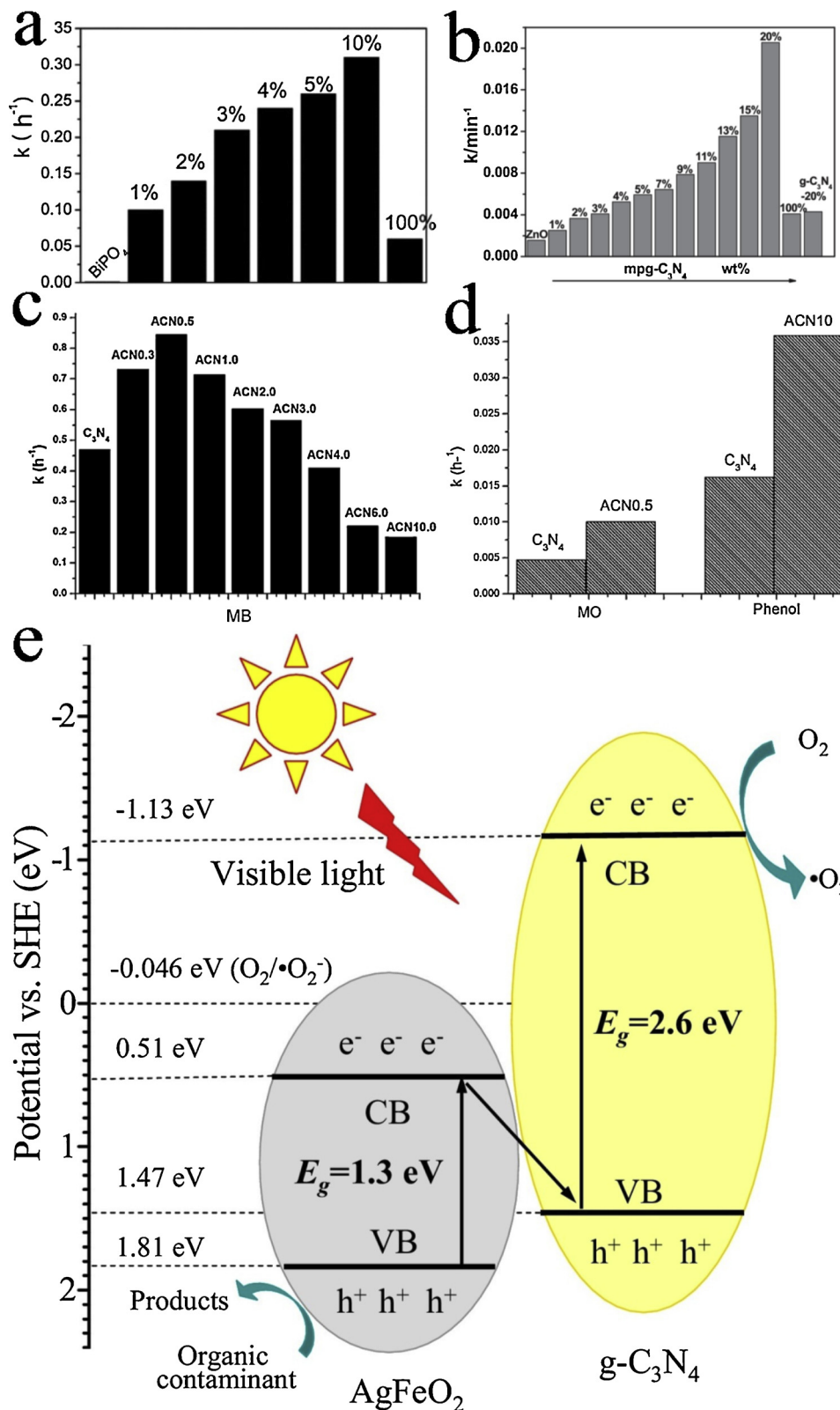
Table 4A summary of $\text{g-C}_3\text{N}_4$ -based core shell structure photocatalysts for pollutant degradation.

| Materials/($\text{g-C}_3\text{N}_4$ wt%) | Pollutant content/(mg L^{-1}) | Light source | Activity | Photoactivity enhancement | Ref. |
|---|--|---|---|---|-------|
| Pollutant: RhB^a | | | | | |
| BiOI@MIL-88A(Fe)@ $\text{g-C}_3\text{N}_4$ | 10 | 300 W Xe lamp $\lambda > 420 \text{ nm}$ | DE ^b of 75% in 180 min | – | [124] |
| TiO ₂ @ $\text{g-C}_3\text{N}_4$ hollow microspheres/(15%) | $1.0 \times 10^{-5} \text{ M}$ | 300 W Xe lamp $\lambda > 420 \text{ nm}$ | DE ^b of 93.3% in 100 min | > 3 times of TiO ₂ hollow microspheres | [117] |
| Rutile TiO ₂ @ $\text{g-C}_3\text{N}_4$ | 10 | 100 W Xe lamp $\lambda > 420 \text{ nm}$ | DE ^b of 95.68% in 180 min | > 1.8 times of $\text{g-C}_3\text{N}_4$; > 2 times of TiO ₂ | [120] |
| WO ₃ @ $\text{g-C}_3\text{N}_4$ /(1%) | 10 | A high-pressure xenon short arc lamp $\lambda > 420 \text{ nm}$ | DE ^b of 90% in 140 min | = 2.25 times of $\text{g-C}_3\text{N}_4$ nanosheets; = 4.5 times of WO ₃ | [159] |
| ZnO@ $\text{g-C}_3\text{N}_4$ nanoparticles | 5 | $\lambda > 400 \text{ nm}$ | $K^c = 0.0831 \text{ min}^{-1}$ | > 5 times of $\text{g-C}_3\text{N}_4$; > 3.4 times of ZnO | [133] |
| SiO ₂ / $\text{g-C}_3\text{N}_4$ core-shell nanospheres | 10 | 300 W Xe lamp $\lambda \geq 420 \text{ nm}$ | DE ^b of 94.3% in 150 min | \approx 3.5 times of $\text{g-C}_3\text{N}_4$ | [132] |
| Fe ₂ O ₃ / $\text{g-C}_3\text{N}_4$ | 10 | 300 W Xe lamp $\lambda \geq 420 \text{ nm}$ | DE ^b of 96.7% in 240 min | \approx 1.4 times of $\text{g-C}_3\text{N}_4$ | [160] |
| Bi ₂ WO ₆ @ $\text{g-C}_3\text{N}_4$ /(3%) | 10 | 250 W halide lamp $\lambda > 420 \text{ nm}$ | DE ^b of 90.8% in 30 min | \approx 1.97 times of Bi ₂ WO ₆ | [161] |
| α -S@ C_3N_4 /(35%) | 5 | 300 W Xe lamp $\lambda > 400 \text{ nm}$ | DE ^b of 93.4% in 40 min | \approx 3 times of α -S | [130] |
| Pollutant: TC^d | | | | | |
| Eu-CN ^e @BiVO ₄ | 20 | 300 W Xe lamp $\lambda > 420 \text{ nm}$ | DE ^b of 92.1% in 30 min | > 1.4 times of BiVO ₄ | [118] |
| β -Bi ₂ O ₃ @ $\text{g-C}_3\text{N}_4$ /(5%) | 10 | 250 W Xe lamp $\lambda > 420 \text{ nm}$ | DE ^b of 80.2% in 50 min | > 5.2 times of $\text{g-C}_3\text{N}_4$; > 1.4 times of β -Bi ₂ O ₃ | [162] |
| Compact and uniform TiO ₂ @ $\text{g-C}_3\text{N}_4$ | 20 | Xenon lamp with full spectrum | DR ^f of 2.2 mg/min | > 2.3 times of $\text{g-C}_3\text{N}_4$; > 2 times of TiO ₂ | [56] |
| Pollutant: CR^g | | | | | |
| Mesoporous TiO ₂ @ $\text{g-C}_3\text{N}_4$ hollow core@shell | 30 | 500 W Xe lamp equipped with a AM 1.5 cut-off filter | DE ^b of 97% in 120 min | > 5.1 times of HT ^h ; > 1.5 times of $\text{g-C}_3\text{N}_4$ | [80] |
| Pollutant: MOⁱ | | | | | |
| $\text{g-C}_3\text{N}_4$ /C, N co-doped anatase/rutile TiO ₂ | 10 | 300 W Xe lamp $\lambda > 420 \text{ nm}$ | DE ^b of 95% in 3.5 h | > 8.6 times of TiO ₂ ; > 4.4 times of $\text{g-C}_3\text{N}_4$ | [136] |
| SnO ₂ @ $\text{g-C}_3\text{N}_4$ microspheres | $1.0 \times 10^{-5} \text{ mol/L}$ | 500 W Xe lamp $\lambda > 400 \text{ nm}$ | $K^c = 0.013 \text{ min}^{-1}$ | > 1.6 times of $\text{g-C}_3\text{N}_4$ | [99] |
| Pollutant: MB^j | | | | | |
| $\text{g-C}_3\text{N}_4$ /MCNTs/BiOI | 10 | 300 W Xe lamp $\lambda > 420 \text{ nm}$ | $K^c = 0.364 \text{ h}^{-1}$ | > 1.3 times of BiOI; > 1.2 times of $\text{g-C}_3\text{N}_4$ | [101] |
| $\text{g-C}_3\text{N}_4$ /a-TiO ₂ /c-TiO ₂ | 10 μM | 100 W tungsten lamp $\lambda > 380 \text{ nm}$ | DE ^b of 82.2% in 60 min | > 9.1 times of $\text{g-C}_3\text{N}_4$ /c-TiO ₂ ; > 16.4 times of TiO ₂ | [163] |
| Ag ₃ PO ₄ @ $\text{g-C}_3\text{N}_4$ /(7%) | 10 | 250W halide lamp $\lambda > 420 \text{ nm}$ | DE ^b of 97% in 30 min | > 1.4 times of Ag ₃ PO ₄ | [128] |
| ZnO/g-C ₃ N ₄ nanorods | $1.0 \times 10^{-5} \text{ M}$ | 100 W halogen lamp $420 \text{ nm} < \lambda < 900 \text{ nm}$ | DE ^b of 98% in 60 min | > 6.5 times of ZnO; > 2.5 times of $\text{g-C}_3\text{N}_4$ | [137] |
| AgI@ $\text{g-C}_3\text{N}_4$ | 10 | 250W halide lamp $\lambda > 420 \text{ nm}$ | DE ^b of 96.5% in 120 min | > 1.3 times of AgI; > 3.1 times of $\text{g-C}_3\text{N}_4$ | [127] |
| C ₃ N ₄ /TiO ₂ | 0.03 mM | 500 W Xe lamp $\lambda > 420 \text{ nm}$ | – | = 1.3 times of TiO ₂ ; = 3.0 times of $\text{g-C}_3\text{N}_4$ | [164] |
| Ag@ C_3N_4 | 0.01 mM | 500 W Xe lamp $\lambda > 420 \text{ nm}$ | – | = 1.3 times of TiO ₂ ; = 1.8 times of $\text{g-C}_3\text{N}_4$ | [164] |
| ZnO/mpg-C ₃ N ₄ ^k | 0.01 mM | 500 W Xe lamp $\lambda > 420 \text{ nm}$ | $K^c = 0.135 \text{ min}^{-1}$ | > 1.9 times of ZnO | [109] |
| C ₃ N ₄ /BiPO ₄ /(4%) | $1.0 \times 10^{-5} \text{ mol L}^{-1}$ | 11 W low-pressure lamp at 254 nm | – | \approx 4.5 times of P25 (TiO ₂); \approx 3.5 times of BiPO ₄ | [131] |
| Pollutant: phenol | | | | | |
| g-C ₃ N ₄ @TiO ₂ | 10 | 500 W Xe lamp $\lambda > 420 \text{ nm}$ | – | > 7.2 times of $\text{g-C}_3\text{N}_4$ | [121] |
| Mesoporous TiO ₂ /g-C ₃ N ₄ Microspheres | 10 | 500 W Hg (Xe) globe $\lambda < 420 \text{ nm}$ | $K^c = 6.8 \times 10^{-3} \text{ min}^{-1}$ | > 8.5 times of $\text{g-C}_3\text{N}_4$ | [83] |
| Pollutant: AB92^l | | | | | |
| Ag ₃ PO ₄ /BiPO ₄ @MIL-88B(Fe)@ $\text{g-C}_3\text{N}_4$ | 10 | 300 W Xe lamp $\lambda > 420 \text{ nm}$ | DE ^b of 85% in 60 min | > 5.6 times of MIL-88B(Fe); = 3.4 times of $\text{g-C}_3\text{N}_4$ | [123] |
| Pollutant: 4-CP^m | | | | | |
| g-C ₃ N ₄ /OD-ZnO ⁿ nanorods | $1.0 \times 10^{-4} \text{ mol L}^{-1}$ | 300 W Xe lamp $\lambda > 420 \text{ nm}$ | DE ^b of 95% in 60 min | > 1.4 times of OD-ZnO ⁿ ; > 2.7 times of $\text{g-C}_3\text{N}_4$ | [85] |
| Pollutant: ARG | | | | | |
| AgFeO ₂ /g-C ₃ N ₄ /(20%) | 20 | 300W Dy lamp $\lambda > 400 \text{ nm}$ | DE ^b of 94% in 180 min | > 11.7 times of AgFeO ₂ ; > 8.5 times of $\text{g-C}_3\text{N}_4$ | [165] |

^aRhB: Rhodamine B; ^bDE: degradation efficiencies; ^cK: rate constant; ^dTC: tetracycline; ^eEu-CN: Eu doped $\text{g-C}_3\text{N}_4$; ^fDR: degradation rate; ^gCR: congo red; ^hHT: TiO₂ hollow nanospheres; ⁱMO: methyl orange; ^jMB: Methyl blue; ^kmpg-C₃N₄: mesoporous C₃N₄; ^lAB92: Acid Blue 92; ^m4-CP: 4-chlorophenol; ⁿOD-ZnO: oxygen-defective ZnO.

intermediate products first, followed by mineralizing into CO₂ and H₂O [166,167]. In addition, compared with ZnO, the composites showed stronger absorption capacity in view of these facts that mpg-C₃N₄ can form the π - π stacking with MB and expand BET surface area of ZnO [168].

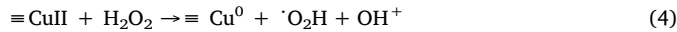
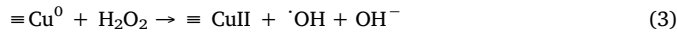
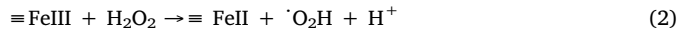
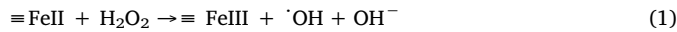
Noble metal (Ag) can also be applied for enhancing the photocatalytic degradation of MB. Ag@C₃N₄ core shell nanocomposites was synthesized by Bai and co-workers [141], which exhibited higher photocatalytic ability than pure g-C₃N₄. Moreover, the increased photocatalytic performance of as-prepared samples can be further



demonstrated by other pollutants, such as methyl orange (MO) and phenol (Fig. 13(c), (d)). The authors attributed this phenomenon to the main reasons: (I) The introduction of Ag nanoparticles can produce more holes as the main oxidative species, which can be certified by the trapping experiments; (II) Owing to maximized connection between $g\text{-C}_3\text{N}_4$ nanosheets and Ag core, Ag nanoparticles can speed up the charge transfer rate confirmed by electrochemical impedance spectroscopy

(EIS); (III) Ag core as a reservoir of electrons can promote the separation of photogenerated carriers; (IV) the improvement of intensity of light absorption is due to the localized surface plasmon resonance (LSPR) of noble metal Ag. More importantly, Ag cores can avoid dissolution and corrosion under the protection of $g\text{-C}_3\text{N}_4$ shells. For this reason, the core shell structure can introduce more materials to synthesize photocatalysts. Apart from noble metal, magnetic Fenton-like

catalysts have been applied for decolorization of pollutants [169,170]. For instance, Yao et al. [104] reported the novel as-fabricated Cu-Fe₂O₄@C₃N₄ catalysts, which combined Fenton-like function and photocatalysis to degrade Orange II. Compared to g-C₃N₄ with quite low removal rate of Orange II, under the visible light irradiation, the presence of vintage sample (CuFe₂O₄@C₃N₄ (2:1)) can degrade around 98% of Orange II within 3.5 h. Accordingly, the heterointerfaces of core shell structure can excellently enhance the photocatalytic performance [171]. The orange of dye disappears, which can be ascribed to the destruction of chromophoric structure by the analysis of UV-vis spectral. Actually, the certain factors play a main role in influencing the photocatalytic activity in wastewater, as follows: (I) The initial concentration of dye can decrease the utilization of light and removal efficiency; (II) With the proper increase of reaction temperature, the reactant can get more energy. More importantly, it can obtain more hydroxyl radicals by the improvement of the decomposition of H₂O₂ in Fenton-like system [172]; (III) The introduction of different anions can change the pH values in solution and increase the removal rate of dye because of the production of novel radicals in the photo Fenton-like system [173,174]. The introduction of NaCl or NaHCO₃ can favor the faster and better removal of Orange II in the composite system of H₂O₂ and CuFe₂O₄@C₃N₄. What's more, for wastewater treatment, the hybrid possessed unique advantages that its magnetic properties are easy to recycle as well as its Fenton-like effect are facilitate to degrade organic compounds [175,176]. H₂O₂ can be reduced to hydroxyl radicals by the catalysis of Cu⁰ or FeII, which occurred on the surface of CuFe₂O₄ crystal, and then CuII or FeIII may react with H₂O₂ to produce ·O₂H. The specific reaction formulas are explained (Eqs. (1) – (4)):



Besides the regulation of chemical properties, adjustment of physical properties is also an excellent measure for achieving the application of high activity photocatalysts. Wang and co-workers [56] announced that TiO₂@g-C₃N₄(TCN) quantum heterojunction was able to remove tetracycline. Because (TiO₂) cores with exposed (001) facets and quantum-thick g-C₃N₄ shells can be combined tightly and evenly, the degradation rate of 100 mg of TCN can reach up to 2.2 mg per minute, which is 1.36 times higher than that of the random mixture of TiO₂ and g-C₃N₄ (TCNmix) and 130% higher than that of g-C₃N₄. Hence, the physical properties of g-C₃N₄ CSNs, such as exposed facets, shell thickness, and the connection of interface, have served as vital factors to degrade pollutants.

Apart from the application in water, several g-C₃N₄ CSNs can simultaneously treat organic pollutants in water and air. Tang et al. [165] found that Ag-based materials with delafossite structure (AgFeO₂) as core can display promising photocatalytic ability for the degradation of acid red G (ARG) (94%) and gaseous formaldehyde (about 87% within 9 h). Generally, it is well known that the key elements for high efficiency photocatalysis are made up of separation efficiency of charge carriers [177], photo absorption property [178] and specific surface area [179]. Nevertheless, it is found that the absorption amount of AgFeO₂/g-C₃N₄ composites for ARG has rarely changed with the weight ratio of g-C₃N₄ shells from 10% to 40%. Hence, they excluded the specific surface area as the main factor for enhancing photocatalytic performance. By further analysis of photoluminescence (PL) spectra, the samples exhibited excellent charge separation as compared to pure g-C₃N₄ and AgFeO₂. The composites with a Z-scheme heterojunction system was confirmed, which is based that the g-C₃N₄ shells possess a more negative CB and more positive VB as compared to AgFeO₂ cores, and the photo-excited electrons on the CB of AgFeO₂ cores are lack of reducing ability to obtain superoxide by reducing O₂ in air. Detailed

energy band structure image is shown in Fig. 13(e).

In conclusion, the g-C₃N₄ based core shell structure can enhance photocatalytic activity by matching multifunctional cores (like noble metal, photosensitizer, electronic capture substances, special exposed surface, oxygen defects, magnetic and Fenton-like materials), introducing cocatalysts and photosensitive dyes, and constructing hollow structures, Z-scheme heterojunctions, and mesoporous structures. No matter what measures to synthesize g-C₃N₄ CSNs, their purposes are to make up for the drawbacks of g-C₃N₄, including low specific surface area for material adsorption, facile recombination of photo-excited electrons and holes, and limited light absorption. The discrepancies in added materials and preparation process exhibited different photocatalytic activities, which emphasizes the influence of varying parameters, such as initial concentration of pollutants, PH, temperature, dosing amount, reaction time, and the presence of other ions. The comprehensive effects of core shell structure related to g-C₃N₄ greatly attracted the attention of researchers in the field of photocatalysis as a result of its easy combination and protection. The further exploration in this direction is worthy of our more efforts.

5.1.3. Other photocatalytic applications

The developments of g-C₃N₄ CSNs have led to new trends of their use in other photocatalysis fields, such as CO₂ reduction and nicotinamide adenine dinucleotide (NADH) regeneration. The utilization of hydrocarbon fuels mainly causes increased levels of atmospheric CO₂ [180]. The increased CO₂ concentration is responsible for the rise of global temperature. This rise could result in melting of the ice caps, the conversion of arable land to desert, and the subsequent a rise in sea level and loss of habitat [181–183]. Therefore, the reduction of CO₂ to fuel by photocatalysts can provide a feasible solution to maintain the sustainability of oil reserves and ameliorate associated climate change. However, the photocatalytic materials offer limited visible absorption and the short lifetime of charge separation. Therefore, researchers have been seeking suitable photosensitizer to attach known photocatalysts and matched semiconductor to extend charge life. Graphitic carbon nitride, as a narrow bandgap semiconductor, can provide better sensitivity and form heterojunctions with other semiconductors to extend charge life. Therefore, g-C₃N₄ CSNs are extraordinarily applied for performing CO₂ reduction. As an example, Li et al. [86] synthesized core shell LaPO₄/g-C₃N₄ nanowires for photoreduction of CO₂. This kind of nanocomposites can largely overcome the drawbacks of the corresponding individual LaPO₄, which include poor sensitivity and wide bandgap, and show effective separation/transfer because of the synergistic catalytic effect between the components. The test results of the product show that CO and O₂ were found. Therefore, the process of CO₂ reduction is explained (Eqs. (5) and (6)):



The CO yield over the optimum sample reaches 14.4 $\mu\text{mol g}^{-1} \text{h}^{-1}$ in the first hour, which is around 8.07 and 10.36 times that of tubular g-C₃N₄ and LaPO₄.

NADH, as one of the largest classes of enzymes (oxidoreductases), has increasingly gained attention due to its essential practical applications in many energy-relevant catalytic hydrogenation reactions spanning from hydrogen production, oxygen reduction to alcohol deactivation [184]. Given the physical instability, stoichiometric usage, necessity and expensiveness of NADH, effective and facile preparation processes are required for practical applications [185,186]. Currently, g-C₃N₄ CSNs have succeed in achieve NADH regeneration. For instance, Wu et al. [84] prepared g-C₃N₄@α-Fe₂O₃/C core@shell photocatalysts for highly efficient regeneration of NADH. In this system, [Cp*Rh(ppy)H₂O]²⁺, a rhodium complex, was used as a mediator to transfer hydrogen and electrons to NAD⁺ (Fig. 14(a)). TEOA was utilized as a sacrificial to remove holes. NADH, as one essential hydride donor, was

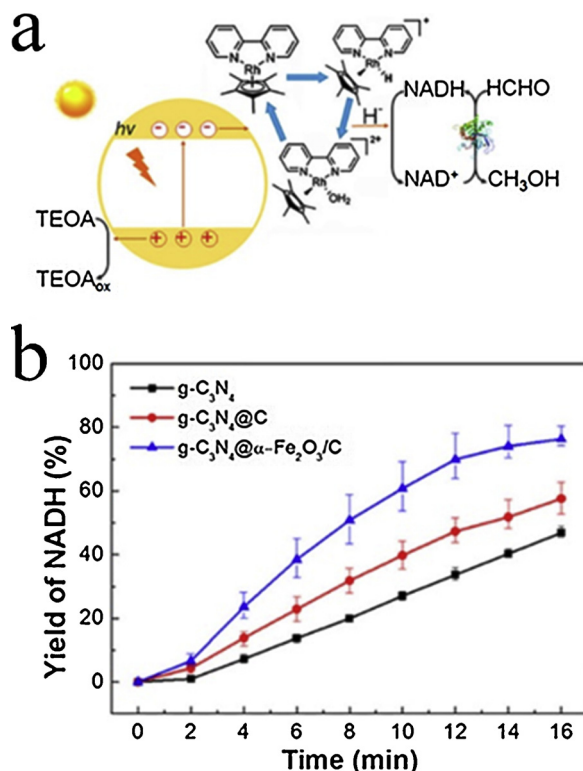


Fig. 14. (a) Schematic diagram of the coupling system with photocatalytic NADH regeneration and enzymatic reduction of formaldehyde. (b) Time-resolved NADH regeneration yields of $g\text{-C}_3\text{N}_4$, $g\text{-C}_3\text{N}_4\text{@C}$ and $g\text{-C}_3\text{N}_4\text{@}\alpha\text{-Fe}_2\text{O}_3\text{/C}$. Reproduced with permission from ref [84]. Copyright 2018 American Chemical Society.

used for reduction of formaldehyde to methanol. In the photocatalytic NADH regeneration known at the time, $g\text{-C}_3\text{N}_4\text{@}\alpha\text{-Fe}_2\text{O}_3\text{/C}$ reached the highest an initial reaction rate (r) of $7.7\text{ mmol h}^{-1}\text{ g}^{-1}$ (based on the first 6 min) (Fig. 14(b)).

5.2. Photoelectrocatalytic applications

At present, photoelectrocatalysis (PEC) system is an advanced system to achieve redox function by utilizing solar energy. The typical system is an electrical circuit, which is composed of external circuit, working electrode, counter electrode, and electrolyte [187]. What is more, in a three-electrode PEC system, this needs to add a reference electrode for offering a steady potential reference to measure the voltage of other electrodes [188]. Generally speaking, the composition of counter electrode is very common, such as carbon materials and noble metal. Consequently, it is the key of photoelectrochemistry that developing new semiconductors applies to the working electrode. Commonly, semiconductor-based photoanode for achieving efficient PEC application is closely related to these essential demands: stability in solution, suitable band gap and margin for both ample light absorption and the powerful ability of reduction and oxidation, long charge life and low recombination of carriers to make carriers reach the semiconductor-electrolyte interface as much as possible [87,189]. Fortunately, the current trend in the investigation of $g\text{-C}_3\text{N}_4$ CSNs could meet the demands of PEC development described above. In this part, we will summarize the progress of $g\text{-C}_3\text{N}_4$ CSNs as the working electrode for PEC applications (including PEC water splitting and water purification).

For the PEC water splitting, Yi and co-workers [87] synthesized the Ti-doped $\text{Fe}_2\text{O}_3\text{@}\text{g-C}_3\text{N}_4$ core shell heterojunction loaded by carbon quantum dots (denoted as $\text{Ti:Fe}_2\text{O}_3\text{@GCNN-CQDs}$). In comparison to lately reported promising photoanodes, the as-fabricated sample

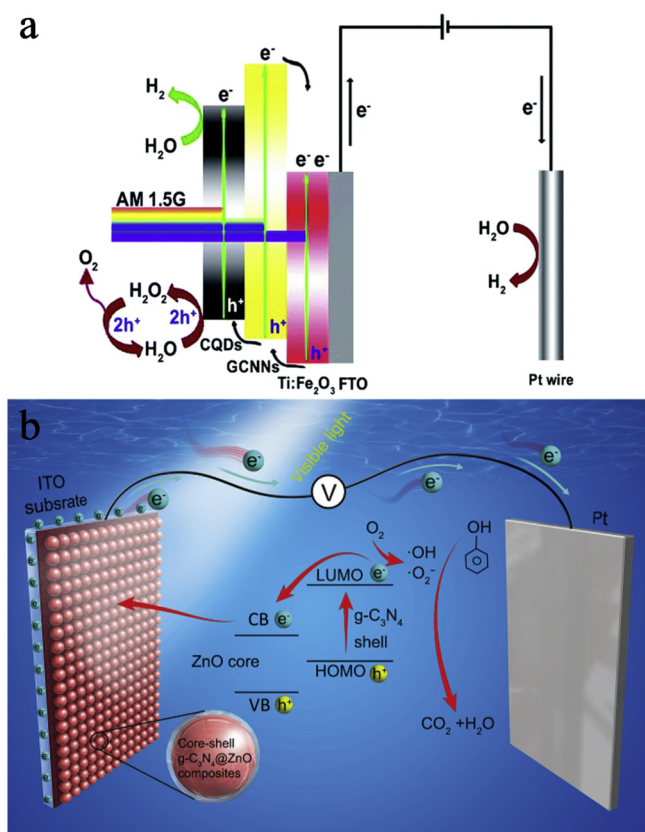


Fig. 15. (a) Schematic diagram of reaction mechanism and band structure for $\text{Ti:Fe}_2\text{O}_3\text{@GCNN}$ core-shell heterostructure. Reproduced with permission from ref [87]. Copyright 2018 The Royal Society of Chemistry. (b) Schematic diagram of reaction mechanism and band structure for 15% $g\text{-C}_3\text{N}_4\text{@ZnO}$ composites. Reproduced with permission from ref [199]. Copyright 2017 Elsevier.

exhibited up to 3.38 mA cm^{-2} of photocurrent density at 1.23 V versus a V_{RHE} , which is 2 times as high as that of $\text{Ti:Fe}_2\text{O}_3$. This indicates that the as-prepared compound facilitates charge separation and transport as well as are comparable to the reported excellent activity of hematite. Subsequently, they analyzed the role of each component and integrated effect. First of all, the role of Ti doping is reflected in regulating band-bending for facilitating charge carriers separation because of the anodic-shifted flat band potential [190]. As a result, the photocurrent density significantly improved. Afterwards, CQDs and GCNNs can speed up charge separation, leading to photocurrent density increase. Meanwhile, although their separate loading can increase donor density of $\text{Ti:Fe}_2\text{O}_3$ slightly, the coupling of them can show a dramatic improvement of donor density and decrease the charge transfer resistance. These further prove that the CQDs and GCNNs possess favorable charge separation and transfer behavior, resulting in suppressing the recombination of bulk/surface [191]. Finally, the loading of CQDs not only completes the kinetics of $\text{Ti:Fe}_2\text{O}_3\text{@GCNN}$ core shell structure for water oxidation but can also be used as the sensitizer for oxidation of hydrogen peroxide, which is a transition product in PEC water oxidation. As illustrated in Fig. 15(a), the energy structure of well-designed core shell structure showed photo-excited holes transfer from $\text{Ti:Fe}_2\text{O}_3$ cores to GCNNs shells then to CQDs and photo-generated electrons reach the counter electrode in the opposite direction. Thus, the improvement of PEC water splitting and efficient charge separation are mainly because the delicate and integrated core shell structure, which is taking $g\text{-C}_3\text{N}_4$ as an intermediary.

To further enhance the performance of photoanode, several quality materials have been investigated. Starting from the utilization of TiO_2 as the electrode to decompose water [192], TiO_2 as an outstanding candidate of photoanode gets an in-depth study. In spite of its

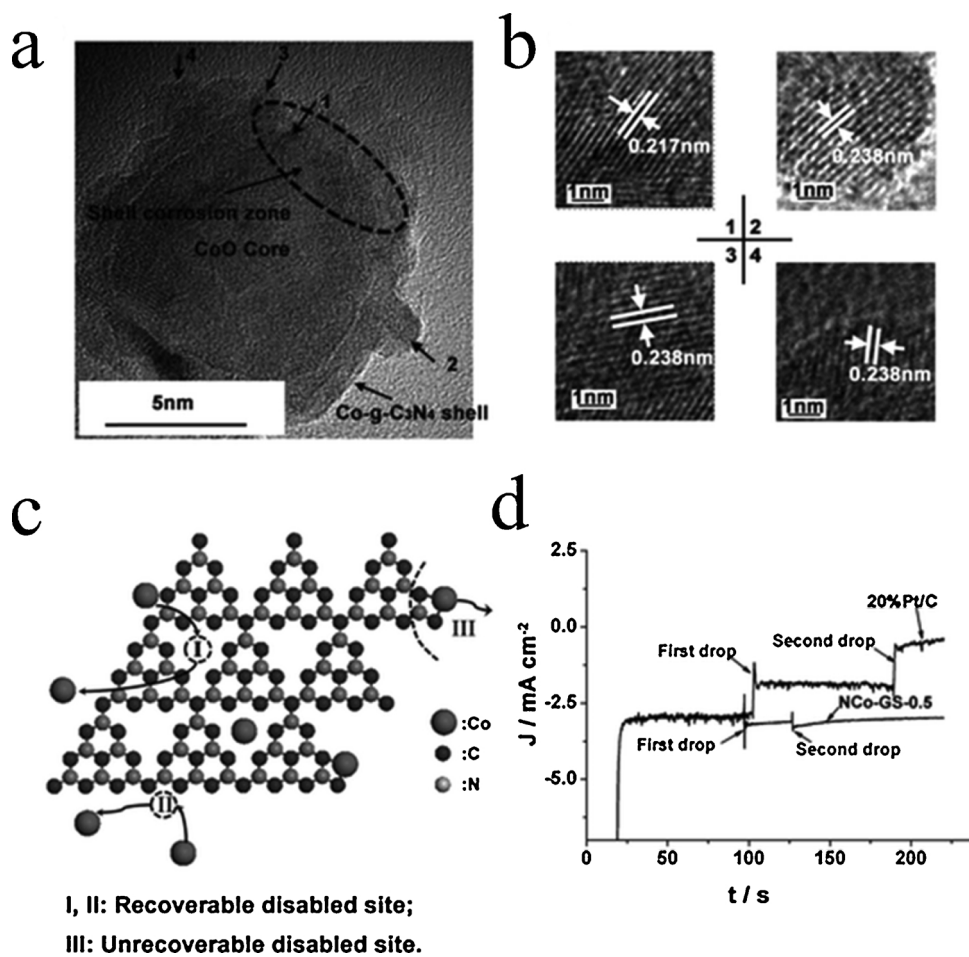


Fig. 16. Stability evaluation of the hybrid for ORR. TEM (a) and HRTEM (b) images of NCo-GS-0.5 after one day of accelerated degradation test (ADT); (c) Schematic diagram of degradation mechanism for NCo-GS-0.5; (d) Comparative experiment on the influence of methanol for NCo-GS-0.5 hybrid and 20% Pt-C. Reproduced with permission from ref [115]. Copyright 2013 The Royal Society of Chemistry.

nontoxicity [193,194] and excellently photoelectrochemical properties [195], it can only be excited under UV light but not in the visible light due to its wide band gap (3.2 eV). Besides, $\text{g-C}_3\text{N}_4$ has suitable band gap (2.7 eV) for capturing visible light, but it is provided with a typical drawback that easy compound of charge carriers. Consequently, Fan et al. [196] thought of using TiO_2 and $\text{g-C}_3\text{N}_4$ to build a core shell heterojunction for solving their shortcoming. By the work, they found the $\text{TiO}_2@\text{g-C}_3\text{N}_4$ core shell photoanode yields the photocurrent density of $80.9 \mu\text{A cm}^{-2}$ at 0.6 V (vs SCE) under visible light, which is 21 times higher than that of $\text{g-C}_3\text{N}_4$. This composite has several highlights that rod-shaped TiO_2 cores provide short-range electronic transmission path and a large surface area, avoid $\text{g-C}_3\text{N}_4$ stacking into large particles, and uniformly load carbon nitride, as well as the space between nanorods and bulk effect with high orientation are suppressed because of the core shell structure.

For degradation of pollutants, the comprehensive utilization of both electrolysis (EC) and photocatalysis (PC) have a better effect than the use of individuals [197]. Sometimes, the PEC process for removing pollutants could be superior to the separate addition of EC and PC processes [198]. Similarly, the composite core shell materials based on $\text{g-C}_3\text{N}_4$ as the working electrode will become a new direction for water purification. For instance, Wang and co-workers [199] fabricated $\text{g-C}_3\text{N}_4@\text{ZnO}$ core shell photoanodes. In this work, they added the external potential bias to greatly enhance the electronic transfer and inhibit the recombination of charge carriers. Hence, it can effectively degrade phenol, which can be demonstrated by comparing pseudo-first order kinetic between different processes. Taking the 15% $\text{g-C}_3\text{N}_4@\text{ZnO}$

with optimum performance as an example, its k value is 1.216 h^{-1} during the PEC degradation of phenol under visible light, which is around 7 times and 3 times as high as that of EC and PC degradation, respectively. This indicated that the $\text{g-C}_3\text{N}_4$ shell with the appropriate thickness and the applied bias, which will provide an effective driving force, are helpful for the separation of electron-hole pairs generated by photoelectricity. However, the loading of $\text{g-C}_3\text{N}_4$ shell decreased PC and PEC activity of pure ZnO under UV light due to the factor that $\text{g-C}_3\text{N}_4$ hindered the UV light absorption of ZnO core. Further, the author found the PEC performance of samples was affected by the thickness of $\text{g-C}_3\text{N}_4$ and the optimum thickness is 1.91 nm. For the phenomenon, they summarize the following two points. First, when continuously increasing $\text{g-C}_3\text{N}_4$ amount, interfacial transfer and the separation of photo-excited electrons and holes were enhanced by the synergistic influence from polarization field offered by ZnO and increasing visible-light absorption by the $\text{g-C}_3\text{N}_4$. Second, when the load exceeds a certain limit, the formed over-density samples will increase the distance of charge transfer and obstruct the movement of electrons from ZnO cores to counter electrode. The specific degradation mechanism is shown in Fig. 15(b). Under visible light irradiation, the $\text{g-C}_3\text{N}_4$ shell is excited, followed by a $\pi-\pi^*$ transition occurs, causing the excited state electrons to migrate from the highest occupied molecular orbital (HOMO, 1.57 eV) to the lowest unoccupied molecular orbital (LUMO, 1.12 eV). Since the VB potential of $\text{g-C}_3\text{N}_4$ (1.40 eV) is lower than that of $\text{H}_2\text{O}^-/\text{OH}^-$ and OH^-/OH (2.27 eV and 1.99 eV) CB potential, $\cdot\text{OH}$ cannot be formed by hole oxidation. At the same time, LUMO of $\text{g-C}_3\text{N}_4$ is less than the CB edge of zinc oxide (-0.5 eV). The excited electrons on the

LUMO of g-C₃N₄ can be transferred from the working electrode to the counter electrode in sequence. In a word, the improvement of phenol degradation performance under visible light is mainly because of electro-oxidation assisted photocatalysis and special core-shell nanostructures.

5.3. Electrocatalytic applications

The g-C₃N₄ based core shell structure can be used in the field of fuel cells, which can directly convert the chemical energy of fuel into electrical energy. In the process, the fuel has undergone an oxidation reaction and produced electrons, which will transfer from the anode to the cathode. On the other hand, oxygen reduction reaction (ORR) has taken place in the cathode. Whereas, the latter reaction is slower than the former, reducing overall efficiency, so electrocatalysts are needed to increase cell efficiency. Traditional platinum electrocatalysts are indeed superior to other electrocatalysts, but it is rare and expensive. Although the electrocatalytic performance of carbon nitride itself is not strong, it can be combined with other substances to obtain good and low-cost electrocatalysts. In particular, this core-shell structure has received extensive attention [91,200–202]. For instance, Jin et al. [115] incorporated the stable and highly active electrocatalyst based on g-C₃N₄@CoO nanoparticles supported on graphene into fuel cells (Fig. 16(a), (b)). By the contrast experiments, the cathodic peak potential was enhanced from -0.27 V to -0.21 V compared with graphene-supported CoO without g-C₃N₄ and the kinetic-limiting current density ($J_{k\text{c}}$) reached 16.78 mA cm⁻² which was close to that of 20% Pt-C (17.22 mA cm⁻²) in the identical situation. In the range of potential from -0.25 V to -0.6 V, parameter n, the electron transfer number, is close to 4, meaning that O₂ is directly oxidized to ·OH. In addition, the gap, between the composite and 20% Pt-C, of half-wave potential ($\Delta E_{1/2}$) has been reduced to only 25 mA. The above facts indicate that the composite has excellent catalytic activity, which exceeds many other catalysts of the same type. Further experiments and analysis revealed that the active sites are mainly cobalt-doped g-C₃N₄ shell. The process, a one-electron and quasi-reversible reduction, determines the ORR reaction rate, which may involve both charge transfer and the reaction intermediate migration. For transition metal-based electrocatalysts, this is usually considered the intermediate O₂²⁻ intermediate formation by a two-electron reduction and the movement of O₂/OH⁻ are the main step to suppress the ORR rate in alkaline solution, which is likely to apply to the hybrid. From the author's research, this resulting hybrid shows the following advantages: (I) forming a large number of active sites, which can be attributed to the factor that pyridine nitrogen in g-C₃N₄ shells coordinate with cobalt ions to form Co-N_x species (Fig. 16(c)); (II) obtaining higher stability in alkaline solution compared to 20% Pt-C, which may originate from broken active sites that can be supplemented by a slow release of CoO cores; (III) exhibiting remarkable poison resistance (Fig. 16(d)). In addition to the cathodic catalyst, it can be used for the anodic catalyst. The platinum and ruthenium bimetallic catalyst (PtRu) has always been a representative of high efficiency anodic electrocatalysts. However, high price and scarcity limited their promotion. Consequently, developing a carrier to evenly disperse PtRu nanoparticles is a critical step. Li and his colleagues [58] replaced the C support with a novel C@g-C₃N₄ nanosheet (C@g-C₃N₄ NS) support to obtain anodic catalyst in direct methanol fuel cells (DMFCs). Through methanol electro-oxidation test, they were surprised to find that the samples (PtRu/C@g-C₃N₄ NS) increased the catalytic activity by a factor of 2.1 relative to PtRu/C. This is mainly because g-C₃N₄ nanosheets with Lewis acid and base sites can prevent PtRu particles aggregation resulting in uniform PtRu NPs particles distribution. The PtRu/C@g-C₃N₄ NS catalyst possesses stability and outstanding mechanical resistance in oxidative and acidic surrounding, and the construction of core shell structure enhanced electron conductivity of the support. Furthermore, the stability of PtRu /C@g-C₃N₄ NS catalyst is improved by 14% and its poison tolerance is stronger, compared with

the as-prepared PtRu/C, which was confirmed by the accelerated potential cycling tests (APCTs) and comes from the metal–support interaction (SMSI) between C@g-C₃N₄ NS support and PtRu NPs.

With the replacement of fuel cells (FCs), new FCs are slowly emerging, such as alkaline FCs [203,204], proton exchange membrane FCs [205], microbial FCs [206], and molten carbonate FCs [207], etc. However, they still face the same problem of low ORR kinetics. To achieve a wider application of FCs, we must explore new stable, low-cost, and efficient Pt-free ECs to replace expensive Pt-based electrodes. Later, different from the support decorated above, the core shell g-C₃N₄ nanoshells can directly serve as ECs at fuel cells, compared with conventional and noble Pt-C, which can combine multiple metal atoms, thus enhancing the practicality. Recently, Negro and co-workers [114] incorporated new core shell Pt-free g-C₃N₄ based ECs into anion-exchange membrane fuel cells (AEMFCs) for ORR. The innovative ECs are composed of CN embedded with iron-tin alloy as shells and graphene nanoplatelet (GNP) as cores. Even in the absence of PGM, the as-prepared samples exhibited a low overpotential, which was an increase of about 70 mV compared to Pt/C ECs. The CN shells could combine with metals to form coordination bonds, thus improving the stability of the metal. Besides, the core shell ECs showed a rare microporosity, which can contribute transport of products and reactants and reduce the concentration overpotentials. It possesses high resistance to methanol poisoning and works well in a gas-diffusion circumstance. Nevertheless, it still faces a mass and charge transfer problem because of a non-optimized porosity [208]. At present, there are several improvement measures, including regulating synthetic ratio between N species and active metal atoms and increasing the surface amount of metal clusters embedded in CN [113].

6. Conclusions and perspectives

In conclusion, g-C₃N₄ CSNs have made considerable progress in construction and applications. In the future, the development of g-C₃N₄ CSNs will grow exponentially and achieve in other fields. Herein, the latest research progress on the g-C₃N₄ CSNs have been summarized. The advantages of core shell structure and g-C₃N₄ CSNs are emphasized for showing their unique features. The design of g-C₃N₄ CSNs are introduced for providing guideline to synthesize g-C₃N₄ CSNs in the future. The construction methods for g-C₃N₄ CSNs broadly categorized into three groups including hydro/solvothermal methods, ultrasonication-assisted self-assembly strategies, and heat treatment. The g-C₃N₄ CSNs have diffuse applications in catalysis including photocatalytic hydrogen evolution and degradation of pollutants, photoanodes, and electrocatalysts. In this part, the current difficulties in each application, and how structural construction of g-C₃N₄ CSNs breaks through them, are summarized.

Despite great progress having been achieved in g-C₃N₄ CSNs, this field is also faced with many challenges. First, a large-scale, general, and simple construction method eagerly needs to be developed for adapting to various cores with different surface properties, morphology, and composition. Second, the specific growth mechanism of g-C₃N₄ shells under different construction methods and core materials is one of the challenges. Third, the construction method needs further exploration to effectively establish controllable synthesis of g-C₃N₄ shells with desired thickness, tightness, surface chemistry, porosity and more, which are hoped to meet actual demands of the catalytic field. Finally, g-C₃N₄ nanosheets, as the traditional layered 2D materials, consist of a covalently bonded lattice and are feasible to be stripped through the top-down exfoliation method due to the weak van der Waals force between neighboring layers. However, the existent preparation methods, such as wet-chemical method and ultrasonic method, have not ideal for the construction of ultrathin structure with atomic thickness. Therefore, the facile and efficient construction of high-quality g-C₃N₄ nanosheets with atomic thickness is still lacking in the catalytic field.

To really apply it to reality, the design of the g-C₃N₄ CSNs in the

future should move toward trend of stableness, cheapness, possessing adjustable morphology and functional materials (cocatalysts, photosensitizer, and metal atoms), and simple synthesis method.

The construction of g-C₃N₄ CSNs has empowered g-C₃N₄ with novel chemical, electrical, optical, and mechanical properties. These progresses have in turn made a breakthrough in catalytic field. However, from the construction perspective, there are still some considerations that should be proposed. Despite the facile and easy-to-operate hydro/solvothermal methods has been developed, it has few adjustable parameters so that the formation of products tends to be randomly combined. Due to the simplicity, effectiveness, and extensiveness of hydro/solvothermal methods, it has indeed been tried to synthesize a variety of g-C₃N₄ CSNs. In this process, in order to avoid blindly trying, the specific combination mechanism and formation principle are urgently needed to be confirmed. Self-assembly strategies rely on solution evaporation, van der Waals forces, electrostatic forces or reflux. This synthetic method suffers from several inherent deficiencies, which range from the lack of core-shell combination robustness without high temperature treatment to unsatisfactory efficiency and yield from multistep synthetic process. Herein, exploring a method with both energy savings and a tight interface has provoked interest of researchers. For the heat treatment, calcination is limited in the use of materials due to the high temperature. Therefore, the method is also mainly directed to high temperature resistant oxides. Moreover, the annealing temperature is a key factor for the synthesis of g-C₃N₄ CSNs. However, lacking in-depth research in inherent mechanisms about the construction of core-shell structures with precursors of different states (gaseous, liquid, and solid) is not conducive to deep understanding of experimental results. Therefore, developing high-end experimental measurements and rigorous theoretical calculations for revealing the mask of g-C₃N₄ CSNs at charge carriers' properties and molecular level is imperative. Other than that, individual examples apply other methods, such as pulsed laser deposition, a facile ball milling method, and gas-phase and wet-chemical synthesis techniques. Indeed, the development of this new idea is worth encouraging. However, it could find that the methods of producing high-quality g-C₃N₄ CSNs is still very rare by searching the literature, and even if the emergence of new methods, they have significant limitations.

From the structure and performance point of view, the following suggestions are worth looking forward to. Synthetic shape of g-C₃N₄ CSNs is mainly limited with spherical structure because of the natural advantages of core symmetrical adhesion. The increasing demands on other catalytic fields make various shape of g-C₃N₄ CSNs become more practical. For instance, rod-shaped g-C₃N₄ CSNs electrodes are more suitable for charge transport than spheres. In general, the shell coating of aspheric core is not uniform, but these also endows g-C₃N₄ CSNs with new properties that allow them to a wider range of applications and are of academic interest. The stability and activity of g-C₃N₄ CSNs are negatively correlated to some extent because shell porosity determines the accessibility of corrosive materials and light sources. The synthesis of g-C₃N₄ precursor directly affects the sealing degree of the g-C₃N₄ shell. In order to conveniently adjust the porosity of the shell, developing shell etching methods is promising.

From the application perspective, most of the retrieved papers indicate that there are wide applications in the field of catalysis and rare scope in biomedical applications, inhibition of bacteria and degradation of nitrogen oxides. At present, these fields are worth exploring. For example, the combination of MOF and g-C₃N₄ photosensitizers constructs core-shell structures for chemical and photodynamic therapy [209]. In view of MOF materials with the wide range of applications in bioimaging, separation, sensors, and gas storage, it is expected that there are new applications of g-C₃N₄ CSNs towards these areas. For the field of sensors, N-doped CsTi₂NbO₇@g-C₃N₄ core-shell heterostructures have been synthesized for nitrite detection [210], which means that there are many untapped applications for g-C₃N₄ CSNs. It is hoped that g-C₃N₄ CSNs play some small part in energy conversion and

storage devices, such as lithium batteries, and supercapacitors, by introducing high-quality nanomaterials.

Above all, the architecture-function-construction-application relationship is urgently needed to provide comprehensive system and detailed theory for the facile preparation and designs of g-C₃N₄ CSNs. The properties of single component are constant during the synthesis process, which means that the increase in catalytic activity depends mainly on the interface. It can be considered that the interface and connecting surface are the most important embodiment of properties. The formation of interface can construct different heterojunctions, such as type-II and Z-scheme, which can enlarge light absorption section and charge separation, obtain new electronic structure by forming a Schottky junction, and form new functional complexes. Furthermore, regulating morphological characteristics and elemental composition of the g-C₃N₄ shells is a practical method to obtain high catalytic activity, such as synthesizing ultra-thin or mesoporous g-C₃N₄ nanosheets, doping metal atoms, and increasing N content. More efforts require us to pay to extend the g-C₃N₄ CSNs from the experimental phase to the real life. With advances in making good use of the filling and encapsulation of g-C₃N₄, we believe that the g-C₃N₄ CSNs will be more widely used in energy and environment in the future.

Acknowledgements

Thanks Min Cheng, Wenjun Wang, Chengyun Zhou for participation in the revision of the paper. This study was financially supported by the Program for the National Natural Science Foundation of China (51809090, 51879101, 51579098, 51779090, 51709101, 51521006, 51278176, 51378190), the National Program for Support of Top-Notch Young Professionals of China (2014), the Program for Changjiang Scholars and Innovative Research Team in University (IRT-13R17), and Hunan Provincial Science and Technology Plan Project (2018SK20410, 2017SK2243, 2016RS3026), the Natural Science Foundation of Hunan Province, China (Grant Nos. 2019JJ50077) and the Fundamental Research Funds for the Central Universities (531118010114, 531119200086, 531107050978).

References

- [1] Z. Zou, J. Ye, K. Sayama, H. Arakawa, Direct splitting of water under visible light irradiation with an oxide semiconductor photocatalyst, *Nature* 414 (2001) 625.
- [2] J. Liu, Y. Liu, N. Liu, Y. Han, X. Zhang, H. Huang, Y. Lifshitz, S.-T. Lee, J. Zhong, Z. Kang, Metal-free efficient photocatalyst for stable visible water splitting via a two-electron pathway, *Science* 347 (2015) 970–974.
- [3] B. Francesco, C. Luigi, Y. Guihua, S. Meryl, T. Valentina, A.C. Ferrari, R.S. Ruoff, P. Vittorio, Graphene, related two-dimensional crystals, and hybrid systems for energy conversion and storage, *Science* 347 (2015) 1246501.
- [4] C. Zhang, C. Lai, G. Zeng, D. Huang, C. Yang, Y. Wang, Y. Zhou, M. Cheng, Efficacy of carbonaceous nanocomposites for sorbing ionizable antibiotic sulfamethazine from aqueous solution, *Water Res.* 95 (2016) 103–112.
- [5] C. Zhang, W. Wang, A. Duan, G. Zeng, D. Huang, C. Lai, X. Tan, M. Cheng, R. Wang, C. Zhou, W. Xiong, Y. Yang, Adsorption behavior of engineered carbons and carbon nanomaterials for metal endocrine disruptors: experiments and theoretical calculation, *Chemosphere* 222 (2019) 184–194.
- [6] C. Zhang, G. Zeng, D. Huang, C. Lai, M. Chen, M. Cheng, W. Tang, L. Tang, H. Dong, B. Huang, X. Tan, R. Wang, Biochar for environmental management: Mitigating greenhouse gas emissions, contaminant treatment, and potential negative impacts, *Chem. Eng. J.* 373 (2019) 902–922.
- [7] B. Li, C. Lai, G. Zeng, L. Qin, H. Yi, D. Huang, C. Zhou, X. Liu, M. Cheng, P. Xu, Facile hydrothermal synthesis of Z-scheme Bi₂Fe₄O₉/Bi₂WO₆ heterojunction photocatalyst with enhanced visible light photocatalytic activity, *ACS Appl. Mater. Interfaces* 10 (2018) 18824–18836.
- [8] L. Li, C. Lai, F. Huang, M. Cheng, G. Zeng, D. Huang, B. Li, S. Liu, M. Zhang, L. Qin, M. Li, J. He, Y. Zhang, L. Chen, Degradation of naphthalene with magnetic biochar activate hydrogen peroxide: synergism of bio-char and Fe–Mn binary oxides, *Water Res.* 160 (2019) 238–248.
- [9] Y. Liu, Z. Liu, D. Huang, M. Cheng, G. Zeng, C. Lai, C. Zhang, C. Zhou, W. Wang, D. Jiang, H. Wang, B. Shao, Metal or metal-containing nanoparticle@MOF nanocomposites as a promising type of photocatalyst, *Coord. Chem. Rev.* 388 (2019) 63–78.
- [10] Y. Román-Leshkov, C.J. Barrett, Z.Y. Liu, J.A. Dumesic, Production of dimethylfuran for liquid fuels from biomass-derived carbohydrates, *Nature* 447 (2007) 982.
- [11] L. Jingshan, I. Jeong-Hyeok, M.T. Mayer, S. Marcel, N. Mohammad Khaja, P. Nam-

Gyu, T.S. David, F.H. Jin, G.T. Michael, Water photolysis at 12.3% efficiency via perovskite photovoltaics and Earth-abundant catalysts, *Science* 345 (2014) 1593–1596.

[12] Y. Zheng, J. Liu, J. Liang, M. Jaroniec, S.Z. Qiao, Graphitic carbon nitride materials: controllable synthesis and applications in fuel cells and photocatalysis, *Energy Environ. Sci.* 5 (2012) 6717–6731.

[13] Y. Yang, C. Zhang, C. Lai, G. Zeng, D. Huang, M. Cheng, J. Wang, F. Chen, C. Zhou, W. Xiong, BiOX (X = Cl, Br, I) photocatalytic nanomaterials: Applications for fuels and environmental management, *Adv. Colloid Interface Sci.* 254 (2018) 76–93.

[14] H. She, Y. Sun, S. Li, J. Huang, L. Wang, G. Zhu, Q. Wang, Synthesis of non noble metal nickel doped sulfide solid solution for improved photocatalytic performance, *Appl. Catal. B Environ.* 245 (2019) 439–447.

[15] Y. Yang, Z. Zeng, C. Zhang, D. Huang, G. Zeng, R. Xiao, C. Lai, C. Zhou, H. Guo, W. Xue, M. Cheng, W. Wang, J. Wang, Construction of iodine vacancy-rich BiOI/Ag@AgI Z-scheme heterojunction photocatalysts for visible-light-driven tetracycline degradation: transformation pathways and mechanism insight, *Chem. Eng. J.* 349 (2018) 808–821.

[16] S. Ye, M. Yan, X. Tan, J. Liang, G. Zeng, H. Wu, B. Song, C. Zhou, Y. Yang, H. Wang, Facile assembled biochar-based nanocomposite with improved graphitization for efficient photocatalytic activity driven by visible light, *Appl. Catal. B Environ.* 250 (2019) 78–88.

[17] L. Qin, D. Huang, P. Xu, G. Zeng, C. Lai, Y. Fu, H. Yi, B. Li, C. Zhang, M. Cheng, C. Zhou, X. Wen, In-situ deposition of gold nanoparticles onto polydopamine-decorated g-C₃N₄ for highly efficient reduction of nitroaromatics in environmental water purification, *J. Colloid Interface Sci.* 534 (2019) 357–369.

[18] D. Xu, B. Cheng, W. Wang, C. Jiang, J. Yu, Ag₂CrO₄/g-C₃N₄/graphene oxide ternary nanocomposite Z-scheme photocatalyst with enhanced CO₂ reduction activity, *Appl. Catal. B Environ.* 231 (2018) 368–380.

[19] H. She, Y. Wang, H. Zhou, Y. Li, L. Wang, J. Huang, Q. Wang, Preparation of Zn₃In₂S₆/TiO₂ for enhanced CO₂ photocatalytic reduction activity via Z-scheme electron transfer, *ChemCatChem* 11 (2019) 753–759.

[20] C. Zhou, P. Xu, C. Lai, C. Zhang, G. Zeng, D. Huang, M. Cheng, L. Hu, W. Xiong, X. Wen, L. Qin, J. Yuan, W. Wang, Rational design of graphic carbon nitride copolymers by molecular doping for visible-light-driven degradation of aqueous sulfamethazine and hydrogen evolution, *Chem. Eng. J.* 359 (2019) 186–196.

[21] L. Wang, S. Duan, P. Jin, H. She, J. Huang, Z. Lei, T. Zhang, Q. Wang, Anchored Cu (II) tetra(4-carboxylphenyl)porphyrin to P25 (TiO₂) for efficient photocatalytic ability in CO₂ reduction, *Appl. Catal. B Environ.* 239 (2018) 599–608.

[22] L. Qin, G. Zeng, C. Lai, D. Huang, C. Zhang, P. Xu, T. Hu, X. Liu, M. Cheng, Y. Liu, L. Hu, Y. Zhou, A visual application of gold nanoparticles: simple, reliable and sensitive detection of kanamycin based on hydrogen-bonding recognition, *Sens. Actuators B Chem.* 243 (2017) 946–954.

[23] C. Zhou, C. Lai, D. Huang, G. Zeng, C. Zhang, M. Cheng, L. Hu, J. Wan, W. Xiong, M. Wen, X. Wen, L. Qin, Highly porous carbon nitride by supramolecular pre-assembly of monomers for photocatalytic removal of sulfamethazine under visible light driven, *Appl. Catal. B Environ.* 220 (2018) 202–210.

[24] J. Ran, J. Zhang, J. Yu, M. Jaroniec, S.Z. Qiao, Earth-abundant cocatalysts for semiconductor-based photocatalytic water splitting, *Chem. Soc. Rev.* 43 (2014) 7787–7812.

[25] C. Zhou, C. Lai, P. Xu, G. Zeng, D. Huang, Z. Li, C. Zhang, M. Cheng, L. Hu, J. Wan, F. Chen, W. Xiong, R. Deng, Rational design of carbon-doped carbon nitride/Bi₁₂O₁₇Cl₂ composites: a promising candidate photocatalyst for boosting visible-light-driven photocatalytic degradation of tetracycline, *ACS Sustainable Chem. Eng.* 6 (2018) 6941–6949.

[26] Y. Yang, C. Zhang, D. Huang, G. Zeng, J. Huang, C. Lai, C. Zhou, W. Wang, H. Guo, W. Xue, R. Deng, M. Cheng, W. Xiong, Boron nitride quantum dots decorated ultrathin porous g-C₃N₄: intensified exciton dissociation and charge transfer for promoting visible-light-driven molecular oxygen activation, *Appl. Catal. B Environ.* 245 (2019) 87–99.

[27] W. Wang, P. Xu, M. Chen, G. Zeng, C. Zhang, C. Zhou, Y. Yang, D. Huang, C. Lai, M. Cheng, L. Hu, W. Xiong, H. Guo, M. Zhou, Alkali metal-assisted synthesis of graphite carbon nitride with tunable band-gap for enhanced visible-light-driven photocatalytic performance, *ACS Sustainable Chem. Eng.* 6 (2018) 15503–15516.

[28] D. Huang, H. Luo, C. Zhang, G. Zeng, C. Lai, M. Cheng, R. Wang, R. Deng, W. Xue, X. Gong, X. Guo, T. Li, Nonnegligible role of biomass types and its compositions on the formation of persistent free radicals in biochar: insight into the influences on Fenton-like process, *Chem. Eng. J.* 361 (2019) 353–363.

[29] L. Cui, B. Li, C. Ming, G. Zeng, D. Huang, Q. Lei, X. Liu, C. Min, W. Jia, C. Du, Simultaneous degradation of P-nitroaniline and electricity generation by using a microfiltration membrane dual-chamber microbial fuel cell, *Int. J. Hydrogen Energy* 43 (2018) 1749–1757.

[30] W. Wang, M. Chen, D. Huang, G. Zeng, C. Zhang, C. Lai, C. Zhou, Y. Yang, M. Cheng, L. Hu, W. Xiong, Z. Li, Z. Wang, An overview on nitride and nitrogen-doped photocatalysts for energy and environmental applications, *Composites Part B* 172 (2019) 704–723.

[31] J. LIEBIG, Über einige Stickstoff - Verbindungen, *Eur. J. Org. Chem.* 10 (1834) 1–47.

[32] Y. Wang, X. Wang, M. Antonietti, Polymeric graphitic carbon nitride as a heterogeneous organocatalyst: from photochemistry to multipurpose catalysis to sustainable chemistry, *Angew. Chem. Int. Ed.* 51 (2012) 68–89.

[33] W.J. Ong, L.L. Tan, Y.H. Ng, S.T. Yong, S.P. Chai, Graphitic carbon nitride (g-C₃N₄)-based photocatalysts for artificial photosynthesis and environmental remediation: are we a step closer to achieving sustainability? *Chem. Rev.* 116 (2016) 7159–7329.

[34] S. Cao, J. Low, J. Yu, M. Jaroniec, Polymeric photocatalysts based on graphitic carbon nitride, *Adv. Mater.* 27 (2015) 2150–2176.

[35] G. Gao, Y. Jiao, E.R. Waclawik, A. Du, Single atom (Pd/Pt) supported on graphitic carbon nitride as an efficient photocatalyst for visible-light reduction of carbon dioxide, *J. Am. Chem. Soc.* 138 (2016) 6292–6297.

[36] G. Mamba, A.K. Mishra, Graphitic carbon nitride (g-C₃N₄) nanocomposites: a new and exciting generation of visible light driven photocatalysts for environmental pollution remediation, *Appl. Catal. B Environ.* 198 (2016) 347–377.

[37] K.S. Lakhi, D.-H. Park, K. Al-Bahily, W. Cha, B. Viswanathan, J.H. Choy, A. Vinu, Mesoporous carbon nitrides: synthesis, functionalization, and applications, *Chem. Soc. Rev.* 46 (2017) 72–101.

[38] Y. Zheng, L. Lin, B. Wang, X. Wang, Graphitic carbon nitride polymers toward sustainable photoredox catalysis, *Angew. Chem. Int. Ed.* 54 (2015) 12868–12884.

[39] G. Shiravand, A. Badie, G. Mohammadi Ziarani, Carboxyl-rich g-C₃N₄ nanoparticles: Synthesis, characterization and their application for selective fluorescence sensing of Hg²⁺ and Fe³⁺ in aqueous media, *Sens. Actuators B Chem.* 242 (2017) 244–252.

[40] J. Wen, J. Xie, X. Chen, X. Li, A review on g-C₃N₄-based photocatalysts, *Appl. Surf. Sci.* 391 (2017) 72–123.

[41] M. Zhu, C. Zhai, M. Sun, Y. Hu, B. Yan, Y. Du, Ultrathin graphitic C₃N₄ nanosheet as a promising visible-light-activated support for boosting photoelectrocatalytic methanol oxidation, *Appl. Catal. B Environ.* 203 (2017) 108–115.

[42] S. Guo, Z. Deng, M. Li, B. Jiang, C. Tian, Q. Pan, H. Fu, Phosphorus-doped carbon nitride tubes with a layered micro-nanostructure for enhanced visible-light photocatalytic hydrogen evolution, *Angew. Chem. Int. Ed.* 55 (2016) 1830–1834.

[43] S.J.A. Moniz, S.A. Shevlin, D.J. Martin, Z.X. Guo, J. Tang, Visible-light driven heterojunction photocatalysts for water splitting – a critical review, *Energy Environ. Sci.* 8 (2015) 731–759.

[44] A. Bafaqeer, M. Tahir, N.A.S. Amin, Well-designed ZnV₂O₆/g-C₃N₄ 2D/2D nanosheets heterojunction with faster charges separation via pCN as mediator towards enhanced photocatalytic reduction of CO₂ to fuels, *Appl. Catal. B Environ.* 242 (2019) 312–326.

[45] J. Qin, J. Huo, P. Zhang, J. Zeng, T. Wang, H. Zeng, Improving the photocatalytic hydrogen production of Ag/g-C₃N₄ nanocomposites by dye-sensitization under visible light irradiation, *Nanoscale* 8 (2016) 2249–2259.

[46] J. Wang, D. Liu, Q. Liu, T. Peng, R. Li, S. Zhou, Effects of the central metal ions on the photosensitization of metalloporphyrins over carbon nitride for visible-light-responsive H₂ production, *Appl. Surf. Sci.* 464 (2019) 255–261.

[47] S.H. Joo, J.Y. Park, C.K. Tsung, Y. Yamada, P. Yang, G.A. Somorjai, Thermally stable Pt/mesoporous silica core-shell nanocatalysts for high-temperature reactions, *Nat. Mater.* 8 (2008) 126.

[48] S. Wei, Q. Wang, J. Zhu, L. Sun, H. Lin, Z. Guo, Multifunctional composite core-shell nanoparticles, *Nanoscale* 3 (2011) 4474–4502.

[49] R. Ghosh Chaudhuri, S. Paria, Core/shell nanoparticles: classes, properties, synthesis mechanisms, characterization, and applications, *Chem. Rev.* 112 (2012) 2373–2433.

[50] W. Li, D. Zhao, Extension of the stöber method to construct mesoporous SiO₂ and TiO₂ shells for uniform multifunctional core-shell structures, *Adv. Mater.* 25 (2013) 142–149.

[51] A. Guerrero-Martínez, J. Pérez-Juste, L.M. Liz-Marzán, Recent progress on silica coating of nanoparticles and related nanomaterials, *Adv. Mater.* 22 (2010) 1182–1195.

[52] M.B. Gawande, A. Goswami, T. Asefa, H. Guo, A.V. Biradar, D.L. Peng, R. Zboril, R.S. Varma, Core-shell nanoparticles: synthesis and applications in catalysis and electrocatalysis, *Chem. Soc. Rev.* 44 (2015) 7540–7590.

[53] F. Zhang, R. Che, X. Li, C. Yao, J. Yang, D. Shen, P. Hu, W. Li, D. Zhao, Direct imaging the upconversion nanocrystal core/shell structure at the subnanometer level: Shell thickness dependence in upconverting optical properties, *Nano Lett.* 12 (2012) 2852–2858.

[54] X. Qian, Y. Lv, W. Li, Y. Xia, D. Zhao, Multiwall carbon nanotube@mesoporous carbon with core-shell configuration: a well-designed composite-structure toward electrochemical capacitor application, *J. Mater. Chem.* 21 (2011) 13025–13031.

[55] Q. Zhang, J. Lee, J.B. Joo, F. Zaera, Y. Yin, Core-Shell nanostructured catalysts, *Acc. Chem. Res.* 46 (2013) 1816–1824.

[56] W. Wang, J. Fang, S. Shao, M. Lai, C. Lu, Compact and uniform TiO₂@g-C₃N₄ core-shell quantum heterojunction for photocatalytic degradation of tetracycline antibiotics, *Appl. Catal. B Environ.* 217 (2017) 57–64.

[57] S. Yi, J.M. Yan, Q. Jiang, Carbon quantum dots sensitized fully integrated Fe₂O₃@g-C₃N₄ core-shell nanoarrays photoanode towards highly efficient water oxidation, *J. Mater. Chem. A* 6 (2018) 9839–9845.

[58] C.Z. Li, Z.B. Wang, X.L. Sui, L.M. Zhang, D.M. Gu, S. Gu, Graphitic carbon nitride nanosheet coated carbon black as a high-performance PtRu catalyst support material for methanol electrooxidation, *J. Mater. Chem. A* 2 (2014) 20139–20146.

[59] C. S, L. J, Y. J, J. M, Polymeric photocatalysts based on graphitic carbon nitride, *Adv. Mater.* 27 (2015) 2150–2176.

[60] D.F. Li, W.Q. Huang, L.R. Zou, A. Pan, G.F. Huang, Mesoporous g-C₃N₄ nanosheets: synthesis, superior adsorption capacity and photocatalytic activity, *J. Nanosci. Nanotechnol.* 18 (2018) 5502–5510.

[61] S. Sun, S. Liang, Recent advances in functional mesoporous graphitic carbon nitride (mpg-C₃N₄) polymers, *Nanoscale* 9 (2017) 10544–10578.

[62] Z. Zhao, Y. Sun, F. Dong, Graphitic carbon nitride based nanocomposites: a review, *Nanoscale* 7 (2015) 15–37.

[63] L. Jiang, X. Yuan, Y. Pan, J. Liang, G. Zeng, Z. Wu, H. Wang, Doping of graphitic carbon nitride for photocatalysis: a review, *Appl. Catal. B Environ.* 217 (2017) 388–406.

[64] W. Jiang, H. Wang, X. Zhang, Y. Zhu, Y. Xie, Two-dimensional polymeric carbon nitride: structural engineering for optimizing photocatalysis, *Sci. China Chem.* 61 (2018) 1205–1213.

[65] J. Zhang, Y. Chen, X. Wang, Two-dimensional covalent carbon nitride nanosheets: synthesis, functionalization, and applications, *Energy Environ. Sci.* 8 (2015) 3092–3108.

[66] D.M. Gawande, A. Goswami, T. Asefa, H. Guo, A. Biradar, D.-L. Peng, R. Zboril, R. Varma, Core-shell nanoparticles: synthesis and applications in catalysis and electrocatalysis, *Chem. Soc. Rev.* 44 (2015) 7540–7590.

[67] H. Zhu, G. Gao, M. Du, J. Zhou, K. Wang, W. Wu, X. Chen, Y. Li, P. Ma, W. Dong, F. Duan, M. Chen, G. Wu, J. Wu, H. Yang, S. Guo, Atomic-scale core/shell structure engineering induces precise tensile strain to boost hydrogen evolution catalysis, *Adv. Mater.* 30 (2018) 1707301.

[68] Q. Wang, S. Chen, P. Li, S. Ibraheem, J. Li, J. Deng, Z. Wei, Surface Ru enriched structurally ordered intermetallic PtFe@PtRuFe core-shell nanostructure boosts methanol oxidation reaction catalysis, *Appl. Catal. B Environ.* 252 (2019) 120–127.

[69] H.P. Feng, L. Tang, G.M. Zeng, Y. Zhou, Y.C. Deng, X. Ren, B. Song, C. Liang, M.Y. Wei, J.F. Yu, Core-shell nanomaterials: applications in energy storage and conversion, *Adv. Colloid Interface Sci.* 267 (2019) 26–46.

[70] L. Li, Y. Hao, J. Guo, Y. Wang, L. Yu, A novel Ag nanoprism@SiO₂@QD composite nanostructure for nano-optics, *Chem. Phys. Lett.* 711 (2018) 178–183.

[71] L. Wang, X. Liu, J. Luo, X. Duan, J. Crittenden, C. Liu, S. Zhang, Y. Pei, Y. Zeng, X. Duan, Self-optimization of the active site of molybdenum disulfide by an irreversible phase transition during photocatalytic hydrogen evolution, *Angew. Chem. Int. Ed.* 56 (2017) 7610–7614.

[72] Y. Wang, Z. Luo, Z. Wang, M. You, S. Xie, Y. Peng, H. Yang, Effect of curcumin-loaded nanoparticles on mitochondrial dysfunctions of breast cancer cells, *J. Nanopart. Res.* 20 (2018) 283.

[73] M. Chen, J.H. Wang, Z.J. Luo, Z.Q. Cheng, Y.F. Zhang, X.F. Yu, L. Zhou, Q. Wang, Facile synthesis of flower-shaped Au/GdVO₄:Eu core/shell nanoparticles by using citrate as stabilizer and complexing agent, *RSC Adv.* 6 (2016) 9612–9618.

[74] R. Kumar, H. Choudhary, S. Pawar, S. Bose, D.B. Sahoo, Carbon encapsulated nanoscale iron/iron-carbide/graphite particles for EMI shielding and microwave absorption, *Phys. Chem. Chem. Phys.* 19 (2017) 23268–23279.

[75] S.H. Chung, C.H. Chang, A. Manthiram, A core-shell electrode for dynamically and statically stable Li-S battery chemistry, *Energy Environ. Sci.* 9 (2016) 3188–3200.

[76] X. Chen, D. Peng, Q. Ju, F. Wang, Photon upconversion in core-shell nanoparticles, *Chem. Soc. Rev.* 44 (2015) 1318–1330.

[77] H.P. Feng, L. Tang, G.M. Zeng, J. Tang, Y.C. Deng, M. Yan, Y.N. Liu, Y.Y. Zhou, X.Y. Ren, S. Chen, Carbon-based core-shell nanostructured materials for electrochemical energy storage, *J. Mater. Chem. A* 6 (2018) 7310–7337.

[78] H. Jia, R. Roa, S. Angioletti-Uberti, K. Henzler, A. Ott, X. Lin, J. Möser, Z. Kochovski, A. Schnegg, J. Dzubiella, M. Ballauff, Y. Lu, Thermosensitive Cu₂O-PNIPAM core-shell nanoreactors with tunable photocatalytic activity, *J. Mater. Chem. A* 4 (2016) 9677–9684.

[79] Y. Zou, J.W. Shi, D. Ma, Z. Fan, L. Lu, C. Niu, In situ synthesis of C-doped TiO₂@g-C₃N₄ core-shell hollow nanospheres with enhanced visible-light photocatalytic activity for H₂ evolution, *Chem. Eng. J.* 322 (2017) 435–444.

[80] N. Guo, Y. Zeng, H. Li, X. Xu, H. Yu, X. Han, Novel mesoporous TiO₂@g-C₃N₄ hollow core@shell heterojunction with enhanced photocatalytic activity for water treatment and H₂ production under simulated sunlight, *J. Hazard. Mater.* 353 (2018) 80–88.

[81] N. Chaoui, M. Trunk, R. Dawson, J. Schmidt, A. Thomas, Trends and challenges for microporous polymers, *Chem. Soc. Rev.* 46 (2017) 3302–3321.

[82] J. Lin, W.J. Ong, Z. Rui, E. Pickwell-Macpherson, J.C. Yu, Graphitic carbon nitride nanosheet wrapped mesoporous titanium dioxide for enhanced photoelectrocatalytic water splitting, *Catal. Today* 315 (2018) 103–109.

[83] H. Wei, W.A. McMaster, J.Z.Y. Tan, L. Cao, D. Chen, R.A. Caruso, Mesoporous TiO₂/g-C₃N₄ microspheres with enhanced visible-light photocatalytic activity, *J. Phys. Chem. C* 121 (2017) 22114–22122.

[84] Y. Wu, J. Ward-Bond, D. Li, S. Zhang, J. Shi, Z. Jiang, g-C₃N₄@α-Fe₂O₃/C Photocatalysts: synergistically intensified charge generation and charge transfer for NADH regeneration, *ACS Catal.* 8 (2018) 5664–5674.

[85] J. Wang, Y. Xia, H. Zhao, G. Wang, L. Xiang, J. Xu, S. Komarneni, Oxygen defects-mediated Z-scheme charge separation in g-C₃N₄/ZnO photocatalysts for enhanced visible-light degradation of 4-chlorophenol and hydrogen evolution, *Appl. Catal. B Environ.* 206 (2017) 406–416.

[86] M. Li, L. Zhang, X. Fan, M. Wu, M. Wang, R. Cheng, L. Zhang, H. Yao, J. Shi, Core-shell LaPO₄/g-C₃N₄ nanowires for highly active and selective CO₂ reduction, *Appl. Catal. B Environ.* 201 (2017) 629–635.

[87] S.S. Yi, J.M. Yan, Q. Jiang, Carbon quantum dot sensitized integrated Fe₂O₃@g-C₃N₄ core-shell nanoarray photoanode towards highly efficient water oxidation, *J. Mater. Chem. A* 6 (2018) 9839–9845.

[88] Z. Chen, G. Ma, Z. Chen, Y. Zhang, Z. Zhang, J. Gao, Q. Meng, M. Yuan, X. Wang, J.M. Liu, Fabrication and photoelectrochemical properties of silicon nanowires/g-C₃N₄ core/shell arrays, *Appl. Surf. Sci.* 396 (2017) 609–615.

[89] L. Liu, Y. Qi, J. Hu, Y. Liang, W. Cui, Efficient visible-light photocatalytic hydrogen evolution and enhanced photostability of core@shell Cu₂O@g-C₃N₄ octahedra, *Appl. Surf. Sci.* 351 (2015) 1146–1154.

[90] Z. Wu, L. Hui, Z. Xu, L. Guan, S. Jian, J. Wu, X. Ning, Construction of graphitic carbon nitride/rutile-TiO₂ core-shell nanocone arrays by pulsed laser deposition and plasma sputtering reaction deposition, *Mater. Lett.* 227 (2018) 37–39.

[91] E. Negro, A. Nale, K. Vezzù, G. Pagot, S. Polizzi, R. Bertoncello, A. Ansaldi, M. Prato, F. Bonaccorso, I.A. Rutkowska, P.J. Kulesza, V. Di Noto, Hierarchical oxygen reduction reaction electrocatalysts based on FeSn_{0.5} species embedded in carbon nitride-graphene based supports, *Electrochim. Acta* 280 (2018) 149–162.

[92] C. Feng, Y. Deng, L. Tang, G. Zeng, J. Wang, J. Yu, Y. Liu, B. Peng, H. Feng, J. Wang, Core-shell Ag₂CrO₄/N-GQDs@g-C₃N₄ composites with anti-photocorrosion performance for enhanced full-spectrum-light photocatalytic activities, *Appl. Catal. B Environ.* 239 (2018) 525–536.

[93] K. Wang, Y. Li, G. Zhang, J. Li, X. Wu, OD Bi nanodots/2D Bi₃NbO₇ nanosheets heterojunctions for efficient visible light photocatalytic degradation of antibiotics: enhanced molecular oxygen activation and mechanism insight, *Appl. Catal. B Environ.* 240 (2019) 39–49.

[94] S. Zhang, J. Li, X. Wang, Y. Huang, M. Zeng, J. Xu, Rationally designed 1D Ag@AgVO₃ nanowire/graphene/protonated g-C₃N₄ nanosheet heterojunctions for enhanced photocatalysis via electrostatic self-assembly and photochemical reduction methods, *J. Mater. Chem. A* 3 (2015) 10119–10126.

[95] Z. Zhang, D. Jiang, D. Li, M. He, M. Chen, Construction of SnNb₂O₆ nanosheet/g-C₃N₄ nanosheet two-dimensional heterostructures with improved photocatalytic activity: synergistic effect and mechanism insight, *Appl. Catal. B Environ.* 183 (2016) 113–123.

[96] L. Zhang, D. Jing, X. She, H. Liu, D. Yang, Y. Lu, J. Li, Z. Zheng, L. Guo, Heterojunctions in g-C₃N₄/TiO₂(B) nanofibres with exposed (001) plane and enhanced visible-light photoactivity, *J. Mater. Chem. A* 2 (2014) 2071–2078.

[97] X. Li, M. Li, J. Yang, X. Li, T. Hu, J. Wang, Y. Sui, X. Wu, L. Kong, Synergistic effect of efficient adsorption g-C₃N₄/ZnO composite for photocatalytic property, *J. Phys. Chem. Solids* 75 (2014) 441–446.

[98] Z. Zhang, J. Huang, M. Zhang, Q. Yuan, B. Dong, Ultrathin hexagonal SnS₂ nanosheets coupled with g-C₃N₄ nanosheets as 2D/2D heterojunction photocatalysts toward high photocatalytic activity, *Appl. Catal. B Environ.* 163 (2015) 298–305.

[99] H. Shen, X. Zhao, L. Duan, R. Liu, H. Li, Enhanced visible light photocatalytic activity in SnO₂@g-C₃N₄ core-shell structures, *Mater. Sci. Eng. B* 218 (2017) 23–30.

[100] Y. Yao, F. Lu, Y. Zhu, F. Wei, X. Liu, C. Lian, S. Wang, Magnetic core-shell CuFe₂O₄@g-C₃N₄ hybrids for visible light photocatalysis of Orange II, *J. Hazard. Mater.* 297 (2015) 224–233.

[101] Z. You, Q. Shen, Y. Su, Y. Yu, H. Wang, T. Qin, F. Zhang, D. Cheng, H. Yang, Construction of a Z-scheme core-shell g-C₃N₄/MCNTs/BiOI nanocomposite semiconductor with enhanced visible-light photocatalytic activity, *New J. Chem.* 42 (2018) 489–496.

[102] C. Yin, L. Cui, T. Pu, X. Fang, H. Shi, S. Kang, X. Zhang, Facile fabrication of nanosized hollow-CdS@g-C₃N₄ core-shell spheres for efficient visible-light-driven hydrogen evolution, *Appl. Surf. Sci.* 456 (2018) 464–472.

[103] J. Zhang, Y. Wang, J. Jin, J. Zhang, Z. Lin, F. Huang, J. Yu, Efficient visible-light photocatalytic hydrogen evolution and enhanced photostability of core/shell CdS/g-C₃N₄ nanowires, *ACS Appl. Mater. Interfaces* 5 (2013) 10317–10324.

[104] Y. Yao, F. Lu, Y. Zhu, F. Wei, X. Liu, C. Lian, S. Wang, Magnetic core-shell CuFe₂O₄@g-C₃N₄ hybrids for visible light photocatalysis of Orange II, *J. Hazard. Mater.* 297 (2015) 224–233.

[105] M.N. Kashid, A. Renken, L. Kiwi-Minsker, Gas-liquid and liquid-liquid mass transfer in microstructured reactors, *Chem. Eng. Sci.* 66 (2011) 3876–3897.

[106] D. Chen, F. Li, A.K. Ray, External and internal mass transfer effect on photocatalytic degradation, *Catal. Today* 66 (2001) 475–485.

[107] K. Mehrotra, G.S. Yablonsky, A.K. Ray, Macro kinetic studies for photocatalytic degradation of benzoic acid in immobilized systems, *Chemosphere* 60 (2005) 1427–1436.

[108] J.T. Richardson, D. Remue, J.K. Hung, Properties of ceramic foam catalyst supports: mass and heat transfer, *Appl. Catal. A Gen.* 250 (2003) 319–329.

[109] D. Chen, K. Wang, D. Xiang, R. Zong, W. Yao, Y. Zhu, Significantly enhancement of photocatalytic performances via core-shell structure of ZnO@mpg-C₃N₄, *Appl. Catal. B Environ.* 147 (2014) 554–561.

[110] B. Boulinguez, A. Bouaza, S. Merabet, D. Wolbert, Photocatalytic degradation of ammonia and butyric acid in plug-flow reactor: degradation kinetic modeling with contribution of mass transfer, *J. Photochem. Photobiol. A* 200 (2008) 254–261.

[111] A.G. Yiotis, I.N. Tsimpanogiannis, A.K. Stubos, Y.C. Yortsos, Coupling between external and internal mass transfer during drying of a porous medium, *Water Resour. Res.* 43 (2007).

[112] Z. Xing, Y. Chen, C. Liu, J. Yang, J. Xu, Y. Situ, H. Huang, Synthesis of core-shell ZnO/oxygen doped g-C₃N₄ visible light driven photocatalyst via hydrothermal method, *J. Alloys. Compd.* 708 (2017) 853–861.

[113] K. Vezzù, A. Bach Delpeuch, E. Negro, S. Polizzi, G. Nawn, F. Bertasi, G. Pagot, K. Artyushkova, P. Atanassov, V. Di Noto, Fe-carbon nitride “Core-shell” electrocatalysts for the oxygen reduction reaction, *Electrochim. Acta* 222 (2016) 1778–1791.

[114] E. Negro, A. Bach Delpeuch, K. Vezzù, G. Nawn, F. Bertasi, A. Ansaldi, V. Pellegrini, B. Dembinska, S. Zoladek, K. Miecznikowski, I.A. Rutkowska, M. Skunick-Nuckowska, P.J. Kulesza, F. Bonaccorso, V. Di Noto, Toward Pt-free anion-exchange membrane fuel cells: Fe–Sn carbon nitride–graphene core–shell electrocatalysts for the oxygen reduction reaction, *Chem. Mater.* 30 (2018) 2651–2659.

[115] J. Jin, X. Fu, Q. Liu, J. Zhang, A highly active and stable electrocatalyst for the oxygen reduction reaction based on a graphene-supported g-C₃N₄/cobalt oxide core–shell hybrid in alkaline solution, *J. Mater. Chem. A* 1 (2013) 10538.

[116] Q. Gu, H. Sun, Z. Xie, Z. Gao, C. Xue, MoS₂-coated microspheres of self-sensitized carbon nitride for efficient photocatalytic hydrogen generation under visible light irradiation, *Appl. Surf. Sci.* 396 (2017) 1808–1815.

[117] L. Ma, G. Wang, C. Jiang, H. Bao, Q. Xu, Synthesis of core-shell TiO₂@g-C₃N₄ hollow microspheres for efficient photocatalytic degradation of rhodamine B under visible light, *Appl. Surf. Sci.* 430 (2018) 263–272.

[118] M. Wang, P. Guo, Y. Zhang, T. Liu, S. Li, Y. Xie, Y. Wang, T. Zhu, Eu doped g-C₃N₄ nanosheet coated on flower-like BiVO₄ powders with enhanced visible light photocatalytic for tetracycline degradation, *Appl. Surf. Sci.* 453 (2018) 11–22.

[119] C. Yang, W. Zhao, X. Yu, H. Liu, J. Liu, R. Vandeven, Z. Liu, Facile synthesis and

luminescence property of core-shell structured $\text{NaYF}_4\text{-Yb,Er/g-C}_3\text{N}_4$ nanocomposites, *Mater. Res. Bull.* 94 (2017) 415–422.

[120] J. Hao, S. Zhang, F. Ren, Z. Wang, J. Lei, X. Wang, T. Cheng, L. Li, Synthesis of $\text{TiO}_2\text{@g-C}_3\text{N}_4$ core-shell nanorod arrays with Z-scheme enhanced photocatalytic activity under visible light, *J. Colloid Interface Sci.* 508 (2017) 419.

[121] Y. Wang, W. Yang, X. Chen, J. Wang, Y. Zhu, Photocatalytic activity enhancement of core-shell structure $\text{g-C}_3\text{N}_4\text{@TiO}_2$ via controlled ultrathin $\text{g-C}_3\text{N}_4$ layer, *Appl. Catal. B Environ.* 220 (2018) 337–347.

[122] Y. Wang, Q. Wu, Y. Li, L. Liu, Z. Geng, Y. Li, J. Chen, W. Bai, G. Jiang, Z. Zhao, Controlled fabrication of $\text{TiO}_2\text{/C}_3\text{N}_4$ core-shell nanowire arrays: a visible-light-responsive and environmental-friendly electrode for photoelectrocatalytic degradation of bisphenol A, *J. Mater. Sci.* 53 (2018) 11015–11026.

[123] S.G. Khasevani, N. Mohaghegh, M.R. Gholami, Kinetic study of navy blue photocatalytic degradation over $\text{Ag}_3\text{PO}_4\text{/BiPO}_4\text{@MIL-88B(Fe)}$ @ $\text{g-C}_3\text{N}_4$ core@shell nanocomposite under visible light irradiation, *New J. Chem.* 41 (2017) 10390–10396.

[124] S.G. Khasevani, M.R. Gholami, Engineering a highly dispersed core@shell structure for efficient photocatalysis: A case study of ternary novel BiOI@MIL-88A(Fe) @ $\text{g-C}_3\text{N}_4$ nanocomposite, *Mater. Res. Bull.* 106 (2018) 93–102.

[125] Y. Z., S. Z., L. X., J. H., D. P., Cadmium sulfide/graphitic carbon nitride heterostructure nanowire loading with a nickel hydroxide cocatalyst for highly efficient photocatalytic hydrogen production in water under visible light, *Nanoscale* 8 (2016) 4748–4756.

[126] F. Zhang, L. Wang, M. Xiao, F. Liu, X. Xu, E. Du, Construction of direct solid-state Z-scheme $\text{g-C}_3\text{N}_4\text{/BiOI}$ with improved photocatalytic activity for microcystin-LR degradation, *J. Mater. Res. Sci.* 33 (2017) 1–12.

[127] L. Liu, Y. Qi, J. Yang, W. Cui, X. Li, Z. Zhang, An $\text{AgI@g-C}_3\text{N}_4$ hybrid core@shell structure: stable and enhanced photocatalytic degradation, *Appl. Surf. Sci.* 358 (2015) 319–327.

[128] L. Li, Y. Qi, J. Lu, S. Lin, W. An, Y. Liang, W. Cui, A stable $\text{Ag}_2\text{PO}_4\text{@g-C}_3\text{N}_4$ hybrid core@shell composite with enhanced visible light photocatalytic degradation, *Appl. Catal. B Environ.* 183 (2016) 133–141.

[129] L. Liu, P. Hu, W. Cui, X. Li, Z. Zhang, Increased photocatalytic hydrogen evolution and stability over nano-sheet $\text{g-C}_3\text{N}_4$ hybridized CdS core@shell structure, *Int. J. Hydrogen Energy* 42 (2017) 17435–17445.

[130] X. Dang, X. Zhang, W. Zhang, X. Dong, G. Wang, C. Ma, X. Zhang, H. Ma, M. Xue, Ultra-thin C_3N_4 nanosheets for rapid charge transfer in the core-shell heterojunction of a-sulfur@ C_3N_4 for superior metal-free photocatalysis under visible light, *RSC Adv.* 5 (2015) 15052–15058.

[131] C. Pan, J. Xu, Y. Wang, D. Li, Y. Zhu, Dramatic activity of $\text{C}_3\text{N}_4\text{/BiPO}_4$ photocatalyst with Core/Shell structure formed by self-assembly, *Adv. Funct. Mater.* 22 (2012) 1518–1524.

[132] B. Lin, C. Xue, X. Yan, G. Yang, G. Yang, B. Yang, Facile fabrication of novel $\text{SiO}_2\text{/g-C}_3\text{N}_4$ core-shell nanosphere photocatalysts with enhanced visible light activity, *Appl. Surf. Sci.* 357 (2015) 346–355.

[133] L. Wang, C. Ma, Z. Guo, Y. Lv, W. Chen, Z. Chang, Q. Yuan, H. Ming, J. Wang, In-situ growth of $\text{g-C}_3\text{N}_4$ layer on ZnO nanoparticles with enhanced photocatalytic performances under visible light irradiation, *Mater. Lett.* 188 (2017) 347–350.

[134] Y. Li, X. Wei, H. Li, R. Wang, J. Feng, H. Yun, A. Zhou, Fabrication of inorganic-organic core-shell heterostructure: novel $\text{CdS@g-C}_3\text{N}_4$ nanorod arrays for photoelectrochemical hydrogen evolution, *RSC Adv.* 5 (2015) 14074–14080.

[135] L. Ma, H. Fan, K. Fu, S. Lei, Q. Hu, H. Huang, G. He, Protonation of graphitic carbon nitride ($\text{g-C}_3\text{N}_4$) for an electrostatically self-assembling Carbon@ $\text{g-C}_3\text{N}_4$ core-Shell nanostructure toward high hydrogen evolution, *ACS Sustainable Chem. Eng.* 5 (2017) 7093–7103.

[136] M.A. Mohamed, J. Jaafer, M.F.M. Zain, L.J. Minggu, M.B. Kassim, M.S. Rosmi, N.H. Alias, N.A.M. Nor, W.N.W. Salleh, M.H.D. Othman, In-depth understanding of core-shell nanoarchitecture evolution of $\text{g-C}_3\text{N}_4\text{@C}_6\text{N}$ co-doped anatase/rutile: efficient charge separation and enhanced visible-light photocatalytic performance, *Appl. Surf. Sci.* 436 (2018) 302–318.

[137] T.J. Park, R.C. Pawar, S. Kang, C.S. Lee, Ultra-thin coating of $\text{g-C}_3\text{N}_4$ on an aligned ZnO nanorod film for rapid charge separation and improved photodegradation performance, *RSC Adv.* 6 (2016) 89944–89952.

[138] V.D. Noto, E. Negro, Development of nano-electrocatalysts based on carbon nitride supports for the ORR processes in PEM fuel cells, *Electrochim. Acta* 55 (2010) 7564–7574.

[139] N. Mansor, T.S. Miller, I. Dedigama, A.B. Jorge, J. Jia, V. Brázdová, C. Mattevi, C. Gibbs, D. Hodgson, P.R. Shearing, C.A. Howard, F. Corà, M. Shaffer, D.J.L. Brett, P.F. McMillan, Graphitic carbon nitride as a catalyst support in fuel cells and electrolyzers, *Electrochim. Acta* 222 (2016) 44–57.

[140] E. Negro, K. Vezzù, F. Bertasi, P. Schiavuta, L. Toniolo, S. Polizzi, V. Di Noto, Interplay between nitrogen concentration, structure, morphology, and electrochemical performance of PdCoNi “core-shell” carbon nitride electrocatalysts for the oxygen reduction reaction, *Chemelectrochem.* 1 (2015) 1359–1369.

[141] X. Bai, R. Zong, C. Li, D. Liu, Y. Liu, Y. Zhu, Enhancement of visible photocatalytic activity via $\text{Ag@C}_3\text{N}_4$ core-shell plasmonic composite, *Appl. Catal. B Environ.* 147 (2014) 82–91.

[142] F.Y. Tian, D. Hou, F. Tang, M. Deng, X.Q. Qiao, Q. Zhang, T. Wu, D.S. Li, Novel $\text{Zn}_{0.8}\text{Cd}_{0.2}\text{S@g-C}_3\text{N}_4$ core-shell heterojunctions with a twin structure for enhanced visible-light-driven photocatalytic hydrogen generation, *J. Mater. Chem. A* 6 (2018) 17086–17094.

[143] C. Zhang, C. Lai, G. Zeng, D. Huang, L. Tang, C. Yang, Y. Zhou, L. Qin, M. Cheng, Nanoporous Au-based chronocoulometric aptasensor for amplified detection of Pb^{2+} using DNAzyme modified with Au nanoparticles, *Biosens. Bioelectron.* 81 (2016) 61–67.

[144] D. Huang, W. Xue, G. Zeng, J. Wan, G. Chen, C. Huang, C. Zhang, M. Cheng, P. Xu, Immobilization of Cd in river sediments by sodium alginate modified nanoscale zero-valent iron: impact on enzyme activities and microbial community diversity, *Water Res.* 106 (2016) 15–25.

[145] D. Huang, L. Liu, G. Zeng, P. Xu, C. Huang, L. Deng, R. Wang, J. Wan, The effects of rice straw biochar on indigenous microbial community and enzymes activity in heavy metal-contaminated sediment, *Chemosphere* 174 (2017) 545–553.

[146] W. Xue, D. Huang, G. Zeng, J. Wan, C. Zhang, R. Xu, M. Cheng, R. Deng, Nanoscale zero-valent iron coated with rhamnolipid as an effective stabilizer for immobilization of Cd and Pb in river sediments, *J. Hazard. Mater.* 341 (2018) 381–389.

[147] X. Gong, D. Huang, Y. Liu, G. Zeng, R. Wang, J. Wei, C. Huang, P. Xu, J. Wan, C. Zhang, Pyrolysis and reutilization of plant residues after phytoremediation of heavy metals contaminated sediments: for heavy metals stabilization and dye adsorption, *Bioreour. Technol.* 253 (2018) 64–71.

[148] X. Gong, D. Huang, Y. Liu, G. Zeng, R. Wang, J. Wan, C. Zhang, M. Cheng, X. Qin, W. Xue, Stabilized nanoscale zero-valent iron mediated cadmium accumulation and oxidative damage of *Boehmeria nivea* (L.) Gaudich cultivated in cadmium contaminated sediments, *Environ. Sci. Technol.* 51 (2017) 11308–11316.

[149] D. Huang, R. Deng, J. Wan, G. Zeng, W. Xue, X. Wen, C. Zhou, L. Hu, X. Liu, P. Xu, Remediation of lead-contaminated sediment by biochar-supported nano-chlorapatite: accompanied with the change of available phosphorus and organic matters, *J. Hazard. Mater.* 348 (2018) 109–116.

[150] C. Hu, D. Huang, G. Zeng, C. Min, X. Gong, R. Wang, W. Xue, Z. Hu, Y. Liu, The combination of Fenton process and *Phanerochaete chrysosporium* for the removal of bisphenol A in river sediments: mechanism related to extracellular enzyme, organic acid and iron, *Chem. Eng. J.* 338 (2018) 432–439.

[151] R.Z. Wang, D.L. Huang, Y.G. Liu, C. Zhang, C. Lai, G.M. Zeng, M. Cheng, X.M. Gong, J. Wan, H. Luo, Investigating the adsorption behavior and the relative distribution of Cd^{2+} sorption mechanisms on biochars by different feedstock, *Bioreour. Technol.* 261 (2018) 265–271.

[152] X. Guo, Z. Peng, D. Huang, P. Xu, G. Zeng, S. Zhou, X. Gong, M. Cheng, R. Deng, H. Yi, H. Luo, X. Yan, T. Li, Biotransformation of cadmium-sulfamethazine combined pollutant in aqueous environments: *phanerochaete chrysosporium* bring cautious optimism, *Chem. Eng. J.* 347 (2018) 74–83.

[153] Y. Wei, Y. Zhu, Y. Jiang, Photocatalytic self-cleaning carbon nitride nanotube intercalated reduced graphene oxide membranes for enhanced water purification, *Chem. Eng. J.* 356 (2019) 915–925.

[154] Z. Wang, M. Chen, Y. Huang, X. Shi, Y. Zhang, T. Huang, J. Cao, W. Ho, S.C. Lee, Self-assembly synthesis of boron-doped graphitic carbon nitride hollow tubes for enhanced photocatalytic NO_x removal under visible light, *Appl. Catal. B Environ.* 239 (2018) 352–361.

[155] J. Zhou, M. Zhang, Y. Zhu, Photocatalytic enhancement of hybrid $\text{C}_3\text{N}_4\text{/TiO}_2$ prepared via ball milling method, *Phys. Chem. Chem. Phys.* 17 (2015) 3647–3652.

[156] Y. Xu, S. Huang, M. Xie, Y. Li, H. Xu, L. Huang, Q. Zhang, H. Li, Magnetically separable $\text{Fe}_2\text{O}_3\text{/g-C}_3\text{N}_4$ catalyst with enhanced photocatalytic activity, *RSC Adv.* 5 (2015) 95727–95735.

[157] A. Arabzadeh, A. Salimi, One dimensional CdS nanowire@ TiO_2 nanoparticles core-shell as high performance photocatalyst for fast degradation of dye pollutants under visible and sunlight irradiation, *J. Colloid Interface Sci.* 479 (2016) 43–54.

[158] L.K. Dhandole, S.-G. Kim, Y.-S. Seo, M.A. Mahadik, H.S. Chung, S.Y. Lee, S.H. Choi, M. Cho, J. Ryu, J.S. Jang, Enhanced photocatalytic degradation of organic pollutants and inactivation of *listeria monocytogenes* by visible light active Rh-Sb codoped TiO_2 nanorods, *ACS Sustainable Chem. Eng.* 6 (2018) 4302–4315.

[159] P. Wang, N. Lu, Y. Su, N. Liu, H. Yu, J. Li, Y. Wu, Fabrication of $\text{WO}_3\text{@g-C}_3\text{N}_4$ with core@shell nanostructure for enhanced photocatalytic degradation activity under visible light, *Appl. Surf. Sci.* 423 (2017) 197–204.

[160] Y. Xu, S. Huang, M. Xie, Y. Li, H. Li, Y. Li, Y. Zhang, H. Li, Magnetically separable $\text{Fe}_2\text{O}_3\text{/g-C}_3\text{N}_4$ catalyst with enhanced photocatalytic activity, *RSC Adv.* 5 (2015) 95727–95735.

[161] L. Liu, Y. Qi, J. Lu, S. Lin, W. An, J. Hu, Y. Liang, W. Cui, Dramatic activity of a $\text{Bi}_2\text{WO}_6\text{@g-C}_3\text{N}_4$ photocatalyst with a core@shell structure, *RSC Adv.* 5 (2015) 99339–99346.

[162] Y. Hong, C. Li, B. Yin, D. Li, Z. Zhang, B. Mao, W. Fan, W. Gu, W. Shi, Promoting visible-light-induced photocatalytic degradation of tetracycline by an efficient and stable beta- $\text{Bi}_2\text{O}_3\text{@g-C}_3\text{N}_4$ core/shell nanocomposite, *Chem. Eng. J.* 338 (2018) 137–146.

[163] A.P. Singh, P. Arora, S. Basu, B.R. Mehta, Graphitic carbon nitride based hydrogen treated disordered titanium dioxide core-shell nanocatalyst for enhanced photocatalytic and photoelectrochemical performance, *Int. J. Hydrogen Energy* 41 (2016) 5617–5628.

[164] J. Zhou, M. Zhang, Y. Zhu, Photocatalytic enhancement of hybrid $\text{C}_3\text{N}_4\text{/TiO}_2$ prepared via ball milling method, *Phys. Chem. Chem. Phys.* 17 (2015) 3647–3652.

[165] D. Tang, G. Zhang, Fabrication of $\text{AgFeO}_2\text{/g-C}_3\text{N}_4$ nanocatalyst with enhanced and stable photocatalytic performance, *Appl. Surf. Sci.* 391 (2017) 415–422.

[166] C. Yogi, K. Kojima, N. Wada, H. Tokumoto, T. Takai, T. Mizoguchi, H. Tamiaki, Photocatalytic degradation of methylene blue by TiO_2 film and Au particles- TiO_2 composite film, *Thin Solid Films* 516 (2008) 5881–5884.

[167] A. Orendorff, C. Ziegler, H. Gnaser, Photocatalytic decomposition of methylene blue and 4-chlorophenol on nanocrystalline TiO_2 films under UV illumination: a ToF-SIMS study, *Appl. Surf. Sci.* 255 (2008) 1011–1014.

[168] H. Zhang, X. Lv, Y. Li, Y. Wang, J. Li, P25-graphene composite as a high performance photocatalyst, *ACS Nano* 4 (2010) 380–386.

[169] M. Cheng, Y. Liu, D. Huang, C. Lai, G. Zeng, J. Huang, Z. Liu, C. Zhang, C. Zhou, L. Qin, W. Xiong, H. Yi, Y. Yang, Prussian blue analogue derived magnetic Cu-Fe oxide as a recyclable photo-Fenton catalyst for the efficient removal of sulfamethazine at near neutral pH values, *Chem. Eng. J.* 362 (2019) 865–876.

[170] M. Cheng, C. Lai, Y. Liu, G. Zeng, D. Huang, C. Zhang, L. Qin, L. Hu, C. Zhou, W. Xiong, Metal-organic frameworks for highly efficient heterogeneous Fenton-like catalysis, *Coord. Chem. Rev.* 368 (2018) 80–92.

[171] L. Sun, Y. Qi, C. Jia, Z. Jin, W. Fan, Enhanced visible-light photocatalytic activity of g-C₃N₄/Zn₂GeO₄ heterojunctions with effective interfaces based on band match, *Nanoscale* 6 (2014) 2649–2659.

[172] Z. He, C. Gao, M. Qian, Y. Shi, J. Chen, S. Song, Electro-Fenton process catalyzed by Fe₃O₄ magnetic nanoparticles for degradation of C.I. Reactive Blue 19 in aqueous solution: operating conditions, influence, and mechanism, *Ind. Eng. Chem. Res.* 53 (2014) 3435–3447.

[173] S. Yuan, X. Mao, A.N. Alshawabkeh, Efficient degradation of TCE in groundwater using Pd and electro-generated H₂ and O₂: a shift in pathway from hydrodechlorination to oxidation in the presence of ferrous ions, *Environ. Sci. Technol.* 46 (2012) 3398–3405.

[174] M.A. Behnajady, M. Hajiahmadi, N. Modirshahla, Enhancement of removal rate of an organic pollutant in the presence of immobilized TiO₂ nanoparticles with inorganic anions combination: optimization using taguchi approach, *Ind. Eng. Chem. Res.* 51 (2012) 15324–15330.

[175] Y. Wang, H. Zhao, M. Li, J. Fan, G. Zhao, Magnetic ordered mesoporous copper ferrite as a heterogeneous Fenton catalyst for the degradation of imidacloprid, *Appl. Catal. B Environ.* 147 (2014) 534–545.

[176] R. Sharma, S. Bansal, S. Singh, Tailoring the photo-Fenton activity of spinel ferrites (MFe₂O₄) by incorporating different cations (M = Cu, Zn, Ni and Co) in the structure, *RSC Adv.* 5 (2014) 6006–6018.

[177] X. Bai, Y. Du, X. Hu, Y. He, E. Liu, J. Fan, Synergy removal of Cr(VI) and organic pollutants over RP-MoS₂/rGO photocatalyst, *Appl. Catal. B Environ.* 239 (2018) 204–213.

[178] H. Miao, J. Yang, Y. Wei, W. Li, Y. Zhu, Visible-light photocatalysis of PDI nanowires enhanced by plasmonic effect of the gold nanoparticles, *Appl. Catal. B Environ.* 239 (2018) 61–67.

[179] S. Wang, T. Peng, Y. Zhang, NH₄Cl-assisted in air, low temperature synthesis of SnS₂ nanoflakes with high visible-light-activated photocatalytic activity, *Mater. Lett.* 234 (2019) 361–363.

[180] C.D. Windle, R.N. Perutz, Advances in molecular photocatalytic and electro-catalytic CO₂ reduction, *Coord. Chem. Rev.* 256 (2012) 2562–2570.

[181] X. Duan, J. Xu, Z. Wei, J. Ma, S. Guo, S. Wang, H. Liu, S. Dou, Metal-free carbon materials for CO₂ electrochemical reduction, *Adv. Mater.* 29 (2017) 1701784.

[182] R.K. Nath, M.F.M. Zain, A.A.H. Kadhum, Artificial photosynthesis using LiNbO₃ as photocatalyst for sustainable and environmental friendly construction and reduction of global warming: a review, *Catal. Rev.* 56 (2014) 175–186.

[183] S.C. Roy, O.K. Varghese, M. Paulose, C.A. Grimes, Toward solar fuels: Photocatalytic conversion of carbon dioxide to hydrocarbons, *ACS Nano* 4 (2010) 1259–1278.

[184] X. Wang, T. Saba, H.H.P. Yiu, R.F. Howe, J.A. Anderson, J. Shi, Cofactor NAD(P)H regeneration inspired by heterogeneous pathways, *Chem.* 2 (2017) 621–654.

[185] V. Ganesan, D. Sivanesan, S. Yoon, Correlation between the structure and catalytic activity of [Cp*Rh(Substituted Bipyridine)] complexes for NADH regeneration, *Inorg. Chem.* 56 (2017) 1366–1374.

[186] S.-S. Lin, O. Miyawaki, K. Nakamura, Continuous production of l-carnitine with NADH regeneration by a nanofiltration membrane reactor with coimmobilized l-carnitine dehydrogenase and glucose dehydrogenase, *J. Biosci. Bioeng.* 87 (1999) 361–364.

[187] S. Shen, J. Chen, M. Wang, X. Sheng, X. Chen, X. Feng, S.S. Mao, Titanium dioxide nanostructures for photoelectrochemical applications, *Prog. Mater. Sci.* 98 (2018) 299–385.

[188] J. Jian, G. Jiang, R. van de Krol, B. Wei, H. Wang, Recent advances in rational engineering of multinary semiconductors for photoelectrochemical hydrogen generation, *Nano Energy* 51 (2018) 457–480.

[189] M.D. Bhatt, J.S. Lee, Recent theoretical progress in the development of photo-anode materials for solar water splitting photoelectrochemical cells, *J. Mater. Chem. A* 3 (2015) 10632–10659.

[190] R.H. Gonçalves, E.R. Leite, The colloidal nanocrystal deposition process: an advanced method to prepare high performance hematite photoanodes for water splitting, *Energy Environ. Sci.* 7 (2014) 2250–2254.

[191] P.S. Bassi, R.P. Antony, P.P. Boix, Y. Fang, J. Barber, L.H. Wong, Crystalline Fe₂O₃/Fe₂TiO₅ heterojunction nanorods with efficient charge separation and hole injection as photoanode for solar water oxidation, *Nano Energy* 22 (2016) 310–318.

[192] F. A, H. K, Electrochemical photolysis of water at a semiconductor electrode, *Nature* 238 (1972) 37–38.

[193] D.M. Andoshe, K. Yim, W. Sohn, C. Kim, T.L. Kim, K.C. Kwon, K. Hong, S. Choi, C.W. Moon, S.-P. Hong, S. Han, H.W. Jang, One-pot synthesis of sulfur and nitrogen codoped titanium dioxide nanorod arrays for superior photoelectrochemical water oxidation, *Appl. Catal. B Environ.* 234 (2018) 213–222.

[194] X. Yu, N. Ren, J. Qiu, D. Sun, L. Li, H. Liu, Killing two birds with one stone: to eliminate the toxicity and enhance the photocatalytic property of CdS nanobelts by assembling ultrafine TiO₂ nanowires on them, *Sol. Energy Mater. Sol. Cells* 183 (2018) 41–47.

[195] G. Rossi, L. Pasquini, D. Catone, A. Piccioni, N. Patelli, A. Paladini, A. Molinari, S. Caramori, P. O'Keeffe, F. Boscherini, Charge carrier dynamics and visible light photocatalysis in vanadium-doped TiO₂ nanoparticles, *Appl. Catal. B Environ.* 237 (2018) 603–612.

[196] X. Fan, T. Wang, B. Gao, H. Gong, H. Xue, H. Guo, L. Song, W. Xia, X. Huang, J. He, Preparation of the TiO₂/graphitic carbon nitride core-shell array as a photoanode for efficient photoelectrochemical water splitting, *Langmuir* 32 (2016) 13322.

[197] C. Nie, L. Liu, R. He, Pt/TiO₂-ZnO in a circuit photo-electro-catalytically removed HCHO for outstanding indoor air purification, *Sep. Purif. Technol.* 206 (2018) 316–323.

[198] H. Wang, Y. Liang, L. Liu, J. Hu, W. Cui, Highly ordered TiO₂ nanotube arrays wrapped with g-C₃N₄ nanoparticles for efficient charge separation and increased photoelectrocatalytic degradation of phenol, *J. Hazard. Mater.* 344 (2018) 369–380.

[199] J. Wang, Z. Yang, X. Gao, W. Yao, W. Wei, X. Chen, R. Zong, Y. Zhu, Core-shell g-C₃N₄@ZnO composites as photoanodes with double synergistic effects for enhanced visible-light photoelectrocatalytic activities, *Appl. Catal. B Environ.* 217 (2017) 169–180.

[200] V. Di Noto, E. Negro, S. Polizzi, K. Vezzù, L. Toniolo, G. Cavinato, Synthesis, studies and fuel cell performance of “core–shell” electrocatalysts for oxygen reduction reaction based on a PtNi_x carbon nitride “shell” and a pyrolyzed polyketone nanoball “core”, *Int. J. Hydrogen Energy* 39 (2014) 2812–2827.

[201] E. Negro, K. Vezzù, F. Bertasi, P. Schiavuta, L. Toniolo, S. Polizzi, V. Di Noto, Interplay between nitrogen concentration, structure, morphology, and electrochemical performance of PdCoNi “core–shell” carbon nitride electrocatalysts for the oxygen reduction reaction, *ChemElectroChem* 1 (2014) 1359–1369.

[202] L. Wei, H. Sun, T. Yang, S. Deng, M. Wu, Z. Li, Iron carbide encapsulated by porous carbon nitride as bifunctional electrocatalysts for oxygen reduction and evolution reactions, *Appl. Surf. Sci.* 439 (2018) 439–446.

[203] W. Yang, X. Liu, X. Yue, J. Jia, S. Guo, Bamboo-like carbon nanotube/Fe₃C nanoparticle hybrids and their highly efficient catalysis for oxygen reduction, *J. Am. Chem. Soc.* 137 (2015) 1436–1439.

[204] W. Xia, R. Zou, L. An, D. Xia, S. Guo, A metal–organic framework route to in situ encapsulation of Co@Co₃O₄@C core@bisphere nanoparticles into a highly ordered porous carbon matrix for oxygen reduction, *Energy Environ. Sci.* 8 (2015) 568–576.

[205] S. Gottesfeld, D.R. Dekel, M. Page, C. Bae, Y. Yan, P. Zelenay, Y.S. Kim, Anion exchange membrane fuel cells: current status and remaining challenges, *J. Power Sources* 375 (2018) 170–184.

[206] D. Bose, S. Sridharan, H. Dhawan, P. Vijay, M. Gopinath, Biomass derived activated carbon cathode performance for sustainable power generation from Microbial Fuel Cells, *Fuel* 236 (2019) 325–337.

[207] A. Mehmeti, J. Pedro Pérez-Trujillo, F. Elizalde-Blancas, A. Angelis-Dimakis, S.J. McPhail, Exergetic, environmental and economic sustainability assessment of stationary Molten Carbonate Fuel Cells, *Energy Convers. Manage.* 168 (2018) 276–287.

[208] A. Serov, I.V. Zhenyuk, C.G. Arges, M. Chatenet, Hot topics in alkaline exchange membrane fuel cells, *J. Power Sources* 375 (2017) 149–157.

[209] R. Chen, J. Zhang, Y. Wang, X. Chen, J.A. Zapien, C.-S. Lee, Graphitic carbon nitride nanosheet@metal–organic framework core–shell nanoparticles for photo-chemo combination therapy, *Nanoscale* 7 (2015) 17299–17305.

[210] M. Wang, C. Liu, X. Zhang, Z. Fan, J. Xu, Z. Tong, In situ synthesis of CsTi₂NbO₇@g-C₃N₄ core–shell heterojunction with excellent electrocatalytic performance for the detection of nitrite, *J. Mater. Res.* 33 (2018) 3936–3945.